Oceanologia

Official Journal of the Polish Academy of Sciences

This journal is supported by the Ministry of Science and Higher Education, Warsaw, Poland

Indexed in: ISI Journal Master List, Science Citation Index Expanded, Scopus, Current Contents, Zoological Record, Thomson Scientific SSCI, Aquatic Sciences and Fisheries Abstracts, DOAJ

IMPACT FACTOR ANNOUNCED FOR 2021 IN THE 'JOURNAL CITATION REPORTS' IS 2.526; 5-year IF is 2.778. CITESCORE ANNOUNCED FOR 2021 IS 4.7

Publisher
Elsevier B.V.
Radarweg 29
1043 NX Amsterdam
The Netherlands

Senior Publisher
Tobias Wesselius
+31 6 5370 3539

ISSN 0078-3234

Oceanologia 65 (2023) 453—465

Available online at www.sciencedirect.com

ScienceDirect

journal homepage: www.journals.elsevier.com/oceanologia

ORIGINAL RESEARCH ARTICLE

Effects of Eulerian current, Stokes drift and wind while simulating surface drifter trajectories in the Baltic Sea

Ove Pärn[a,*], Lina Davulienė[b], Diego Macias Moy[a], Kaimo Vahter[c], Adolf Stips[a], Tomas Torsvik[d]

[a] *European Commission, Joint Research Centre, Ispra, Varese, Italy*
[b] *SRI Center for Physical Sciences and Technology (FTMC), Vilnius, Lithuania*
[c] *Department of Marine Systems, School of Science, Tallinn University of Technology, Tallinn, Estonia*
[d] *Geophysical Institute, University of Bergen, Bergen, Norway*

Received 8 April 2022; accepted 3 February 2023
Available online 16 February 2023

KEYWORDS
Litter modelling;
OceanParcels framework;
Surface drifter trajectories;
Stokes drift;
Wind effect

Abstract The simulation of Lagrangian drift is an important task in applications such as dispersion of pollutants, larvae and search and rescue activities. In this study, the Eulerian current, Stokes drift and wind effect on the simulation of observed drifters were analysed. The Lagrangian OceanParcels model was used, and the surface trajectories were assessed by comparison with 9 GPS drifter trajectories in the Gulf of Finland, Gulf of Riga and Lithuanian coast. The Normalised Cumulative Lagrangian Separation (NCLS) distance between the simulated and the satellite-tracked drifter trajectories, and the mean absolute error (MAE) were used as comparison metrics. The present study suggests the need to consider the Stokes drift and the wind factor in addition to the modelled Eulerian currents to obtain a better description of the trajectories of particles. By making these considerations, the OceanParcels model could adequately simulate particle trajectories in the sub-basins within the Baltic Sea. The realized model tests showed that motion of surface drifters are strongly controlled by the Stokes drift when the

* Corresponding author at: European Commission, Joint Research Centre, Ispra, Varese, Italy.
E-mail address: Ove.PARN@ext.ec.europa.eu (O. Pärn).
Peer review under the responsibility of the Institute of Oceanology of the Polish Academy of Sciences.

Production and hosting by Elsevier

https://doi.org/10.1016/j.oceano.2023.02.001

significant wave height is >1 m, whereas the wind component and the Eulerian currents are crucial when the significant wave height is <0.6 m or the wave (Stokes drift) directions do not match the wind direction.

1. Introduction

Marine litter is observed across oceans and seas worldwide, even in remote areas located far from human activities, and is a global environmental concern (Chiba et al., 2018). Thus, tracking the movement of litter particles in oceans is crucial. Although ocean currents and wind control the distribution and accumulation of floating marine debris, observational data of marine litter are sparse. Thus, analysing and predicting the marine debris movement is challenging (van Sebille et al., 2020).

Factors such as physical properties (size and buoyancy) of the debris influence their transport. Approximately 40% of mismanaged plastic waste that enters the ocean is denser than seawater, and hence, it sinks to the ocean floor near the coast rather than being carried away by surface currents and winds (Andrady, 2011). Even in simplified 2D modelling, surface drift trajectories being a combination of numerous processes, are challenging to simulate. Details of their input factors can still be misunderstood as some of them are difficult to predict. Some very influential factors of the input to the model such as windage can only be estimated. About 7–14% of the factors influencing the drifter are governed by processes (other than direct wind and wave impact) such as eddies, fronts, upwellings, etc. (Delpeche-Ellmann et al., 2021).

Currents, winds, waves and the general prevailing circulation basically define the drift of various objects and substances in the surface layer (Vandenbulcke et al., 2009). State-of-the-art three-dimensional circulation models adequately replicate the major features of the hydrophysical fields such as temperature, salinity, and large-scale water level and currents (Myrberg et al., 2010; Pärn et al., 2021a,b). The reproduction of the details of hydrography and patterns of currents is limited by the model resolution, which may substantially modify the statistical properties of the drift of various substances. The reason for this is that even small errors in the estimates of current patterns and shifts in the position of the water particles due to the impact of a multitude of relatively small-scale turbulent motions can drastically change the calculated trajectories of the drift of floating objects (Griffa et al., 2004; Soomere et al., 2011). For instance, the fact that drifters deployed in the same location may be in different locations within a few hours or days (Davulienė et al., 2014; Soomere et al., 2011). The separation rate of drifters in the Gulf of Finland (GoF) is 200–300 m/day when drifters are deployed from the same location (initial separations <150 m) (Soomere et al., 2011), whereas it is approximately 1000 m/day in the southeastern part of the Baltic Sea (Davulienė et al., 2014).

Earlier drifter studies have been published when Mackas et al. (1989) studied sea ice motions based on drifter observations and meteorological forces in the Baltic Sea. Gästgifvars et al. (2006) studied how well hydrodynamic models can reproduce the drift of buoys. The modelled uppermost layer currents do not replicate drifters over longer time periods (t > 12 h) that are also affected by other ocean drivers, buoyancy effects, Stokes drift, etc. (Murawski and Woge Nielsen, 2013). To solve this problem, Vandenbulcke et al. (2009) used Super-ensemble techniques to predict the surface drift trajectories, which significantly improved the results because a larger number of models smooths out the prediction errors. Murawski and Woge Nielsen (2013) improved the surface current based approach and modelled the drift under the joint impact of currents, and wind and wave-driven advection was addressed using an advanced oil spill model in the Gulf of Finland. Ensemble modelling requires a lot of resources, so instead of using them, scientists use their own individual models for drift prediction. In this case, the developed parameters may be suitable for a particular model while they may not be appropriate for another model.

As described before, the uncertainty of modelling drift depends on the magnitude of sub-grid processes (enters as a random perturbation) and the replicable features of the flow field. However, the third factor that controls the dispersion is the coastlines which make up the geometry of the basin. Lilover et al. (2018) examined high-resolution Eulerian and Lagrangian sea ice kinematics based on an ADCP and icebound drifting buoys in the Gulf of Finland. The average asymptotic ice speed and wind ratio depends on the direction of the wind indicating the role of morphometry of the coast in the speed of the icebound drifting buoys. So, the inaccuracy of morphometric data is one factor that caused the model errors. The shore effect was also reflected in the pattern of locations of coastal hits (beaching) of Lagrangian trackers regardless of the wind forces in the Gulf of Finland (Viikmäe and Soomere, 2018).

Tracking Lagrangian trajectories is a powerful tool for understanding and modelling motion in oceans. Drifters provide essential information on the use of Eulerian fields, predicted wind and waves to model Lagrangian movement. Knowledge of the origin and destination of substances in the marine environment and the spread of particles is essential for modelling the fate of marine litter, living organisms (Corell, 2012) and plankton.

The present study investigates the relative impact of Eulerian current, wind drift and Stokes drift on the simulation of observed drifters. We provide a possible method to compute Lagrangian numerical trajectories for marine litter in the Baltic Sea. To improve and test model predictions,

the model results were compared with data obtained from field measurements by 9 drifters in three specific areas (GoF, GoR and the Lithuanian coast). Therefore, the results of simulation parameters can be site-specific. Moreover, the size of the drifter was not considered.

The wave-generated Stokes drifts can be neglected in model calculations (Edwards et al., 2006; Tamtare et al., 2021), but in this study, they have been considered crucial to obtain satisfactory results from windage and Eulerian currents. The present study attempts to tune the Lagrangian model to reliably simulate marine litter. Marine litter differs in the shapes and properties, and the microlitter does not extend out of the water like drifters. Hence, the microlitter moves as a part of the water currents. Therefore, the present study explored a calculation scheme where the surface current of the Stokes drift and the Eulerian model showed a strong influence factor, whereas the windage had only a small influence.

Generally, the dimensions of the drifters are taken into account, but in this study, drifters of three different sizes were used, and hence, the sizes were ignored. It has been found in the model calculations that the trajectory and speed of floating items are controlled by their size (Giudici et al., 2019) and other physical characteristics (Miron et al., 2020; Zhang, 2017). However, considering the complexity of sea processes, we parameterized wind and wave effects in a very simple way. Nicole Delpeche-Ellmann et al. (2021) studied effects induced by wind and surface waves on the observed surface drift in the Gulf of Finland for the period 2011—2018. For example the drifters in cases 1 and 11 in 2014 with the same dimensions, the same mean wave height (0.5 m), and almost the same mean wind speed (7.1 m/s and 7.5 m/s respectively) were considered, but the speed of these drifters was significantly different: 0.16 m/s and 0.1 m/s. Also, when a drifter with the same dimensions (in 2018, case 1) was in mean wave height of 1 m, mean wind speed 10.4 m/s, the speed of the drifter was only 0.12 m/s. Delpeche-Ellmann et al. (2016) used the data from three drifters of the same dimensions that were deployed simultaneously on 15 May 2013 with their initial locations differing only by a few meters near the island of Naissaar (59.548°N, 24.580°E), and the average speed of the drifters was 0.16, 0.12 and 0.15 m/s.

Comprehensive performance analysis of marine litter tracking models in the Baltic Sea is still missing due to insufficient Lagrangian data. Only a few satellite-tracked drifter experiments have been performed in the Baltic Sea (Davulienė et al., 2014), but a large number of observations and a thorough analysis of drifters have been made in the Gulf of Finland (Delpeche-Ellmann et al., 2021). The difficulties in using surface drifters in the Baltic Sea are associated with heavy ship traffic (HELCOM, 2009) and fishing activities in this area.

2. Material and methods

2.1. Study sites

The GoF is an elongated, shallow (mean depth: 37 m) water body in the northeastern Baltic Sea (Figure 1). The water mass dynamics are affected by the open part of the Baltic Sea on the western side and by a large inflow of freshwater from the east. Thus, buoyancy-driven currents are vital for water circulation (Soomere et al., 2008), resulting in a strong east-west gradient in salinity and sea level (Myrberg et al., 2013). The current system in the GoF exhibits a complicated pattern, mostly comprising of cyclonic circulation at the basin-scale, occasional large elongated anticyclonic gyre in the east-west direction that covers part of the central gulf area (Soomere et al., 2011) in the surface layer depending on the other prevailing natural conditions as well as mesoscale eddies and frequent upwellings (Liblik and Lips, 2017).

The Gulf of Riga (GoR) is shallow (mean depth: 29 m), relatively closed, and an almost circular eastern sub-basin of the Baltic Sea (Figure 1). The water exchange with the Baltic Proper occurs through two openings, namely the Irbe strait (with a sill depth of 25 m and a minimum cross-section area of 0.4 km^2) in the west, and the Suur strait (with a sill depth of 5 m and a minimum cross-sectional area of 0.04 km^2) in the north. A general cyclonic circulation occurs in the GoR (Yurkovskis et al., 1993). Thus, inflowing saltier water through the Irbe Strait moves towards the south along the western slope of the gulf. The basin circulation in the surface layer depends on the existing wind forces and stratification (Lips et al., 2016). However, dominant circulation patterns in spring (near the freshwater inflow) become the anticyclonic gyre in the southeastern part of the GoR, and cyclonic in the northwestern part of the GoR (Soosaar et al., 2014).

The southeastern part of the Baltic Sea along the Lithuanian coast is a part of the existing strong and high-persistence cyclonic gyres within the Baltic Proper.

2.2. Drifter data

In October 2010, five drifters were deployed at different locations in the GoF. Figure 1 specifies the launch position and trajectory of each drifter. Table 1 presents the duration and total length of the trajectories.

Lightweight, durable, and cost-effective drifters were developed by the Tallinn University of Technology and local engineering companies. The drifters had a rugged and simple housing construction and were equipped with a general packet radio service based on two-way communication. Data were transferred in real-time through the internet at 10-minute intervals. No data were available if the connection was lost. Erroneous data were excluded from the study. The drifter was a round tube with an outer diameter of 0.11 m, a length of 1 m, and a submerged part of approximately 0.95 m (Verjovkina et al., 2010).

Tests 6—8 were conducted in 2013 and 2014, where three drifters were deployed in the GoF and GoR. The basic drifter design comprised a polyethylene pipe with length and diameter of approximately 1.8 m and 0.05 m, respectively. The drifter was positioned vertically in the water, where approximately 9/10th part of the pipe was submerged and the remaining 1/10th part of the pipe was above water (Torsvik, 2016).

Test 9 was conducted from 22 to 30 November 2013. The surface drifter experiment was performed along the Lithuanian coast (Figure 1) (Davulienė et al., 2014). Three drifters (a,b,c) were deployed at the location 55.750°N and

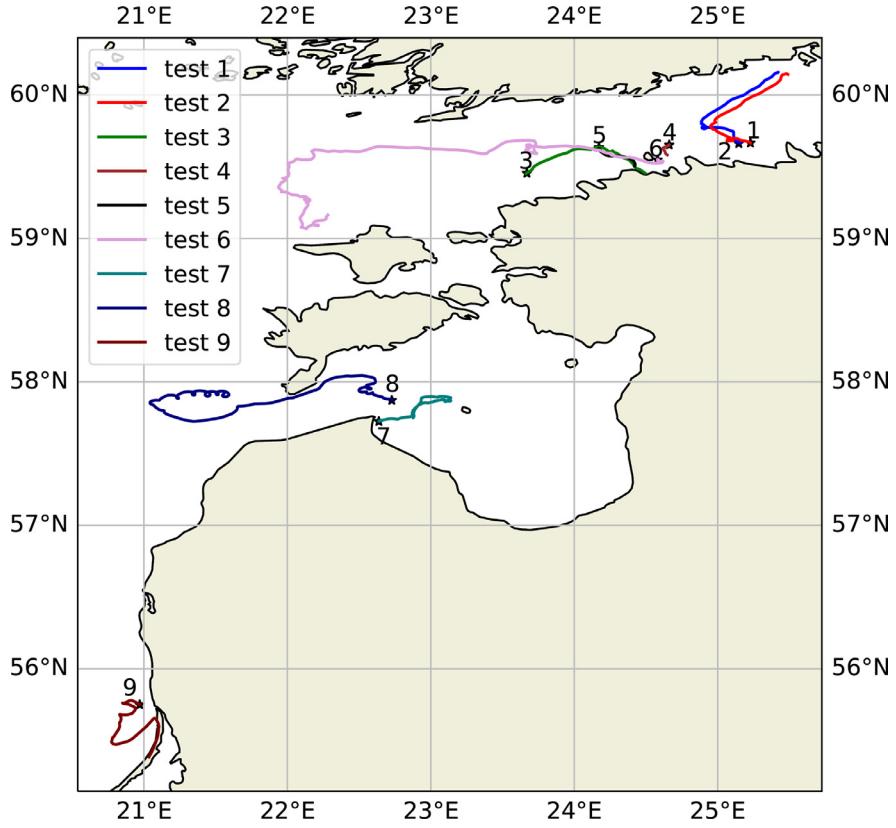

Figure 1 Observed trajectories of drifters deployed at the locations indicated by black stars.

Table 1 Duration and trajectories of drifters; GoF (Gulf of Finland), GoR (Gulf of Riga), LT (Lithuanian coast).

Test no.	Area	Trajectory [km]	Date	Mean/Max speed [m/s]		Mean/Max *Hm0* [m]	
Test 1	GoF	82	24–31.10.2007	0.16	0.8	0.6	1.5
Test 2	GoF	73	24–31.10.2007	0.17	0.4	0.6	1.5
Test 3	GoF	64	16–19.10.2007	0.2	0.5	0.85	1.8
Test 4	GoF	11	10–11.10.2007	0.14	0.2	1	1.3
Test 5	GoF	21	9–10.10.2007	0.25	0.4	1.3	1.8
Test 6	GoF	284	15.05–13.06.2013	0.16	1.7	0.4	1.2
Test 7	GoR	78	02.10–14.11.2013	0.1	0.7	0.9	3.3
Test 8	GoR	65	5–12.07.2014	0.1	1.1	0.65	1.3
Test 9	LT	41	22–30.11.2013	0.17	0.5	1.1	2.5

20.972°E, approximately 6 km from the coast. Each drifter was a tube-shaped plastic pipe weighing 1.8 kg, with a diameter of 0.05 m and a length of approximately 2 m (the submerged part was 1.4 m long). The signals of two drifters (drifters b and c) were lost 56 h after beginning the experiment. The drift experiment ended after 8 days. The distance between drifters a and b increased to 500 m in 16 h from the start of the experiment, and more than 2500 m in 56 h (Davulienė et al., 2014). The maximum dispersion rate of the drifters was 470 m/h.

2.3. Modelling the routes of drifters

The paths of floating objects can be used to study the combined effect of wind, waves, and sea surface currents on their drift. If the wind, wave, and sea surface current conditions during the drift are known, the optimal wind drag coefficients can be calculated such that the model best fits the observed trajectories. Wind, wave and sea surface data can be obtained from either sensors or ocean and atmospheric dynamic models.

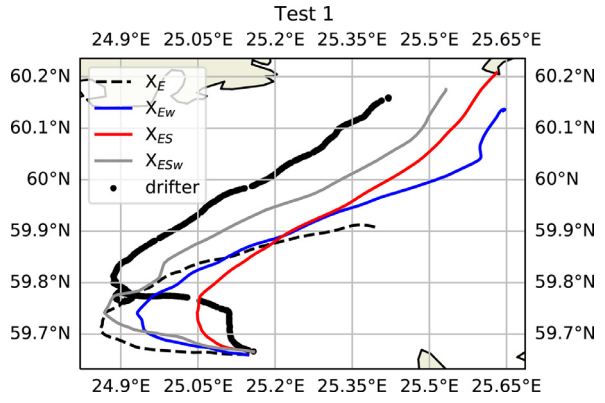

Figure 2 The track of the observed drifter is compared to the modelled drifter carried by Eulerian model currents x_E, modelled drifter carried by x_{Ew} (x_E and adjusted for the wind vector x_w), the modelled drifter carried by x_{ES} (x_E and Stokes drift x_S), and the modelled drifter carried by x_{ESw} (x_E, Stokes drift x_S and the wind vector x_w).

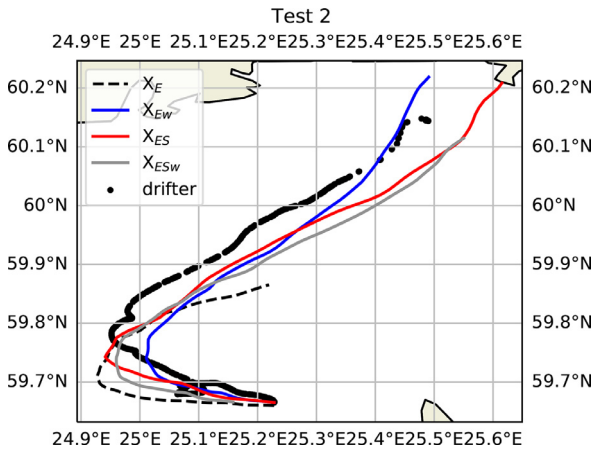

Figure 3 The track of the observed drifter is compared to the modelled drifter carried by Eulerian model currents x_E, modelled drifter carried by x_{Ew} (x_E and adjusted for the wind vector x_w), the modelled drifter carried by x_{ES} (x_E and Stokes drift x_S), and the modelled drifter carried by x_{ESw} (x_E, Stokes drift x_S and the wind vector x_w).

Tuomi et al. (2018) confirmed that the Stokes drift is a crucial component of the surface drift in the Baltic Sea. Additionally, those authors determined that the annual mean value of the Stokes drift in the Baltic Sea is 0.08–0.1 m/s. Thus, the influence of the Stokes drift on the surface drift is as crucial as that of surface currents on the surface drift.

The following equations are used for simulating the drifter location x as a function of time t:

$$\frac{dx}{dt} = u_E + \beta u_S + \alpha u_w \tag{1}$$

where u_E is the Eulerian sea surface current of the upper grid cell calculated with the GETM model (Section 2.5), and u_S is the wave-induced Stokes drift. This Stokes drift data is provided by the Finnish Meteorological Institute (FMI), with a timestep of 1 h and a grid resolution of 1 nautical mile. u_w is the wind vector taken from an ERA5 reanalysis service output, and α is the wind correction term. It can be $\alpha_1 = 0.022$ and $\alpha_2 = 0.007$. The values are obtained by the trial and error method, where the drifters' MAE (t = 48h) is minimal. Beta indicates whether the Stokes drift was used or not. For validation, the Lagrangian model produced the following tracers:

$$x_E, \alpha = \beta = 0 \tag{1a}$$

$$x_{ES}, \alpha = 0, \beta = 1 \tag{1b}$$

$$x_{Ew}, \alpha = \alpha_1 = 0.022, \beta = 0 \tag{1c}$$

$$x_{ESw}, \alpha = \alpha_2 = 0.007, \beta = 1 \tag{1d}$$

The mean error (MAE) for the distance (d) between the observed drifter and the modelled drifter was calculated every hour.

$$MAE = \frac{1}{n}\sum_{i=1}^{n} d_i \tag{2}$$

where d_i is the separation distance between observed and simulated trajectories at time step i.

For model skill assessment, the normalised cumulative Lagrangian separation (NCLS) distance (Liu and Weisberg, 2011) was calculated as follows:

$$NCLS = \frac{MAE}{\sum_{i=1}^{n} l_i} \tag{3}$$

where l_i is the length of the observed trajectory at time step i, and n is the forecast horizon. The present study calculated NCLS after 24 h and 48 h.

2.4. Lagrangian model description

The OceanParcels framework was used to track marine litter. This framework can create customisable particle tracking simulations by using outputs from ocean circulation models. OceanParcels is a Lagrangian ocean analysis tool that has wide flexibility for modelling particles with different characteristics and can be efficiently implemented using modern computing infrastructure.

The latest version of OceanParcels includes a set of interpolation schemes that can read different discretised fields, from rectilinear to curvilinear grids in the horizontal direction and from z- to s-levels in the vertical direction. Additionally, the set of schemes can read different variable distributions such as the distributions in Arakawa's A-, B-, and C-grids (Delandmeter and van Sebille, 2019).

The timestep for the calculation of the position of virtual drifters in OceanParcels was 0.5 h. The starting points of virtual drifters were determined by the starting points and times of the observed drifters.

2.5. Eulerian ocean surface current data

The OceanParcels simulations for plastic model validation were performed using a coupled three-dimensional model system comprising a hydrodynamic model GETM (https://getm.eu/; Burchard and Bolding, 2002; Stips et al., 2004) and general ocean turbulence model (GOTM;

www.gotm.net). This system resolves the vertical mixing (Umlauf and Burchard, 2005) and ice existence problems (Pärn et al., 2021a,b). The Baltic Sea model implementation considering the land-based runoff by Väli et al. (2019), had a horizontal resolution of 2 × 2 nautical miles and includes 25 vertical σ layers with an open boundary in northern Kattegat (Pärn et al., 2021a,b). The thickness of the extracted upper layer is 1.6 m. The meteorological data of the ERA5 reanalysis obtained from the ECMWF for every 1 h were applied to the model and wind correction analyses.

The drift depends strongly on surface currents. Due to the complicated nature of these currents, no model can simulate them accurately. There are numerous sources of differences behind the results produced using different hydrodynamic models. We checked the drift with another independent model NEMO-Nordic for surface currents to examine if it yields the same effect as the GETM model (Supplementary material, Section 1). For comparison, we used the hourly high-resolution NEMO-Nordic data, which are available since 2019. Hence, this model comparison study does not describe the time series associated with drifters and is not generalizable. This provides case-by-case insight that in many cases the patterns of current movement coincide, but also that the direction of currents at the same time and location can be significantly different across models. For instance, in the Gulf of Finland, the best agreement was reached between the two models on 20 July (Figure S2), when the average MAE of the 4 trajectories was 5.1 km, and the average length of the 4 trajectories was 23 km during 24 h. In the comparison of all trajectories in the Gulf of Finland, the average MAE was 8.1 km. The best agreement between the two models in the Gulf of Riga was 3.4 km on 02 June (Figure S3a) when virtual drifters travelled 20 km on average. The MAE of all trajectories during the two months of June and July was 6.7 km. The best agreement is in the Lithuanian coastal waters on 04 July (Figure S4), when MAE = 3.6 km, and virtual drifters covered an average of 28.4 km during 24 h. During the two months, the MAE of all trajectories was 7.1 km.

3. Results

Simulated Eulerian currents do not fully reproduce observed Lagrangian tracks. The trajectories of virtual drifters (x_E) generated by the Eulerian currents in Tests 1 and 2 (Figures 2 and 3) exhibited a similar shape to the observations, but the lengths of the trajectories were more than 2 times shorter, and thus, the virtual drifter and drifter end positions are 37.2 km apart. In Tests 3, 4 and 5 (Figures 4–6), in the modelled trajectory x_E the disagreement with the drifter observations is so great that the simulated trajectory does not reflect the observations at all.

We can see that the virtual drifter trajectories calculated from Eulerian currents are significantly shorter in all the Tests (Tests 1–5) than in the observations. This is an expected feature as the drifter normally has motions caused by subgrid motions in addition to those that are replicated by circulation models. Tests 1–5 (Figures 2–6) serve to explore the relevance of Stokes drift and windage effects as alternative parameters for optimising simulated drift trajectories. The modelled trajectories (x_{ES}; Figures 2–6) generated by the Eulerian currents and Stokes drift are closer to the observations than x_E. However, while using x_{ES}, the speeds were higher than those of the virtual drifters (Tests 1 and 2), and the virtual drifters reached the northern shore of the GoF (Figures 2 and 3) faster. The mean significant wave height (*Hm0*) was 0.9 m (if the first 48 h are excluded from the drifter journey). The inclusion of Stokes drift provided more impetus and the trajectories lengthened too much (Figures 2 and 3). In Tests 3 and 4, the speed is comparatively slower and the trajectory x_{ES} is shorter than in the observations. In Test 3, for the first 20 h, $Hm0 = 1.3$ m, and then falls to 0.5 m for the 5 h during the rest of the journey, $Hm0 = 0.85$ m.

The wind speed (from E) of Tests 1 and 2 was relatively low ($U < 4.5$ m/s) for the first 30 h, and the mean significant wave height was small ($Hm0 < 0.2$ m). Then on 27 October, the drifters (Tests 1 and 2) change direction (longitude 24.89 and 24.95, respectively) (Figures 2 and 3). The 6-hour average wind speed increased; it was 6.5–13 m/s for the following 5 days. Then the wind direction stayed between S to SW and *Hm0* was between 1–1.5 m until 31 October. Finally, on the last day of the experiment, $Hm0 = 0.4$ m.

Additional wind effects may manifest themselves in different ways. For position x, in equation (1) using the velocities (1c) and (1d), we used two different wind tuning parameters: α_1 when the inputs are Eulerian currents and wind in cases x_{Ew}, and α_2 when the inputs are Eulerian currents, Stokes drift and wind in cases x_{ESw}. The α values were obtained from tests, where, for each case, a different trajectory was used for best results, and each tuning parameter exhibited a different value. The optimal result was the one with the smallest MAE and NCLS values. The best match between the observations and the model for x_{Ew} α_1 was 0.022, whereas that for x_{ESw} α_2 was 0.007.

The modelled trajectory (x_{Ew}; Figures 2 and 3) generated by the Eulerian currents and windage (with α_1) exhibited a trajectory close to the trajectory of the observed drifter (Table 2).

In Test 3, two drifters were launched from almost the same location. During ~72 hours, the first drifter covered 64 km (Figure 4), and the second drifter covered 67 km. The final position between the two drifters was only 1.7 km. Both the drifters were of the same type and size. On 17 October, 184 positions were recorded for both drifters, and their speed correlation was 0.34, which was lesser than expected, and the average wind speed was 8 m/s. There can be differences in speed between the drifters. One drifter can be twice as much as the other or only one-half times the speed of the other in the same time intervals. In Test 3, the modelled trajectory, which was improved by adding a wind component to the calculation, was near the drifter trajectory (Figure 4), and both the x_{ESw} and x_{Ew} (MAE = 2.1 and 2.2 km respectively) exhibited a close result to the observations. At the outset of Test 4, the modelled virtual particles x_{ES}, x_{ESw}, and x_{Ew} moved south for the first few hours (Figure 5), whereas the drifter moved northwest causing a large discrepancy. MAE for each of x_{ES}, x_{ESw}, and x_{Ew} was 1.9 km. However, visually, the closest to the observation was x_{EW}. In Test 5, the trajectory x_{Esw} best fitted the observa-

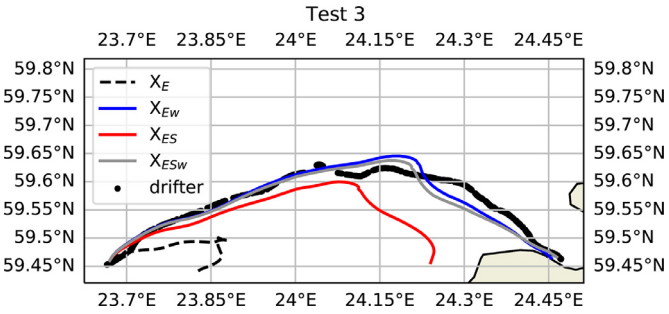

Figure 4 The track of the observed drifter is compared to the modelled drifter carried by Eulerian model currents x_E, modelled drifter carried by x_{Ew} (x_E and adjusted for the wind vector x_w), the modelled drifter carried by x_{ES} (x_E and Stokes drift x_S), and the modelled drifter carried by x_{ESw} (x_E, Stokes drift x_S and the wind vector x_w).

Table 2 The mean distances between the observed drifter and the modelled drifter.

Test no.	MAE [km] (24 h/48 h)		NCLS (24 h/48 h)	
	x_{ES}	x_{ESw}	x_{ES}	x_{ESw}
Test 1	4.5 / 7.3	1.8 / 2.9	12.4 / 12	2.9 / 3.5
Test 2	2.3 / 2.7	2.3 / 2.7	2.8 / 3.6	2.7 / 3.4
Test 3	2.4 / 4.7	1.8 / 2.1	1.4 / 3.2	1.3 / 1.2
Test 4	1.9 / –	1.9 / –	4.5 / –	4.4 / –
Test 5	5.1 / –	0.8 / –	4.1 / –	0.9 / –
Test 6	2.6 / 3.4	2.4 / 3.3	9.1 / 5.1	8.6 / 5
Test 7	1.9 / 2.2	2.4 / 2.6	6.4 / 3.3	8.7 / 5.1
Test 8	1.7 / 6.7	1.7 / 7.3	3 / 8.1	3.2 / 8.9
Test 9	1.2 / 2.1	0.7 / 1.2	2.6 / 3.8	1.5 / 2.3

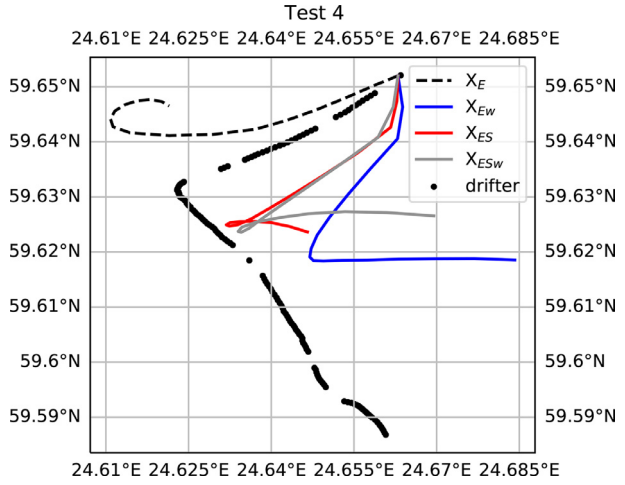

Figure 5 The track of the observed drifter is compared to the modelled drifter carried by Eulerian model currents x_E, modelled drifter carried by x_{Ew} (x_E and adjusted for the wind vector x_w), the modelled drifter carried by x_{ES} (x_E and Stokes drift x_S), and the modelled drifter carried by x_{ESw} (x_E, Stokes drift x_S and the wind vector x_w).

tions and x_{Ew} also replicated the model well. MAE was 0.8 km for x_{ESw}, and MAE for x_{Ew} was 1.2 km (Figure 6). The average wind speed on the first day was 3 m/s, but on the other test days, it was 9.8 m/s.

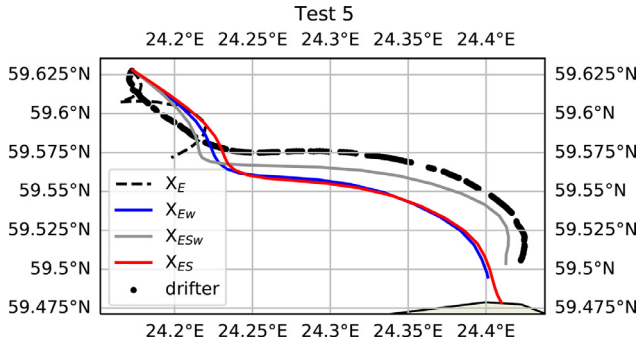

Figure 6 The track of the observed drifter is compared to the modelled drifter carried by Eulerian model currents x_E, modelled drifter carried by x_{Ew} (x_E and adjusted for the wind vector x_w), the modelled drifter carried by x_{ES} (x_E and Stokes drift x_S), and the modelled drifter carried by x_{ESw} (x_E, Stokes drift x_S and the wind vector x_w).

We can see from the experiment's results (Table 2, Figures 2–6) that if we simulate the surface trajectory of a drifter (when part of the instrument is out of the water), which is exposed to the wind, then Stokes Drift is not relevant. Therefore, there exists a strong connection between the winds and the motions in the surface layer, but this strong correlation is not straightforward as it is different in each test. Delpeche-Ellmann et al. (2016) found that the drifter trajectories could be almost entirely aligned with

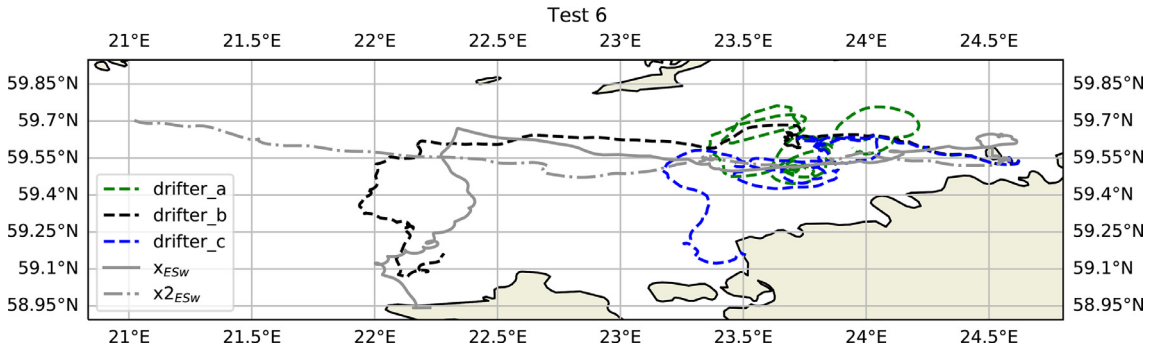

Figure 7 The track of the observed drifters (a, b, c) is compared to the modelled drifters $x2_{ESw}$ and x_{ESw}.

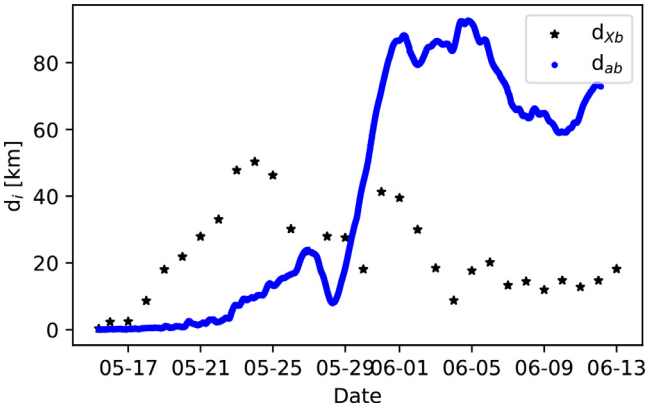

Figure 8 For Test 6, the distance between the model drifter and drifter b is indicated by stars, and the distance between drifters a and b is shown by the solid line.

the wind direction during episodes of 10—15 m/s winds, but would tend to meander at lower wind speeds. But, it might be relevant if we aim to model marine litter that is deeper than the water surface and may not have direct exposure to wind. However, we can see that the Stokes Drift improves the performance of the visual drift for all the,s.

In Test 6 (Figure 7), three drifters (a,b,c) were deployed with their initial locations differing by only a few meters. But, the daily MAE (Figure 8, drifters a and b) between the observed drifter_a and drifter_b was more than 80 km after the 16th day. The large difference in trajectories a, b and c is explained as the drifters entered into strong upwelling events (Delpeche-Ellmann et al., 2016).

Test 6 was sensitive to the starting point because upwelling events occurred at a short distance from the launch site. The Eulerian circulation was highly variable in this region. The model did not replicate the drifter structure when we used the exact drifter starting point. A small difference in the starting point affects the trajectory of the drifter. The starting point of the simulated x_{2ESw} trajectory (Figure 7, grey dashed line) shifted 880 m south compared to x_{ESw} (Figure 7, solid line). However, the longitude of the starting point was the same for both trajectories. The direction of the modelled trajectories changed drastically at longitude 22.5°E, with both moving in different directions. However, the drifters with the same starting positions also moved in different directions (Figure 7, green and blue line). Visually, drifter_b and virtual drifter x_{ESw} followed the same pattern. However, a shift was observed in the timeline after the third day when the daily MAE between the virtual drifter and drifter_b (dxb) was less than 4 km in 3 days, and it began to grow rapidly to 49 km on 24 May (Figure 8).

In Test 7, the movement of the drifter was replicated by the trajectory x_{ESw} of the model (Figure 9). However, an abrupt change occurred after 4.5 days (23.15°E) when the drifter returned westward (blue line in Figure 9). However, the modelled particle continued to move eastwards for both trajectories (Figure 9, red and grey lines). At this location, neither the wind nor the force of Eulerian currents indicated the necessity of a sharp change in the direction of the virtual drifter motion. The red and blue arrows indicate the direction and speed of the surface current and wind, respectively. The current scale is 1:1, and the wind speed is 1:150.

In the GoR rather than in the GoF, the Stokes drift is more crucial than windage (Figure 10). This can be attributed to the difference between the wave fields in GoR and GoF. In the GoR, the distributions of wave directions also mirror the combination of the directional structure of winds (Eelsalu et al., 2014). Wind-wave misalignment occurs in the GoF (Alari et al., 2013). In Test 8, the direction of the wind and wave is predominantly of the same structure. 92% of the time, the difference is less than 10 degrees. Data with a time step of 1h was compared (the wind forces for the wave model came from HIRLAM, and we used ERA5 winds). Test 7 was a long simulation, and in some episodes, at the beginning, the wind and wave direction was accurate 15% of the time. However, 89% of the time, the difference was less than 10 degrees in Test 7.1 (Table 3), and in the last 14 days, it was less than 10 degrees 93% of the time. Therefore, adding windage usually reinforces the impact of Stokes drift as in the GoR and Tests 1 and 2. In Tests 1 and 2, the wind and wave direction structure is almost the same (86% of the time the difference is less than 10 degrees), but in Tests 3, 4 and 5, the difference in structure is dominant (less than 29% of the time the difference is less than 10 degrees in Tests 3, 4, 5). In Test 9, 60% of the time the difference is less than 10 degrees. In Test 8, both x_{ES} and x_{ESw} were in agreement with the observations (Figure 10, Table 2). On the second day, at longitude 22.6°E, a time shift came into the drifter and the modelled trajectory, where the drifter makes a rotation and turns around. Only the Stokes drift component (no Eulerian

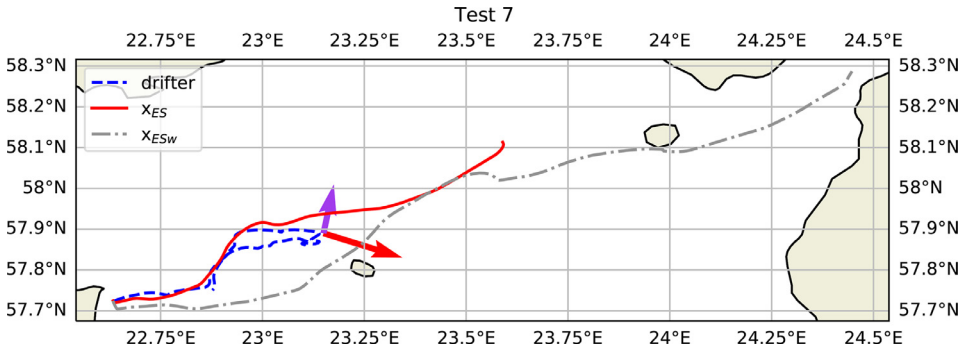

Figure 9 The track of the observed drifter is compared to the virtual drifter. The red and violet arrows indicate the direction and speed of the surface current and wind, respectively. The current scale is 1:1, and the wind speed is 1:150.

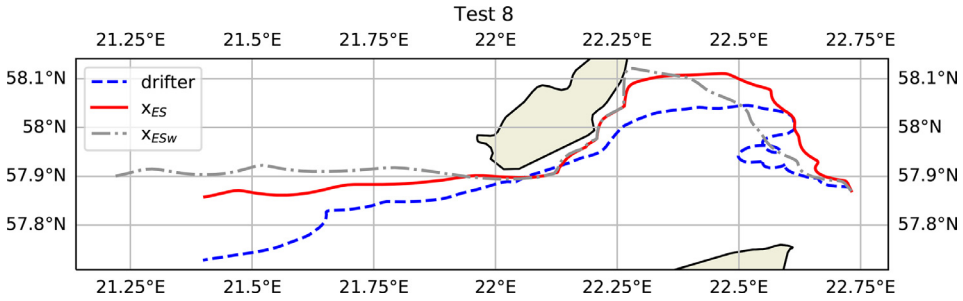

Figure 10 The track of the observed drifters is compared to the modelled drifter.

Table 3 Trajectories and conditions of drifters; duration of drifts is 2 days; GoF (Gulf of Finland), GoR (Gulf of Riga), LT (Lithuanian coast).

Test no.	Area	Trajectory [km]	Start time	Mean/Max speed [m/s]		Mean/Max *Hm0* [m]	
Test 1.1	GoF	37	28.10.2007	0.21	0.39	1.1	1.5
Test 1.2	GoF	15	29.10.2007	0.08	0.3	0.7	1.1
Test 2.1	GoF	39	28.10.2007	0.22	0.38	1.1	1.5
Test 3.1	GoF	44	17.10.2007	0.26	0.7	0.7	1.5
Test 6.1	GoF	21	17.05.2013	0.12	0.3	0.6	1.5
Test 6.2	GoF	15	18.05.2013	0.09	0.2	0.4	0.8
Test 7.1	GoR	18	3.10.2013	0.1	0.22	0.5	1
Test 8.1	GoR	28	8.07.2014	0.16	0.3	0.4	1
Test 8.2	GoR	46	10.07.2014	0.26	0.7	0.9	1.5
Test 8.3	GoR	37	15.07.2014	0.21	1.4	0.9	1.4
Test 9.1	LT	30	24.11.2013	0.17	0.4	1.2	1.9
Test 9.2	LT	32	26.11.2013	0.19	0.5	1.8	2.5
Test 9.3	LT	28	27.11.2013	0.16	0.5	2.6	3.4

currents and windage effects) results in Test 7 MAE = 1.8 km (after 1 day), and 2.1 km (after 2 days), and for Test 8 MAE = 1.6 km and 6.5 km respectively.

For Test 9 (Figure 11), the model was in agreement with the observations for x_{ESw} (Table 2). The virtual drifter x_{ESw} covered 67.4 km in 5 days and 7 h, where 7 h after the start of the drifter experiment MAE = 378 m, and after 31 h, it was 752 m. After the fifth day and 7 h, the drifter reached the beach according to the GETM model. This drifter experiment lasted another 2 days with the drifter moving south on the water-shore border, an area outside the GETM model domain. The 5-day average MAE was 1.54 km. The spectral significant wave heights (*Hm0*) are shown in Table 1 (Lindgren et al., 2021). For the first 40 h of Test 9, the *Hm0* was 0.2—0.5 m. In the following five days (02—29 November), *Hm0* was between 1.2—3.5 m.

To obtain additional data for analysis, we divided the trajectories of drifters into two-day-long segments (Figure 12, Table 3). We used the coordinates of the observation drifter at 00:00 hours UTC for each date. These coordinates became the starting point for calculating the modelled trajectories during 48 h.

In Figure S5 in Tests 1.1 to 3.1, in all the cases, the routes of the modelled x_{ESw} trajectories are very similar to the tra-

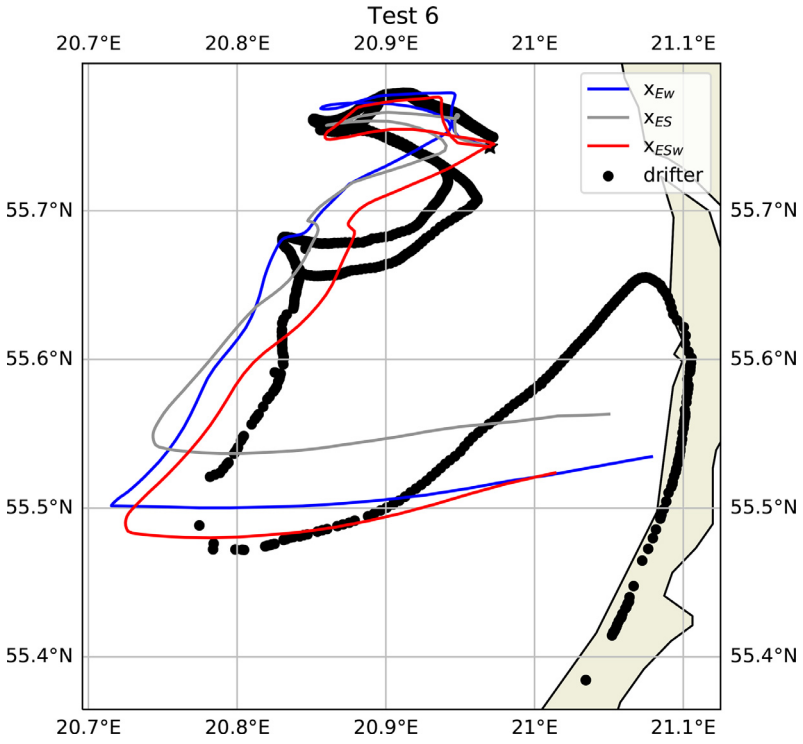

Figure 11 The track of the observed drifters (a, b) is compared to the modelled drifter.

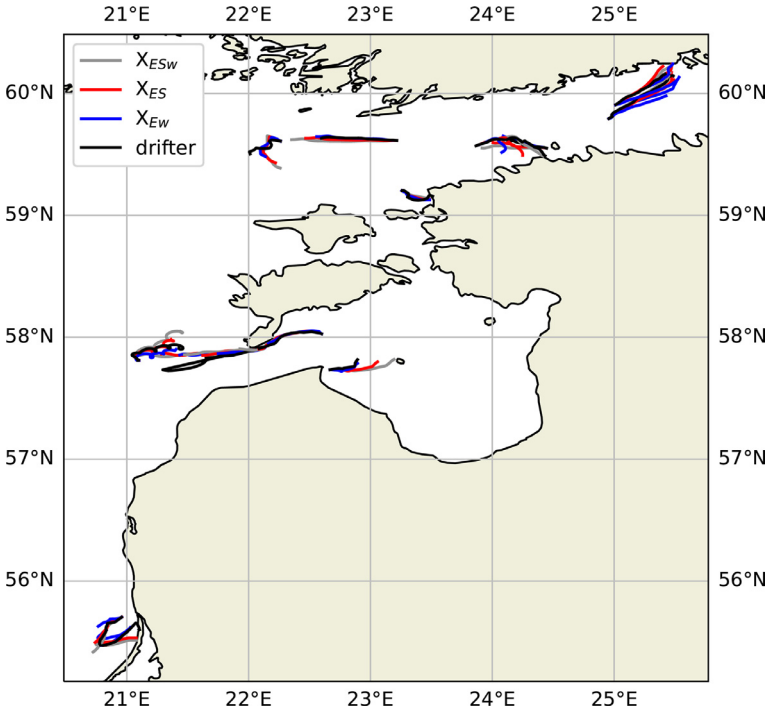

Figure 12 The track of the observed drifters is compared to the modelled drifter by 48 h sections.

jectories of the drifters. However, such a trend is not reflected in the statistics. After zooming in, more detailed trajectories are shown in the supplementary material (Figure S5). In Tests 1.1, both x_{ES} and x_{ESw} have MAE (48 h) = 4.3 km, but NCLS is smaller for the x_{ES} trajectory. In Test 2.1 as well, MAE is lower for x_{ES}. MAE and NCLS are calculated every hour, so the distance covered in an hour is more accurate for x_{ESw} even if this trajectory deviates slightly from the path. x_{ESw} follows the path more precisely but moves either faster or slower during the same time step. Wave direction was aligned with the wind direction in Test 1.1. In Test 1.2, the drifter has reached an area where the significant wave

Table 4 The mean distances between the observed drifter and the modelled drifter.

	MAE [km] (24 h/48 h)			NCLS (24 h/48 h)		
	x_{ES}	x_{Ew}	x_{ESw}	x_{ES}	x_{Ew}	x_{ESw}
Test 1.1	2.1/ 4.3	3.3/ 4.8	2.4/ 4.3	2.2 / 4.5	3.2/5.2	2.4/ 5.1
Test 1.2	0.7/ 3.1	1.6/ 3.4	1.2/ 1.9	0.9 / 7.1	2/ 8.1	1.8/ 4.8
Test 2.1	1.8 / 3	1.5/ 3.7	1.6 / 3.1	2.2 / 3.1	1.9/ 3.8	1.8 / 3.1
Test 3.1	2 / 5.7	4.3/8.2	1.4 / 3.1	1.8 / 4.5	3.8/7.9	1.1 / 3.1
Test 6.1	2.2 / 4.2	1/ 1.3	3.2 / 6.7	4 / 6.7	1.7/ 2.5	5.8 / 15
Test 6.2	2 / 4.4	0.9/ 1.8	3.4 / 7.8	3 / 5.3	1.3/ 2.3	4.8 / 10
Test 7.1	1.6 / 4	1.7/ 2.2	2.6 / 7.2	4.7 / 6.3	4.8/ 5.2	7/ 18
Test 8.1	1.8 / 1.7	3.6/ 5.2	0.9 / 2.7	2.7 / 2.2	5.4/ 6.4	1.2 / 8
Test 8.2	1.1/ 2	1.7/ 2.5	1.6/ 5.7	1.3/ 1.6	1.8/ 2.2	2/ 5.6
Test 8.3	4.5/ 5.5	4.5/ 6	5/ 10	9/ 7.3	9/ 7.5	12/ 14
Test 9.1	1.9 / 3.1	4.3/ 8	1.6 / 3.3	2.7 / 4.2	6/ 10	2.3 / 2.5
Test 9.2	0.8/ 4.4	2/ 3.8	1.4/ 4.7	1.4 /6.5	3.4/ 5.6	1.9/ 5.7
Test 9.3	5/ 7.4	1.8/ 2.9	6/ 8.3	4.8/ 7.8	1.9/ 2.2	5.9/ 8.4

height is less than 0.8 m, the wave directions do not match the wind direction, and x_{ESw} is more accurate. In Test 3.1, on the first day (17 October) the significant wave height was between 0.8—1.5 m, but by the beginning of the second day, it had dropped to 0.4 m in the evening, and it rose again to 1 m. The wave directions matched the wind direction by 26% during Test 3.1. On the first day, both x_{ES} and x_{ESw} accurately replicate the route of the observation drifter, but on the second day, x_{ESw} is more accurate. In Tests 6.1 and 6.2 (Table 3), we see that if the speed of the drifter is slow (0.09—0.12 m/s) and the mean significant wave height is small ($Hm0 < 0.7$ m), then the most accurate result was x_{Ew} MAE = 4.2 and 4.4 km, and the use of Stokes drift and wind together gave the most inaccurate result with MAE = 6.7 and 7.8 km (Table 4). Also, in Test 7.1, the wave height and drift speed are small, and the most accurate result was achieved with x_{Ew}. In Test 8.1, the mean wave height was small ($Hm0 = 0.4$ m) as well, but the drift speed was 1.5 times higher than in Test 7.1. The average speed was 0.16 m/s (Table 3), and the most accurate result was given by x_{ES}. In Tests 9.1—9.3, both drift speed and wave height were high, $U > 0.16$ m/s and $Hm0 > 1.2$ m. The smallest MAE of Test 9.1 was 3.1 km for x_{ES}. Tests 9.2 and 9.3 were initiated one day apart, so they have an overlapping area. The most accurate result was given by x_{Ew} which seems to contradict the previous analysis. But, the fact that these movements took place near the coast, where the water is shallow, can be an important factor. This is not reflected in the statistics of this study as that is not the scope of this paper. However, it was observed through analysis that if the drifter got close to the coast, then the most accurate result was given by x_E in which only the Eulerian sea surface currents were used to model the trajectory.

In a shorter period of time ($t < 24$ h), Stokes drift and currents (x_{ES}) were statistically the most important factor and gave the most accurate result while considering the entire picture. But, in the case of a longer simulation, the end position of the drifter was closer to the final position of the drifter due to the combined effect of Stokes drift and wind (x_{ESw}). When only x_{ESw} was used, the speeds of the virtual drifters were mostly overestimated.

4. Summary and conclusions

The importance of Eulerian currents, windage, and the Stokes drift was investigated for simulating the trajectory of the observed drifter. The performance of the Lagrangian model was assessed in the Baltic Sea by using the trajectories of nine drifters from different periods under diverse dynamical conditions. When we looked at each drifter or drifter section, a Lagrangian trajectory close to almost every observation case was modelled by combining different input parameters like Eulerian currents, windage, and the Stokes drift. The calibration factors, which combine all those parameters, varied across each case study. Since our aim is to use the Lagrangian model for modelling marine litter such as plastic, the Eulerian currents and the Stokes drift were fully taken into account. The best windage factor for all the cases was $\alpha_2 = 0.007$. The results in terms of simulation parameters may be site-specific and we did not consider the design of the drifter.

In order to evaluate the model's performance, it is necessary to consider the complex processes occurring at sea. Uncertainty of the virtual drifter which causes the modelling errors depends on the magnitude of sub-grid processes (enters as a random perturbation) and the replicable features of the Eulerian flow field and morphometry. For example, the distance between two drifters launched at sea at the same time and location (in Test 9, section 2.2) can increase to more than 2500 m in 56 h. In order to keep the virtual drifters modelling as simple as possible, we did not take into account that three types of size drifters were used in the observations. Even observed drifters with the same dimensions can drift at different speeds at the same instants of time in the same area. For example, in Test 3, two drifters were deployed at the same time on 17 October. The speed correlation was only 0.34, and they had different speeds within

the same time intervals. However, the dimensions of floating particles must be taken into account in future studies.

With this combination of input parameters, the Lagrangian particle tracking modelling framework 'OceanParcels' can simulate the trajectory of a drifter buoy (Figures 2–11). The mean error between the observed drifter buoy and the modelled one was between 0.7–7.8 km during the two days (Tables 2 and 4).

The wind is strongly connected to the surface currents and allows the prediction of the movement of the drifter. We found that the inclusion of surface waves (Stokes drift) in the models led to a more accurate prediction of the transport of surface substances. The current proposed scheme works best when the wave height is < 0.7 m. When the significant wave heights $Hm0 > 1$ m, and wave directions matched the wind direction, the Stokes drift becomes more important (like Tests 7 and 8 in GoR) than windage. While wave directions did not match the wind direction, adding a windage component improved the ability to replicate the Test (Tests 3, 5 and 9).

In a shorter period of time ($t < 24$ h), Stokes drift and currents (x_{ES}) are statistically the most important factor (Table 4) and give the most accurate result while considering the entire picture. But, in the case of a longer simulation, the end position of the drifter is closer to the final position of the drifter due to the combined effect of Stokes drift and wind (x_{ESw}). When wave directions matched the wind direction then x_{ESw}, the speeds of the virtual drifters were mostly overestimated (Test 1, 2 and 8).

- Eulerian currents are not sufficient to describe the trajectory of a drifter.
- Wind drift ($\alpha_1 = 0.022$) and Eulerian currents are promising parameters to be considered for the simulation of the observed drifters. Stokes drift further improves the modelling accuracy.
- There was a strong and straightforward connection between the Stokes drift and the motions of the drifter when the significant wave height was $Hm0 > 1$ m.
- To compute Lagrangian numerical trajectories in cases conducted in this study, the best fit was when the Eulerian currents and the Stokes drift were fully taken into account, and the windage factor was $\alpha_2 = 0.007$.
- The windage component improved replication ability when wave directions did not match the wind direction. When $Hm0 > 0.7$ m and the wave directions matched the wind direction, the Stokes drift and the Eulerian currents were more important than the windage factor.

Acknowledgements

The authors greatly thank the reviewers for their insightful comments which helped improve this manuscript. Many thanks also to Anisha Bhosale for her invaluable help in editing the text and English. Great thanks also to the drifter data: Team of Professor Tarmo Soomere in Tallinn University of Technology, Department of Cybernetics, Dr. Tarmo Kõuts, who organized the drift experiment at the Department of Marine Systems, and many thanks to Professor Inga Dailidiene in Klaipeda University for organizing the drifter experiment at the Lithuanian coast.

Declaration of competing interest

The authors declare that there are no conflicts of interest.

Supplementary materials

Supplementary material associated with this article can be found, in the online version, at https://doi.org/10.1016/j.oceano.2023.02.001.

References

Alari, V., Van Vledder, G.P., 2013. Spatial variability of directional misalignment between waves and wind in the Baltic Sea-model study. In: Measurements. 13th International Workshop on Wave Hindcasting and Forecasting, 4th Coastal Hazard Symposium, Banff, Canada, 16 pp.

Andrady, A.L., 2011. Microplastics in the marine environment. Mar. Pollut. Bull. 62 (8), 1596–1605.

Burchard, H., Bolding, K., 2002. GETM. A general estuarine transport model, Scientific documentation, JRC EUR Report 20253EN.

Chiba, S., Saito, H., Fletcher, R., Yogi, T., Kayo, M., Miyagi, S., Ogido, M., Fujikura, K., 2018. Human footprint in the abyss: 30 year records of deep-sea plastic debris. Mar. Policy 96, 204–212. https://doi.org/10.1016/j.marpol.2018.03.022

Corell, H., Moksnes, P.O., Engqvist, A., Döös, K., Jonsson, P.R., 2012. Depth distribution of larvae critically affects their dispersal and the efficiency of marine protected areas. Mar. Ecol. Prog. Ser. 467, 29–46. https://doi.org/10.3354/meps09963

Davulienė, L., Kelpšaite, L., Dailidiene, I., 2014. Surface drifters experiment in the south-eastern part of the Baltic Sea. Baltica (2). https://doi.org/10.5200/baltica.2014.27.24

Delandmeter, P., Sebille, E., 2019. The parcels v2.0 Lagrangian framework: new field interpolation schemes. Geosci. Model Dev. 12 (8), 3571–3584. https://doi.org/10.5194/gmd-12-3571-2019

Delpeche-Ellmann, N., Giudici, A., Rätsep, M., Soomere, T., 2021. Observations of surface drift and effects induced by wind and surface waves in the Baltic Sea for the period 2011–2018. Estuar. Coast. Shelf Sci. 249, 107071. https://doi.org/10.1016/j.ecss.2020.107071

Delpeche-Ellmann, N., Torsvik, T., Soomere, T., 2016. A comparison of the motions of surface drifters with offshore wind properties in the Gulf of Finland, the Baltic Sea. Estuar. Coast. Shelf Sci. 172, 154–164. https://doi.org/10.1016/j.ecss.2016.02.009

Edwards, K.P., Werner, F.E., Blanton, B.O., 2006. Comparison of observed and modeled drifter trajectories in coastal regions: an improvement through adjustments for observed drifter slip and errors in wind fields. J. Atmos. Ocean. Technol. 23 (11), 1614–1620.

Eelsalu, M., Org, M., Soomere, T., 2014. Visually observed wave climate in the Gulf of Riga. In: 2014 IEEE/OES Baltic International Symposium (BALTIC), 1–10.

Gästgifvars, M., Lauri, H., Sarkanen, A., Myrberg, K., Andrejev, O., Ambjörn, C., 2006. Modelling surface drifting of buoys during a rapidly-moving weather front in the Gulf of Finland, Baltic Sea. Estuar. Coast. Shelf Sci. 70 (4), 567–576. https://doi.org/10.1016/j.ecss.2006.06.010

Giudici, A., Kalda, J., Soomere, T., 2019. Generation of large pollution patches via collisions of sticky floating parcels driven by wind and surface currents. Mar. Pollut. Bull. 141, 573–585. https://doi.org/10.1016/j.marpolbul.2019.02.039

Griffa, A., Piterbarg, L.I., Ozgokmen, T., 2004. Predictability of Lagrangian particle trajectories: effects of smoothing of the underlying Eulerian flow. J. Mar. Res. 62 (1), 1–35. https://doi.org/10.1357/00222400460744609

HELCOM, 2009. Ensuring safe shipping in the Baltic. Helsinki Commission, Helsinki, 20 pp.

Liblik, T., Lips, U., 2017. Variability of pycnoclines in a three-layer, large estuary: the Gulf of Finland. Boreal Environ. Res. 22, 27—47. https://doi.org/10.5194/os-8-603-2012

Lilover, M.-J., Pavelson, J., Kõuts, T., Leppäranta, M., 2018. Characteristics of high-resolution sea ice dynamics in the Gulf of Finland, Baltic Sea. Boreal Env. Res. 23, 175—191.

Lindgren, E., Tuomi, L., Huess, V., 2021. Baltic Sea Wave Hindcast, CMEMS-BAL-PUM-003-015. https://doi.org/10.48670/moi-00014

Lips, U., Zhurbas, V., Skudra, M., Väli, G., 2016. A numerical study of circulation in the Gulf of Riga, Baltic Sea. Part I: Whole-basin gyres and mean currents. Cont. Shelf Res. 112, 1—13. https://doi.org/10.5194/bg-2021-160

Mackas, D.L., Crawford, W.R., Niiler, P.P., 1989. A performance comparison for two Lagrangian drifter designs. Atmos.-Ocean 27 (2), 443—456. https://doi.org/10.1080/07055900.1989.9649346

Miron, P., Olascoaga, M.J., Beron-Vera, F.J., Putman, N.F., Triñanes, J., Lumpkin, R., Goni, G.J., 2020. Clustering of marine-debris- and *Sargassum*-like drifters explained by inertial particle dynamics. Geophys. Res. Lett. 47 (19), e2020GL089874. https://doi.org/10.1029/2020GL089874

Murawski, J., Woge Nielsen, J., 2013. Applications of an oil drift and fate model for fairway design. In: Soomere, T., Quak, E. (Eds.), Preventive Methods for Coastal Protection: Towards the Use of Ocean Dynamics for Pollution Control. Springer, Cham, 367—415. https://doi.org/10.1007/978-3-319-00440-2_11

Myrberg, K., Ryabchenko, V., Isaev, A., Vankevich, R., Andrejev, O., Bendtsen, J., Erichsen, A., Funkquist, L., Inkala, A., Neelov, I., Rasmus, K., Medina, M.R., Raudsepp, U., Passenko, J., Soderkvist, J., Sokolov, A., Kuosa, H., Anderson, T.R., Lehmann, A., Skogen, M.D., 2010. Validation of three-dimensional hydrodynamic models in the Gulf of Finland based on a statistical analysis of a six model ensemble. Boreal Environ. Res. 15, 453—479.

Myrberg, K., Soomere, T., 2013. The Gulf of Finland, its hydrography and circulation dynamics, Preventive Methods for Coastal Protection. Springer, Heidelberg, 181—222. https://doi.org/10.1007/978-3-319-00440-2_6

Pärn, O., Friedland, R., Rjazin, J., Stips, A., 2021b. Regime shift in sea-ice characteristics and impact on the spring bloom in the Baltic Sea. Oceanologia 64 (2), 181—222. https://doi.org/10.1016/j.oceano.2021.12.004

Pärn, O., Lessin, G., Stips, A., 2021a. Effects of sea ice and wind speed on phytoplankton spring bloom in central and southern Baltic Sea. PloS One 16 (3), e0242637. https://doi.org/10.1371/journal.pone.0242637

Soomere, T., Myrberg, K., Lepparanta, M., Nekrasov, A., 2008. The progress in knowledge of physical oceanography of the Gulf of Finland: a review for 1997—2007. Oceanologia 50 (3), 287—362.

Soomere, T., Viidebaum, M., Kalda, J., 2011. On dispersion properties of surface motions in the Gulf of Finland. Proc. Est. Acad. Sci. 60 (4), 269. https://doi.org/10.3176/proc.2011.4.07

Soosaar, E., Maljutenko, I., Raudsepp, U., Elken, J., 2014. An investigation of anticyclonic circulation in the southern Gulf of Riga during the spring period. Cont. Shelf Res. 78, 75—84. https://doi.org/10.1016/j.csr.2014.02.009

Stips, A., Bolding, K., Pohlmann, T., Burchard, H., 2004. Simulating the temporal and spatial dynamics of the North Sea using the new model GETM (general estuarine transport model). Ocean Dynam. 54 (2), 266—283. https://doi.org/10.1007/s10236-003-0077-0

Tamtare, T., Dumont, D., Chavanne, C., 2021. The stokes drift in ocean surface drift prediction. J. Oper. Oceanogr. 15 (3), 1—13. https://doi.org/10.5194/egusphere-egu2020-9752

Torsvik, T., 2016. Data processing and performance testing of a low-cost surface drifter design for use in coastal waters. Proc. Est. Acad. Sci. 65 (1), 58. https://doi.org/10.3176/proc.2016.1.06

Tuomi, L., Vähä-Piikkiö, O., Alenius, P., Björkqvist, J.V., Kahma, K.K., 2018. Surface Stokes drift in the Baltic Sea based on modelled wave spectra. Ocean Dynam. 68 (1), 17—33. https://doi.org/10.1007/s10236-017-1115-7

Umlauf, L., Burchard, H., 2005. Second-order turbulence closure models for geophysical boundary layers: a review of recent work. Cont. Shelf Res. 25 (7—8), 795—827.

van Sebille, E., Aliani, S., Law, K.L., Maximenko, N., Alsina, J.M., Bagaev, A., et al., 2020. The physical oceanography of the transport of floating marine debris. Environ. Res. Lett. 15 (2), 023003. https://doi.org/10.1088/1748-9326/ab6d7d

Vandenbulcke, L., Beckers, J.-M., Lenartz, F., Barth, A., Poulain, P.-M., Aidonidis, M., Meyrat, J., Ardhuin, F., Tonani, M., Fratianni, C., Torrisi, L., Pallela, D., Chiggiato, J., Tudor, M., Book, J.W., Martin, P., Peggion, G., Rixen, M., 2009. Super-ensemble techniques: Application to surface drift prediction. Prog. Oceanogr. 82 (3), 149—167. https://doi.org/10.1016/j.pocean.2009.06.002

Väli, G., Meier, M., Dieterich, C., Placke, M., 2019. River runoff forcing for ocean modeling with in the Baltic sea model intercomparison project. Leibniz-Institut für Ostseeforschung Warnemünde. https://doi.org/10.12754/msr-2019-0113

Verjovkina, S., Raudsepp, U., Kõuts, T., Vahter, K., 2010. Validation of Seatrack Web Using surface drifters in the Gulf of Finland and Baltic Proper. In: 2010 IEEE/OES Baltic International Symposium (BALTIC). IEEE, 1—8. https://doi.org/10.1109/BALTIC.2010.5621634

Viikmäe, B., Soomere, T., 2018. The persistence of spatial patterns of beaching of current-driven pollution in a changing wind climate: a case study for the Gulf of Finland. Boreal Environ. Res. 23, 299—314.

Yurkovskis, A., Wulff, F., Rahm, L., Andruzaitis, A., Rodriguez-Medina, M., 1993. A nutrient budget of the Gulf of Riga; Baltic Sea. Estuar. Coast. Shelf Sci. 37 (2), 113—127. https://doi.org/10.1006/ecss.1993.1046

Zhang, H., 2017. Transport of microplastics in coastal seas. Estuar. Coast. Shelf Sci. 199, 74—86. https://doi.org/10.1016/j.ecss.2017.09.032

Oceanologia 65 (2023) 466—483

Available online at www.sciencedirect.com

ScienceDirect

journal homepage: www.journals.elsevier.com/oceanologia

ORIGINAL RESEARCH ARTICLE

Variations of temperature, salinity and oxygen of the Baltic Sea for the period 1950 to 2020

Vera Stockmayer, Andreas Lehmann*

GEOMAR Helmholtz Centre for Ocean Research, Kiel, Germany

Received 29 April 2022; accepted 3 February 2023
Available online 4 March 2023

KEYWORDS
Climate variability;
Temperature, salinity and oxygen evolution;
Baltic Sea;
Time series analysis

Abstract Variations of temperature, salinity and oxygen of the Baltic Sea on interannual to decadal timescales were studied for the period from 1950 to 2020. Both observational data and the output of a numerical circulation model of the Baltic Sea were analyzed. In addition, we investigated the influence of atmospheric parameters and river runoff on the observed hydrographic variations. Variability of sea surface temperature (SST) closely follows that of air temperature in the Baltic on all timescales examined. Interannual variations of SST are significantly correlated with the North Atlantic Oscillation in most parts of the sea in winter. The entire water column of the Baltic Sea has warmed over the period 1950 to 2020. The trend is strongest in the surface layer, which has warmed by 0.3—0.4°C decade^{-1}, noticeably stronger since the mid-1980s. In the remaining water column, characterized by permanent salinity stratification in the Baltic Sea, warming trends are slightly weaker. A decadal variability is striking in surface salinity, which is highly correlated with river runoff into the Baltic Sea. Long-term trends over the period 1950—2020 show a noticeable freshening of the upper layer in the whole Baltic Sea and a significant salinity increase below the halocline in some regions. A decadal variability was also identified in the deep layer of the Baltic Sea. This can be associated with variations in saltwater import from the North Sea, which in turn are influenced by river runoff: fewer strong saltwater inflows were observed in periods of enhanced river runoff. Furthermore, our results suggest that changes in wind speed have an impact on water exchange with the North Sea. Interannual variations of surface oxygen are strongly anti-correlated with those

* Corresponding author at: GEOMAR Helmholtz Centre for Ocean Research, Düsternbrooker Weg 20, 24105 Kiel, Germany.
E-mail address: alehmann@geomar.de (A. Lehmann).
Peer review under the responsibility of the Institute of Oceanology of the Polish Academy of Sciences.

Production and hosting by Elsevier

https://doi.org/10.1016/j.oceano.2023.02.002

of SST. Likewise, the positive SST trends are accompanied by a decrease in surface oxygen. In greater depths of the Baltic Sea, oxygen decrease is stronger, which is partly related to the observed increase of the vertical salinity gradient.

1. Introduction

Due to the brackish water conditions, the ecosystem in the Baltic Sea is unique and vulnerable. Most species already live at the edge of their comfort zone and small changes in the water properties could cause shifts in the ecosystem. Therefore, the question of how a changing climate affects the Baltic Sea is of particular interest. To investigate what changes and variations of hydrography can already be observed in the Baltic Sea is part of this work. The focus is mainly on the variations of temperature, salinity and oxygen as these are not only characteristic parameters for identifying and comparing different types of watermasses but also significantly determine the living conditions in marine ecosystems.

The Baltic Sea is a semi-enclosed basin in northeast Europe and one of the largest brackish seas on Earth (Figure 1). On the long-term mean, salinity is consistent with the water balance in the Baltic Sea (Omstedt and Rutgersson, 2000). The main components of the freshwater budget are river runoff, net precipitation (precipitation minus evaporation) and water exchange with the North Sea at the entrance area. Because of the dominant river runoff, the water budget is strongly positive and a general outflow of brackish Baltic Sea water into the Kattegat results from the freshwater surplus. This is compensated by an inflow of higher saline bottom water from the Skagerrak and Kattegat into the Baltic Sea (for details see Leppäranta and Myrberg, 2009). The basin-like topography with shallow sills restricts the horizontal spread of dense bottom water in the Baltic Sea. Irregular barotropic exchange flows such as Major Baltic Inflows (MBIs, Matthäus and Schinke, 1999) and Large Volume Changes (LVC, Lehmann et al., 2017) are needed to renew the bottom waters in the Baltic deeps. Those inflows take place sporadically and can be observed as high salinity and oxygen peaks in time series of the deep waters all the way from the western Baltic to the northern Baltic Proper (Liblik et al., 2018; Mohrholz, 2018). There is no long-term trend in MBI occurrence (Mohrholz, 2018) and the frequency of large volume changes (Lehmann and Post, 2015). Salinity changes in the Baltic Sea are rather dominated by multidecadal variability with a period of about 30 years, likely driven by changes in river runoff and wind (Kniebusch et al., 2019b; Meier and Kauker, 2003).

Water temperature in the Baltic Sea, especially in winter, follows the two-layer structure determined by the salinity distribution. In the upper layer, the temperature is mainly driven by solar radiation and air-sea interactions. During summer, an additional surface layer forms, separating the upper layer into a mixed layer and a cold intermediate layer below. The permanent halocline, usually located at a depth of 40—80 m (Leppäranta and Myrberg, 2009), prevents vertical exchange and decouples the higher saline layer from the brackish surface layer. Temperature variations in and below the halocline are mainly caused by advection from salt water inflows in this layer. Long-term trends of sea surface temperature show much greater warming in the Baltic Sea than the global mean, with the strongest trends since the mid-1980s (Kniebusch et al., 2019a; MacKenzie and Schiedek, 2007). In recent decades, SST trends of about 0.4—0.6°C per decade have been observed in the Baltic Sea (BACC II Author Team, 2015; Lehmann et al., 2011; Liblik and Lips, 2019; Tronin, 2017).

Oxygen content in the Baltic Sea is determined by uptake from the atmosphere, vertical and lateral transport, and consumption of oxygen by biogeochemical processes (Lehmann et al., 2022). As a result of the limited vertical convection through the halocline, deep water masses are often poorly oxygenated and anoxic conditions can be found at the bottom. A strong increase of hypoxia in the Baltic Sea during the last century due to increased nutrient inputs and higher water temperatures was reported by Carstensen et al. (2014). During an MBI, oxygen-rich water is brought into the Baltic deeps, which might temporarily improve the oxygen conditions and end anoxic states (e.g. Neumann et al., 2017).

Since the Baltic Sea is quite shallow, the dynamics are to a large extent wind-driven and variations in temperature, salinity and oxygen are closely linked to the prevailing atmospheric conditions. The climate of the Baltic Sea region is strongly related to the atmospheric large-scale circulation. In particular, the North Atlantic Oscillation (NAO) has a large impact on the Baltic Sea climate (Hurrell, 1995). A positive (negative) phase of the NAO is characterized by a strengthened (diminished) near-surface pressure difference between the Icelandic Low and Azores High, with stronger (weaker) than normal westerly winds. Consequently, a positive NAO is associated with warm and humid winters and a negative NAO with cold and dry winters over the Baltic area (BACC I Author Team, 2008). The influence of the NAO on the Baltic Sea can be observed in many different factors. Hänninen et al. (2000) showed a relationship between the NAO and river runoff to the Baltic Sea: a positive phase of the NAO is related to increased runoff, followed by a decrease in the mean salinity. Their results are confirmed by Zorita and Laine (2000), who studied the dependence of salinity and oxygen concentrations in the Baltic Sea on large-scale atmospheric circulation. They observed decreased salinities at all depths and enhanced oxygen conditions during strong meridional sea level pressure gradients over the North Atlantic. Andersson (2002) and Lehmann et al. (2002) presented a correlation between the NAO and changes in the Baltic sea level, and corresponding volume exchange with the North Sea, respectively.

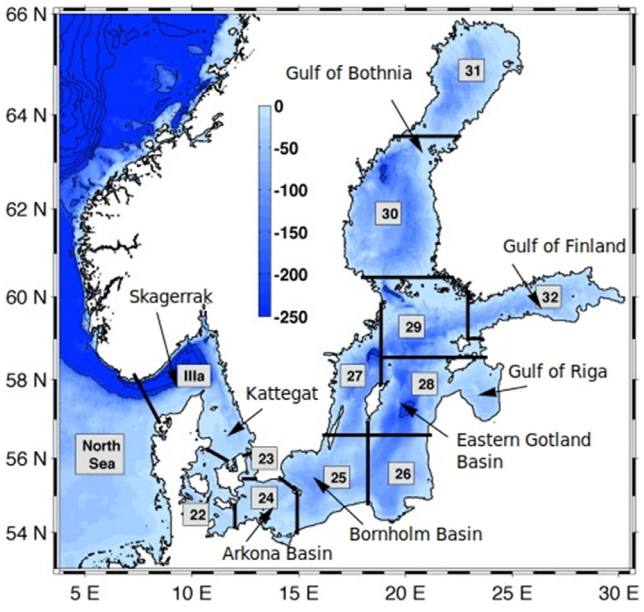

Figure 1 The Baltic Sea region with ICES subdivisions (with small modifications from Lehmann et al., 2014). Color scale shows sea depth in m.

The aim of this study is to provide a detailed investigation of changes in temperature, salinity and oxygen on different time and space scales in the Baltic Sea for the period 1950 to 2020. The main questions we would like to address are: Which variability and trends can be identified in the three parameters during this period of 71 years? And to what extent can the observed variations be explained by the influence of the atmosphere and river runoff? The former is analyzed by comparing observational data with the output of a numerical circulation model of the Baltic Sea. The data sets provide a sufficiently long period to investigate variability not only on annual and interannual but also on decadal time scales and allow validation of the results through comparison. Although many publications have analyzed variations in the hydrography of the Baltic Sea (e.g. BACC I Author Team, 2008; BACC II Author Team, 2015; Kniebusch et al., 2019a,b; Liblik and Lips, 2019; Meier et al., 2022), few studies have investigated variations of temperature, salinity and oxygen over this long period in such detail.

A detailed description of the data and methods used in this study is presented in the following section. The subsequent results section consists of two parts: First, the variations of temperature, salinity and oxygen in the Baltic Sea are described. In the second part, the atmospheric influence on the Baltic Sea hydrography is analyzed. Thereafter, the results are discussed in Section 4 and the paper ends with a short conclusion.

2. Data and methods

2.1. ICES data set on ocean hydrography

In this study, data sets of temperature, salinity and oxygen from the International Council for the Exploration of the Sea (ICES) oceanographic database were used as observational data (ICES, 2022). The data sets consist of a collection of CTD (Conductivity-Temperature-Depth) and bottle measurements from the entire Baltic Sea, spatially averaged across the ICES subdivisions (SD, see Figure 1) and aggregated to monthly means with a vertical resolution of 5 m stratum. It must be noted that the quality of spatially and temporally averaged values may differ in the individual months and subdivisions, depending on how many measurements were available. Furthermore, negative oxygen is not present in the ICES data set. The first measured values listed in the ICES data sets date from the end of the 19th century. However, there are large gaps in the data, especially at the beginning of the time series, as there are no measurements for some years and months. Good data coverage is given in most SDs from the 1950s or 1960s onwards. In the Gulf of Bothnia (SD 30 and 31), the Gulf of Riga and the Gulf of Finland (SD 32), there are large data gaps until the end of the 1970s (Liblik and Lips, 2019), especially in winter, because ice coverage makes measurements during the sea ice season which lasts on average from January to April (Leppäranta and Myrberg, 2009) difficult. This might have an impact on the trend estimations which we discuss further below. We used linear interpolation along the depth and time axes to close smaller data gaps. For each subdivision, we checked individually from which year onwards sufficient data are available to make linear interpolation reasonable. Particular care was taken to ensure that annual cycles in temperature and oxygen time series are well represented. As a rule, the gaps were not allowed to be larger than three consecutive months. Since the data coverage in the individual subdivisions varies, the prepared time series are of different lengths. The longest period is from 1956 to 2018 for the Arkona Basin (SD 24), the Bornholm Basin (SD 25) and the southeastern Baltic Proper (SD 26) and the shortest period is from 1977 to 2018 for the Gulf of Bothnia (SD 30 and 31) and the Gulf of Finland (SD 32). Finally, we applied a 3-month filter (moving average) to reduce noise and irregularities in the data.

2.2. Baltic Sea model output

Parallel to the observational data, the output of the three-dimensional coupled sea ice-ocean model of the Baltic Sea (BSIOM, Lehmann et al., 2002; Lehmann and Hinrichsen, 2000) was analyzed and both data sets were compared with each other. The Baltic Sea model has currently a horizontal resolution of 2.5 km, and the vertical structure is described by 60 layers, which allows resolving the upper 100 m with layers of 3 m thickness and layers of 6 m thickness below (Lehmann et al., 2014). The model covers the entire Baltic Sea, including the Kattegat and Skagerrak. At the western boundary, a simplified North Sea basin is connected to the model domain to provide characteristic temperature and salinity profiles in case of inflow situations from the North Sea into the Skagerrak. Outflowing water leaving the model domain will be slowly relaxed at the surface to typical North Sea salinity conditions. The model is further forced by low-frequency sea level variations in the North Sea/Skagerrak calculated from the BSI (Baltic Sea Index, Lehmann et al., 2002).

Table 1 Considered time periods and depths of surface layer, halocline and bottom layer for the selected ICES subdivisions.

	Considered time period	Surface layer [m]		Halocline depth [m]		Bottom layer [m]	
		ICES	BSIOM	ICES	BSIOM	ICES	BSIOM
Arkona Basin (SD 24)	1956—2018	0—10	1.5—10.5	30—40	31.5—40.5	40—45	40.5—46.5
Bornholm Basin (SD 25)	1956—2018	0—10	1.5—10.5	50—60	49.5—58.5	80—90	82.5—91.5
Eastern Gotland Basin (SD 28)	1959—2018	0—10	1.5—10.5	65—75	52.5—61.5	230—240	228—240
Gulf of Finland (SD 32)	1977—2018	0—10	1.5—10.5	60—70	61.5—70.5	—	—

The hydrodynamic model is realistically forced using the ERA5 global re-analysis in the preliminary extension version back to 1950 (Bell et al., 2021), with a 3-hourly temporal and approximately 50 km spatial resolution, respectively. The forcing data were interpolated on the model grid. They include surface air pressure, precipitation, cloudiness, and air- and dew point temperatures at 2 m height from the sea surface. Wind speed and wind direction at 10 m height from the sea surface were calculated from geostrophic winds with respect to different degrees of roughness on the open sea and off the coast (Bumke et al., 1998). BSIOM forcing functions, such as wind stress, radiation and heat fluxes were calculated according to Rudolph and Lehmann (2006).

In addition, river runoff is included in a monthly mean runoff data set provided by HELCOM Baltic Sea Environment Fact Sheets (Johansson, 2016). Oxygen uptake at the sea surface is determined from the oxygen saturation concentration using the modelled sea surface temperature and salinity values. The consumption of oxygen is modelled by one pelagic and two benthic sinks due to microbial and macrofaunal respiration (for details see Lehmann et al., 2014).

In this study, the output of the current model run from 1950 to 2020 is used. To obtain conditions as similar as possible to the observational data, the modelled temperature, salinity and oxygen values were spatially averaged across the whole area of the ICES subdivisions and monthly means were calculated. The time periods of the model data for each subdivision were adjusted to those of the ICES data for better comparability. Furthermore, we smoothed the data with a 3-month filter just like the observational data.

2.3. Analysis and comparison of ICES observational data and BSIOM data

The Baltic Sea is divided into 11 subdivisions according to ICES (Figure 1). Four specific subdivisions were selected and investigated for variations in temperature, salinity and oxygen: the Arkona Basin (SD 24), Bornholm Basin (SD 25), eastern Gotland Basin with the Gulf of Riga (SD 28) and Gulf of Finland (SD 32). Time series of temperature, salinity and oxygen were considered at three representative depth levels: at the surface, in the area of the halocline and at the bottom. For each depth level, the average was taken over a layer of about 10 m thickness. The depth of the halocline was determined using the 5%, 50% and 95% percentiles of salinity profiles (see Figure 2), visually estimating where the salinity gradient is strongest. The exact depths can be found in Table 1. In the Gulf of Finland, there is no permanent halocline at a specific depth. Instead, the presence and depth of the halocline vary with the prevailing inflow and wind conditions (Lehmann et al., 2022; Liblik and Lips, 2017; Stoicescu et al., 2019). Therefore, after averaging the data, the halocline is not visible in the percentiles in Figure 2.

On the annual time scale, mean annual cycles of temperature, salinity and oxygen were calculated for each subdivision and the three depth levels (surface, halocline, bottom) over the entire period (see Table 1 for the considered period in each subdivision). Time series of the monthly mean values with subtracted mean annual cycles were created to analyze the variability on longer than annual time scales. Linear trends were recalculated at all depths for the entire period using linear regression. To examine whether the time series showed variability on decadal time scales, a 10-year window trend was calculated using a moving average. Pearson correlation coefficients between the time series based on ICES and BSIOM data were determined to examine the agreement between the two data sets. For all correlation calculations, the annual cycles and linear trends of the time series were removed beforehand. Trend values and Pearson correlation coefficients in the present work were considered significant when the p-value was ≤ 0.05.

2.4. Investigation of the atmospheric influence on the hydrography of the Baltic Sea

The second part of this study deals with the influence of the atmosphere on the hydrography of the Baltic Sea. It is investigated whether the variations in temperature, salinity and oxygen can be related to changes in atmospheric parameters. For this purpose, the 2 m air temperature, zonal wind speed at 10 m height and precipitation from the ERA5 reanalysis data set (see Section 2.2) were used. Like the hydrographic data, the atmospheric parameters have also been averaged over the ICES subdivisions and to monthly mean values beforehand. Time periods of the ERA5 data were adjusted to those specified by the ICES data for each subdivision (see Table 1). Time series with anomalies from the annual cycle of air temperature were compared and correlated with sea surface temperature anomalies based on ICES and BSIOM data. Additionally, linear trends for the air temperature were calculated.

The impact of freshwater inflow was investigated using river runoff data provided by HELCOM (Johansson, 2016), which is also used as forcing in the Baltic Sea model. The

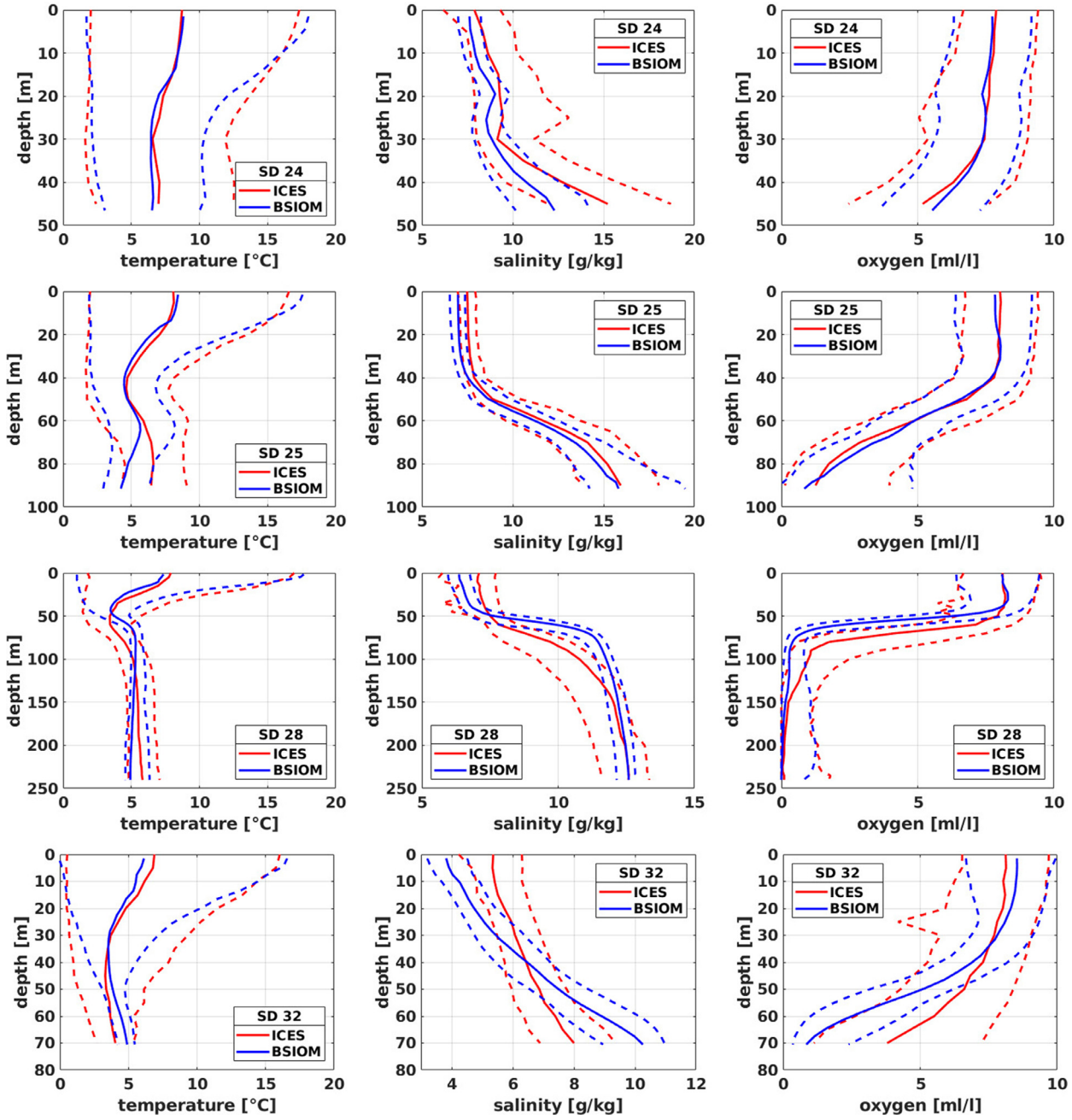

Figure 2 Percentiles (5% and 95%: dashed line, 50%: solid line) of temperature, salinity and oxygen profiles for SD 24 (period 1956—2018), SD 25 (period 1956—2018), SD 28 (period 1959—2018) and SD 32 (period 1977—2018) based on monthly means of ICES observational data and BSIOM model output. The monthly mean data are filtered with a 3-month moving average.

data set contains the sum of river discharge into the entire Baltic Sea and was used here with a temporal resolution of annual mean values. Furthermore, the data were accumulated and smoothed with a 5-year moving average to relate them to variations in salinity.

Finally, the influence of the NAO on the atmospheric and hydrographic parameters was examined. The winter DJF NAO index by Tim Osborne (updated from Jones et al., 1997) was used for this purpose. Correlation coefficients were calculated between the DJF NAO index and atmospheric and hydrographic parameters, which have been averaged over DJF and detrended beforehand.

3. Results

3.1. Trends and variability of temperature, salinity and oxygen

Figure 2 provides an overview of the range of variability in temperature, salinity and oxygen for the subdivisions 24, 25, 28 and 32 over the considered time periods. As depicted in the 5% and 95% percentiles, the range in which 90% of the observed and modelled values are located can be identified along the entire depth profile. The strongest fluctuations can be observed in temperature (Figure 2 left panels), es-

pecially in the top 20—30 m of each subdivision. Values here vary approximately between 0°C and 20°C which is caused by the annual cycles in SST. Comparing the temperature percentiles based on ICES data with those based on BSIOM output (Figure 2, left panels), it is noticeable that both the mean depth profiles and the ranges of variability coincide very well in all subdivisions.

The stratification of the water column is clearly visible in the salinity profiles (Figure 2 middle panels). In the upper layer, the salinity is in the range of approximately 4—8 g kg^{-1}, with decreasing values along the path from SD 24 to SD 32. Much higher salinities can be found at the bottom with up to 20 g kg^{-1} in the Arkona and Bornholm Basin. A strong salinity gradient between these two layers marks the depth of the halocline. In the Arkona Basin, the halocline is shown at a depth of about 30—40 m. Here, the increase in salinity gradient is somewhat more pronounced in the ICES data than in the model. For the Bornholm Basin (SD 25), the salinity profiles of the ICES and BSIOM data are in very good agreement. The halocline can be identified in this SD at a depth of 50—60 m. In SD 28, the location of the halocline in the model is slightly higher than in observation. It is located at a depth of about 50—60 m in the model and 65—75 m in the observations.

In all subdivisions, the layer above the halocline is nearly homohaline, while salinity in the lower layer continues to increase with depth. Fluctuations in salinity at the surface and in the area of the halocline are very small compared to variations in temperature and oxygen in all subdivisions. The 5% and 95% percentiles are close together in these areas and differ by a maximum of about 1—2 g kg^{-1} (except in the Arkona Basin, where the range of variation can also be larger). In SD 24 and 25, the percentiles fan out at the bottom. Here, variations in salinity are dictated by irregular inflows of highly saline water from the North Sea in combination with subsequent periods of stagnation.

Oxygen profiles (Figure 2 right panels) reflect the stratification defined by salinity. Above the halocline, the oxygen content is highest and almost constant with depth in all subdivisions. However, the absolute values can vary here in the range of 6—10 ml l^{-1}, which is related to the annual cycles in oxygen at the surface. The variability is less pronounced in the area of the halocline, while the 5% and 95% percentiles fan out again at the bottom due to inflow events. Mean profiles and variability ranges of oxygen are captured very well by the Baltic Sea model. Especially in SD 24 and 25, the percentiles based on ICES and BSIOM data match almost perfectly. In the Gulf of Finland, the observed bottom oxygen concentrations seem to be higher than the modelled.

A comparison between the observational data and model output for the temporal evolution of temperature, salinity and oxygen profiles for subdivisions 24, 25, 28 and 32 are presented in Appendix A (Figure A1 to Figure A4). These figures clearly show the annual cycles in temperature and oxygen at the sea surface. Furthermore, the varying depth of the halocline and the associated 2-layer structure of the water column can be seen (Figure A2 and Figure A3). The distribution and temporal development of temperature, salinity and oxygen are well captured by the model. Irregular major Baltic inflows (e.g. 1970, 1976, 1993, 2003 and 2014—2016), which are accompanied by a strong increase in salinity, but also changes in temperature and oxygen, are represented in both, observations and Baltic Sea model data.

In the following, we take a closer look at the trends and variations of temperature, salinity, and oxygen. It should be noted that the calculated trends from the observational data can be easily biased by missing observations at the beginning of the period. We calculated the trends for both observational and model data and found significant deviations in some cases. Therefore, in the following text, we mainly focus and rely on model-based trends.

3.1.1. Trends and variations in temperature

The time series of sea surface temperature with the mean annual cycle subtracted (Figure 3) show high interannual variability for the whole Baltic Sea. In some months the monthly mean temperature deviates from the mean annual cycle up to ±4°C (Figure 3, upper panel). To see how well the presented variations based on ICES and BSIOM data agree, correlation coefficients were determined. For the 3-month filtered SST data, the coefficients range from 0.68 in the Gulf of Finland to 0.87 in the Arkona and Bornholm Basin. Therefore, the data sets agree very well at the surface and the correlations are even better when annual averages of the SSTs are formed ($r = 0.9$ to 0.96).

Linear trends of SST are significantly positive in all subdivisions considered (see Table 2). Annual mean SST has increased with a rate of about 0.3°C $decade^{-1}$ in SD 24, SD 25 (period 1956—2018) and SD 28 (period 1959—2018), and with a higher rate of 0.4°C $decade^{-1}$ in the Gulf of Finland. For SD 32, however, it is important to take the shorter time period (1977—2018) into account. Warming trends of annual mean SST based on ICES observational data and BSIOM output coincide well. Linear trends over seasonally averaged sea surface temperature show stronger warming in summer than in winter (Table 2).

The 10-year window moving average of SST (Figure 3, upper panel) indicates that the warming trend is not constant over the entire period. In SD 24, SD 25 and SD 28, no distinct warming is evident in the first 25 years of the period. A continuous increase in SST can only be identified from about 1984 onwards. This is shown by observational data as well as in the Baltic Sea model. The correlation coefficients between the 10-year filtered data are high ($r = 0.8$ to 0.9). While the variability and linear trends of sea surface temperature are quite similar in all four subdivisions, there are differences between the basins in the remaining depth profile. In the Arkona Basin, the interannual variability of temperature after removing the annual cycle is still high down to the bottom. A different pattern of temperature variations is formed at the bottom of the Bornholm and Gotland Basin. There is less interannual variability, but irregular peaks in temperature associated with inflow events (Figure 3, lower panel). This can be observed particularly well with the BSIOM output, which shows weaker variations.

In general, the correlations between ICES and BSIOM data at the bottom of SD 25 and 28 are lower than at the surface ($r \approx 0.4$). In the Gotland Basin, the temperature fluctuations at the bottom are even smaller and less frequent than in SD 25, which can be seen both in the observation and in the model (see Figure A3). Interannual variability dominates again at the bottom of the Gulf of Finland, which is more pronounced in the ICES data than in the BSIOM data.

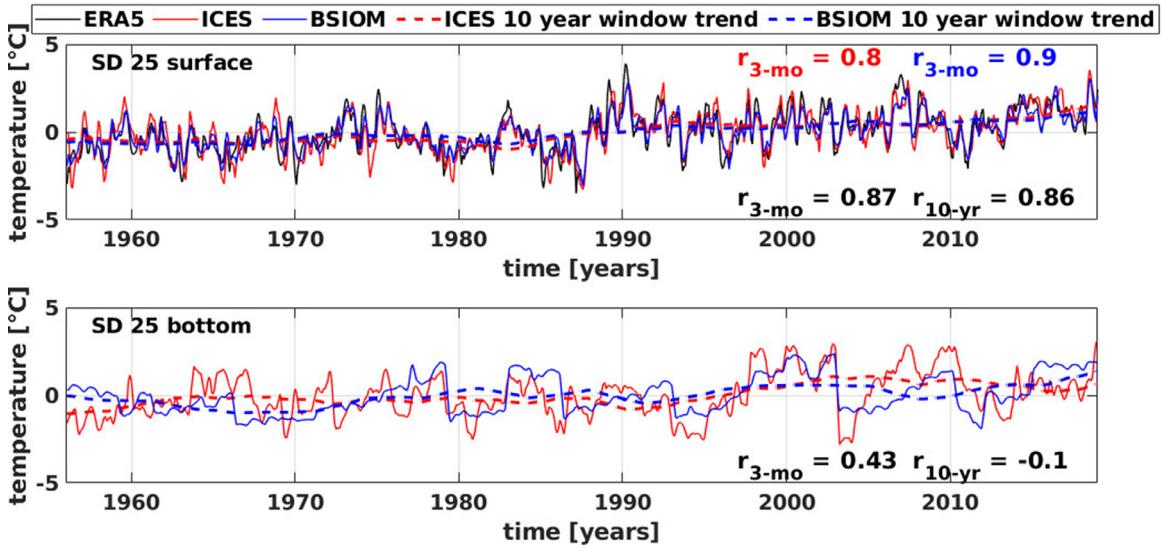

Figure 3 Anomalies from the annual cycle of 2 m air temperature (solid, black), sea surface and bottom temperature based on 3-month filtered ERA5 data, ICES observational data (solid, red) and BSIOM model output (solid, blue) for SD 25 and the period 1956—2018. Dashed lines show the 10-year moving average. Correlation coefficients are given for the correlation between 3-month ($r_{3\text{-mo}}$) and 10-year ($r_{10\text{-yr}}$) filtered BSIOM & ICES data, and between 3-month filtered ICES & ERA5 data ($r_{3\text{-mo}}$, red) and BSIOM & ERA5 data ($r_{3\text{-mo}}$, blue).

Table 2 Linear trends of SST (0—10 m) and 2 m air temperature in [°C decade^{-1}] for annual and seasonal (DJF — December, January, February; MAM — March, April, May; JJA — June, July, August; SON — September, October, November) means over the entire period. See Table 1 for the considered periods of each subdivision. SST trends are based on ICES observational and BSIOM model data, air temperature trends are based on ERA5 data. * indicates trends that are not statistically significant (5% level).

		Annual mean	DJF	MAM	JJA	SON
Arkona Basin (SD 24)	ICES	0.36	0.09*	0.41	0.62	0.29
	BSIOM	0.25	0.23	0.33	0.27	0.16
	ERA5	0.34	0.33	0.42	0.3	0.29
Bornholm Basin (SD 25)	ICES	0.3	0.11*	0.41	0.45	0.22
	BSIOM	0.27	0.23	0.34	0.34	0.17
	ERA5	0.33	0.33	0.38	0.32	0.26
Gotland Basin (SD 28)	ICES	0.28	0.13	0.26	0.46	0.28
	BSIOM	0.28	0.24	0.28	0.34	0.26
	ERA5	0.33	0.37	0.34	0.34	0.3
Gulf of Finland (SD 32)	ICES	0.39	0.18*	0.24	0.53	0.57
	BSIOM	0.4	0.25	0.25	0.54	0.52
	ERA5	0.62	0.76	0.6	0.64	0.47

Temperature trend profiles are presented in Figure 4. It is noticeable that all temperature trend profiles lie above zero. This means that the entire water column in the Baltic Sea is warming. However, the warming is mostly not homogeneous throughout the water column. All subdivisions have in common that temperature trends are strongest at the surface and tend to decrease with depth. In the Arkona Basin, BSIOM data show a trend of about 0.3°C decade^{-1} at the surface which decreases to about 0.2°C decade^{-1} below. In the Gotland and Bornholm Basin, a layered structure is shown in the ICES data with a trend minimum above the halocline (at about 40 m depth) and a maximum at the depth of the halocline itself (at about 60 m depth). The data thus indicate that warming is strongest at the surface and in the area of the halocline and lowest above the halocline and at the bottom. A deviating structure is shown by the model in SD 25 and 28 because the BSIOM data have a minimum temperature trend in the area of the halocline. At the bottom, however, the simulated and observed trends coincide very well again with rates of 0.25°C decade^{-1} in SD 25 and 0.15°C decade^{-1} in SD 28. The Gulf of Finland has a similar trend structure to that in the Arkona Basin. Temperature trends decrease from 0.5°C decade^{-1} at the surface to 0.2°C decade^{-1} at the bottom. There is no seasonality in temperature trends in the deep layer in most of the areas.

3.1.2. Trends and variations in salinity

At the surface, the interannual variability of salinity is very low. This is especially true for the Bornholm and Gotland Basin and the Gulf of Finland (Figure 5, upper panel). Correlations between ICES and BSIOM surface salinity are weaker than those observed in sea surface temperature in all sub-

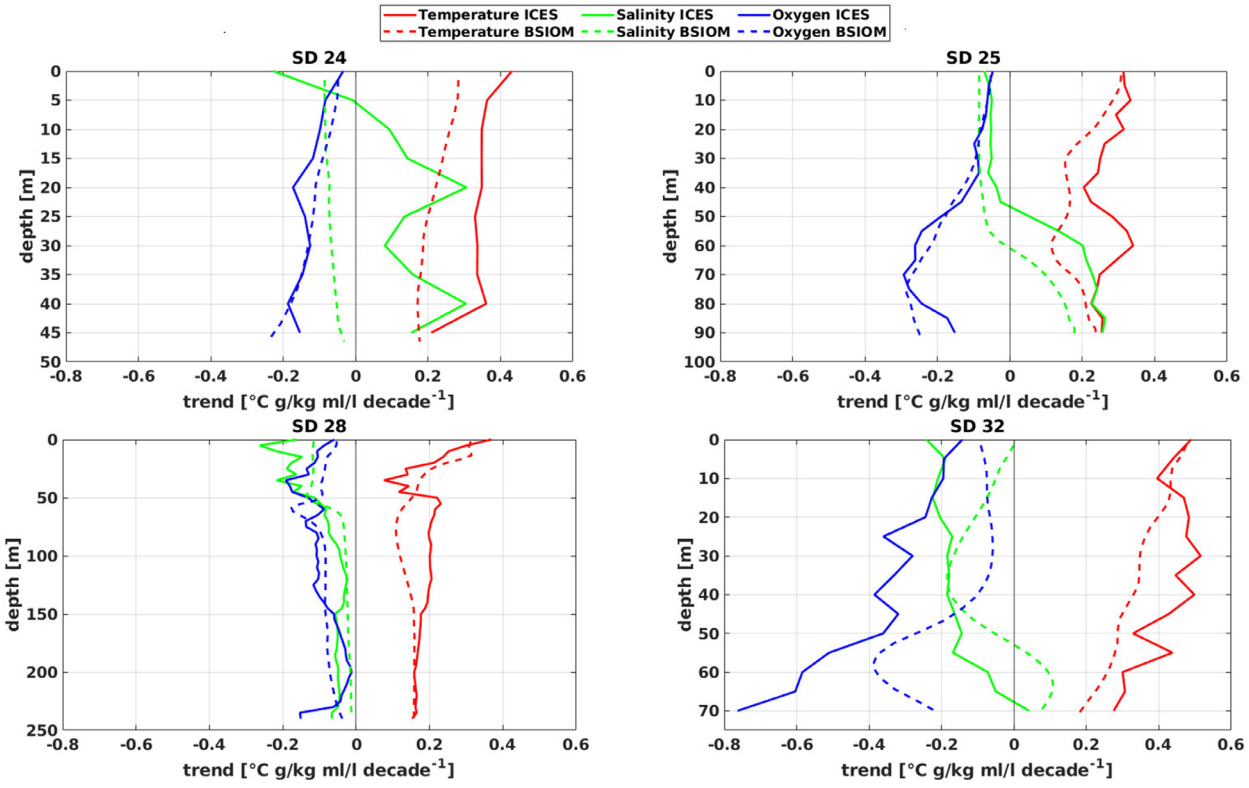

Figure 4 Trends per decade of temperature, salinity and oxygen for SD 24 (period 1956—2018), SD 25 (period 1956—2018), SD 28 (period 1959—2018) and SD 32 (period 1977—2018) based on ICES observational data (solid line) and BSIOM model output (dashed line).

divisions. Correlation coefficients are between 0.4 and 0.5 for the 3-month filtered data as well as for the annual mean data in SD 24 and SD 32. The data sets in SD 25 and 28 agree much better (see Figure 5, upper panel). Here, the correlation coefficients are 0.68 and 0.76 for the 3-month filtered surface salinity and between 0.8 and 0.9 for annual mean values.

A decrease in salinity at the surface can be observed in all subdivisions (Table 3). Linear trends over the entire period show a significant decrease of 0.05—0.08 g kg^{-1}

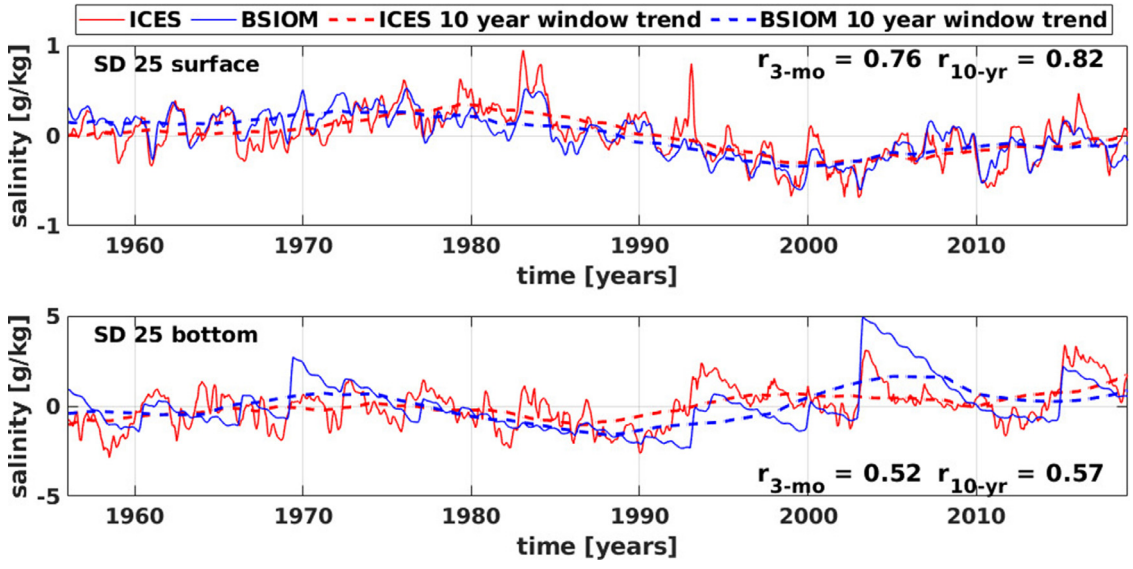

Figure 5 Anomalies of surface salinity (upper panel) and bottom salinity (lower panel) based on 3-month filtered ICES observational data (solid, red) and BSIOM model output (solid, blue) for SD 25 and the period 1956—2018. Dashed lines show the 10-year moving average. Correlation coefficients are given for the correlation between 3-month ($r_{3\text{-mo}}$) and 10-year ($r_{10\text{-yr}}$) filtered BSIOM & ICES data.

Table 3 Linear trends of surface salinity (0—10 m) in [g kg^{-1} decade^{-1}] for annual and seasonal (DJF, MAM, JJA, SON) means over the entire period. See Table 1 for the considered periods of each subdivision. * indicates trends that are not statistically significant (5% level).

		Annual mean	DJF	MAM	JJA	SON
Arkona Basin (SD 24)	ICES	−0.05	0.07*	−0.08	−0.12	−0.07
	BSIOM	−0.08	−0.07	−0.08	−0.1	−0.08
Bornholm Basin (SD 25)	ICES	−0.06	−0.06	−0.06	−0.06	−0.06
	BSIOM	−0.08	−0.08*	−0.08	−0.08	−0.09*
Gotland Basin (SD 28)	ICES	−0.21	−0.14	−0.25	−0.28	−0.19
	BSIOM	−0.12	−0.11	−0.11	−0.12	−0.12
Gulf of Finland (SD 32)	ICES	−0.21	−0.19	−0.18	−0.22	−0.26
	BSIOM	−0.03	−0.02*	−0.02*	−0.02*	−0.03*

decade^{-1} in the Arkona and Bornholm Basin. The trends based on the Baltic Sea model and the observational data match closely here. As can be seen in Table 3, the negative salinity trends prevail in all seasons and no significant differences in the seasonal cycle are pronounced in SD 24 and SD 25. In the eastern Gotland Basin, the model shows stronger freshening trends of 0.12 g kg^{-1}, but no significant freshening is visible in the Gulf of Finland from BSIOM data. The ICES data show a much stronger freshening in these areas. However, this might be an artificial signal due to the irregularity in the data.

The 10-year moving average of surface salinity anomalies (Figure 5, upper panel) shows a pronounced decadal variability in SD25. This can also be observed in SD 24 and SD 28 (not shown). Increasing salinities can be seen from the beginning of the period until the end of the 1970s and early 1980s in these areas. Thereafter, the surface salinity decreases until about 2000, where a minimum is shown in SD 25, SD 28 and in the BSIOM data of SD 24. Since then a slight increase in the data can be observed again. In the Bornholm and eastern Gotland Basin, the 10-year window trends based on ICES data correlate very well with those based on BSIOM output ($r = 0.82$ for SD 25 and $r = 0.9$ for SD 28). In the Gulf of Finland, the 10-year filtered ICES surface salinity data show a permanent decrease throughout the period, which is more pronounced at the beginning until about 1990.

In the area of the halocline of SD 25 and 28, the 10-year window trend of salinity shows a strongly declining salinity from 1980 onwards with a striking minimum around 1992. This minimum is also clearly depicted in the salinity profiles of Figure A3. At the bottom, strong peaks of salinity due to major inflow events can be observed at irregular intervals in SD 25 and 28 (Figure A2, Figure A3, Figure 5 lower panel). Particularly strong inflow events can be observed e.g. in 1970 and 2003, where the salinity anomaly is quickly raised by up to 5 g kg^{-1} in the deep layer of the Bornholm Basin. There is a complete lack of strong salinity peaks between 1983 and 1993. The Baltic Sea model shows fewer salinity inflows than the ICES data in the Bornholm and Gotland Basin. However, the particularly strong inflow events are represented very closely by the model.

Both data sets indicate a decadal variability of large saltwater inflows with a period of about 30 years through their 10-year moving average in SD 25 (see Figure 5, lower panel) and SD 28. However, the investigated time period is too short to conclude a regular variability with such a period.

A similar pattern can be observed in the 10-year moving averaged bottom salinity of the Gulf of Finland. Here, however, it is not the irregular peaks due to major inflows that dominate the deep layer salinity, but a pronounced interannual variability (Figure A4). In the Arkona Basin as well, interannual salinity variations at the bottom are high and the decadal variability, on the other hand, is very weak.

From the salinity trend profiles in Figure 4, it becomes clear that the long-term trends behave differently at the bottom than at the surface. While declining salinity trends can be observed in the upper layer, the tendency in the deep layer is towards positive trends. The difference is most obvious in the Bornholm Basin. Below the halocline, there are significant positive trends of about 0.2 g kg^{-1} decade^{-1}. In the Gotland Basin and the Gulf of Finland, no increase in the deep layer salinity can be observed over the entire period, but trends are almost zero. The ICES and BSIOM salinity trend profiles in the Arkona Basin deviate from each other. While the Baltic Sea model shows a slight decrease throughout the entire water column, the observational data indicate an increase of salinity in the lower 40 m of the basin with maxima at 20 m and 40 m depths.

3.1.3. Trends and variations in oxygen

From Figure 6, a strong interannual variability of oxygen is noticeable in all subdivisions at the surface. Correlations between surface oxygen anomalies based on BSIOM and ICES data are highest in the Arkona and Bornholm Basin ($r \approx 0.6$, see Figure 6). In SD 28 and SD 32, the time series are less consistent ($r_{SD28} = 0.45$ and $r_{SD32} = 0.2$).

Table 4 shows a significant decrease in surface oxygen concentrations in the entire Baltic Sea over the period under consideration. Linear trends lie between −0.05 and −0.08 ml l^{-1} decade^{-1} in all subdivisions. Seasonal trends demonstrate a higher decline in surface oxygen concentrations in summer (from June to August) than in winter (Table 4). No particular decadal variability is evident in the 10-year window trend of the surface oxygen anomalies (Figure 6, upper panel). Similar to that in temperature, the 10-year moving average is close to zero and nearly constant until the mid-1980s, and only from then on, a clear decline can be observed. This pattern applies to all subdivisions and both hydrographic data sets. Overall, the variability and trends in surface oxygen are similar to those of temperature, since both parameters are linked by the change in solubility depending on varying water temperature.

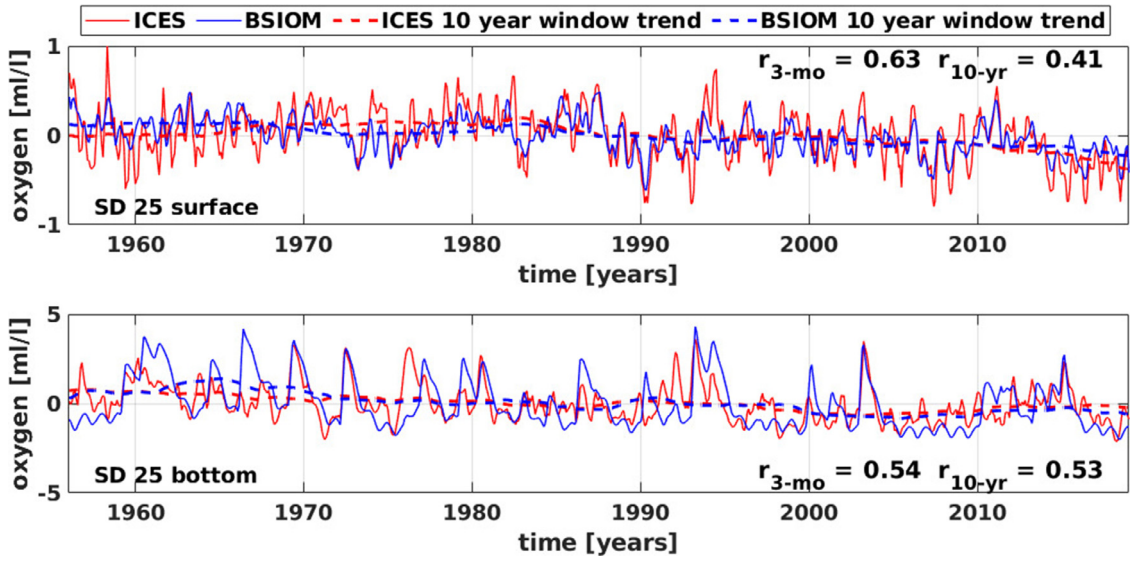

Figure 6 Anomalies of surface oxygen (upper panel) and bottom oxygen (lower panel) based on 3-month filtered ICES observational data (solid, red) and BSIOM model output (solid, blue) for SD 25 and the period 1956—2018. Dashed lines show the 10-year moving average. Correlation coefficients are given for the correlation between 3-month ($r_{3\text{-mo}}$) and 10-year ($r_{10\text{-yr}}$) filtered BSIOM & ICES data.

Table 4 Linear trends of surface oxygen (0—10 m) in [ml l^{-1} $decade^{-1}$] for annual and seasonal (DJF, MAM, JJA, SON) means over the entire period. See Table 1 for the considered periods of each subdivision. * indicates trends that are not statistically significant (5% level).

		Annual mean	DJF	MAM	JJA	SON
Arkona Basin (SD 24)	ICES	—0.07	0.02*	—0.07	—0.12	—0.05
	BSIOM	—0.05	—0.05	—0.07	—0.06	—0.03
Bornholm Basin (SD 25)	ICES	—0.05	0*	—0.08	—0.08	—0.03
	BSIOM	—0.05	—0.05	—0.07	—0.06	—0.03
Gotland Basin (SD 28)	ICES	—0.08	—0.05	—0.03	—0.15	—0.09
	BSIOM	—0.05	—0.05	—0.05	—0.06	—0.04
Gulf of Finland (SD 32)	ICES	—0.16	—0.14	—0.17	—0.21	—0.13
	BSIOM	—0.07	—0.05	—0.04	—0.09	—0.09

In the area of the halocline, variations of oxygen are stronger than at the surface. In addition to strong interannual variability, the 10-year moving average shows a pronounced minimum around 1970 and a maximum around 1990 in the Bornholm and eastern Gotland Basin. This pattern is similar to that of salinity in the same depth but reversed. It is also evident from the oxygen profiles in Figure A3.

At the bottom, there are large differences between the oxygen time series of the individual subdivisions: while interannual variations dominate in the Arkona Basin, only irregular fluctuations cause variations of oxygen in SD 25 and SD 28 (Figure 6, lower panel, Figure A1—A3), which can be related again to inflow events from the North Sea. Anomalies with peaks up to 4 ml l^{-1} can be observed with high frequency in the Bornholm Basin. Here, the BSIOM output shows more frequent fluctuations than the ICES observational data. For example, no marked fluctuations can be observed in the ICES data for the period 1980—1993, but there are some in the Baltic Sea model (Figure 6). This is reflected in the correlation coefficient between the two data sets, which is about 0.5 in the bottom oxygen in SD 25. However, both data sets have in common that the intensity and frequency of such oxygen anomalies have decreased since mid-1990. In the eastern Gotland Basin, the oxygen concentration at the bottom is zero most of the time (see Figure A3). Only a few inflows can raise the oxygen content here to about 2 ml/l for a short time (e.g. in 1970, 1993 and 2003). The Gulf of Finland shows a strong interannual signal in bottom oxygen concentration again. Just as in the area of the halocline of the other basins, the 10-year moving average has a pronounced maximum around 1990 at the bottom of SD 32.

The oxygen trend profiles (Figure 4) are negative in all subdivisions and across the entire water column. The decrease in oxygen is weakest at the surface and tends to increase with depth. At the bottom of the Arkona Basin, a decrease in oxygen up to —0.2 ml l^{-1} $decade^{-1}$ can be seen. In SD 25, there is a maximum decrease with —0.3 ml l^{-1} $decade^{-1}$ at 70 m depth. BSIOM data and ICES observations agree almost exactly here (Figure 4, upper right). A smaller maximum with about —0.2 ml l^{-1} $decade^{-1}$ is shown in the eastern Gotland Basin at 40 m depth with the ICES data and at about 60 m with the BSIOM data. The strongest trend can be observed at about 60 m depth in the Gulf of Finland,

where BSIOM data show an oxygen decrease up to −0.2 ml l^{-1} $decade^{-1}$. No remarkable seasonality is shown in the negative oxygen trends in the deep layer of the Baltic Sea.

3.1.4. Correlations between the variations in temperature, salinity and oxygen

In order to investigate more closely whether there are connections between the described variations in temperature, salinity and oxygen that indicate common forcing factors, the time series were correlated with each other. At the surface, strong anticorrelations were found between the 3-month filtered temperature and oxygen anomalies, which is not surprising due to their connection by solubility. This connection is particularly pronounced in the Baltic Sea model output with correlation coefficients of −0.98 in all subdivisions. The ICES data show slightly lower correlations ($r = -0.6$ to -0.7) between surface temperature and oxygen time series.

In the depth of the halocline, a particularly negative correlation ($r = -0.9$ in ICES and $r = -0.96$ in BSIOM data) between salinity and oxygen anomalies is noticeable in SD 28 and SD 32. Low salinities are associated with high oxygen concentrations and vice versa. This observation can be explained by the vertical movement of the halocline. Oxygen conditions deteriorate at a given depth as the halocline rises. In the Bornholm Basin, this relationship is also visible, but not that pronounced ($r = 0.5$ in ICES and BSIOM data).

3.2. Analysis of the atmospheric influence on the Baltic Sea hydrography

3.2.1. Impact of the air temperature

As can be seen in Figure 3, the air temperature anomalies from the annual cycle fit very precisely with the SST anomalies in SD 25 over the entire time period. The correlation coefficient between ICES SST and air temperature is 0.8, and 0.9 between BSIOM SST and air temperature in this basin, as well as in the Arkona Basin. In SD 28, the correlations are slightly lower and lowest in the Gulf of Finland with $r \approx 0.6$ between air temperature and ICES SST, and $r \approx 0.7$ with the BSIOM surface temperature. From the seasonally averaged time series of SD 32 (not shown), it becomes clear that the differences in sea surface and air temperature are particularly pronounced in winter (from December to February). Significantly higher correlations are determined with annual mean anomalies of the sea surface and air temperature. The correlation coefficients lie then predominantly between 0.9 and 0.98 in all subdivisions.

Table 2 shows that temperature trends in the period from 1950 to 2018 are very similar in the atmosphere and the sea surface in all subdivisions. The long-term trend of air temperature in the Arkona, Bornholm and eastern Gotland Basin for the period 1956/59–2018 is about 0.33°C $decade^{-1}$ (see Table 2). A significantly stronger trend in air temperature is noticeable in the Gulf of Finland for the period 1977–2018. With a rate of 0.62°C $decade^{-1}$, the atmospheric warming is higher than observed in the water temperature in this area. Seasonally, the trend of air temperature is strongest from December to February in SD 32 (0.76°C $decade^{-1}$, see Table 2). Also in the eastern Gotland Basin, the strongest atmospheric warming takes place in winter (DJF). In SD 24 and SD 25, however, the maximum trends are observed from March to May. The trends are weakest in all subdivisions from September to November.

3.2.2. Impact of the freshwater inflow

Figure 7 (upper panel) shows the annual mean river runoff into the Baltic Sea. For the period 1959–2018, the total mean river discharge was 15.5×10^3 m^3 s^{-1}. No long-term trend can be observed in the runoff for this period, but there are alternating dry and wet periods lasting for a couple of years to a decade. Particularly wet periods can be observed between 1969 and 1976 or between 2002 and 2009 (orange ranges in Figure 7). The runoff was above the mean value during 1978–1990 and 1996–2002 (green ranges). When comparing the runoff time series with the volume averaged salinity of SD 28, we notice that salinity clearly decreased during periods with anomalous strong runoff and increased during dry periods. As described above, particularly strong saltwater inflow events followed by high peaks in the deep layer salinity of SD 28 could be observed in 1970 and 2003 (see Figure A3). These major Baltic inflows lie exactly in the periods with low runoff to the Baltic Sea and are responsible for the increase in average salinity from Figure 7. In contrast, no strong saltwater inflows were observed in the eastern Gotland Basin during the wet periods. In the 5-year filtered zonal wind speed (Figure 7, middle panel), positive anomalies can be observed during both the particularly wet and dry periods. Especially in the period 1979–1990, a strong increase in zonal wind speed is striking.

The observed influence of river runoff into the Baltic Sea on variations in salinity on decadal timescales is confirmed

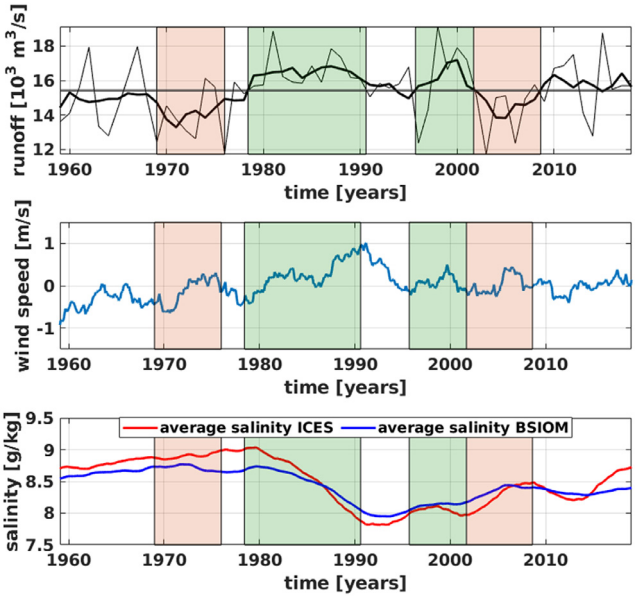

Figure 7 Upper panel: Annual mean river runoff to the Baltic Sea (thin line). In addition, the 5-year moving average (thick line) and the total mean for the period 1959–2018 (horizontal line) are shown. Middle panel: Zonal wind speed anomaly for SD 24 based on ERA5 data, smoothed with a 5-year moving average. Lower panel: Volume averaged salinity smoothed with a 5-year moving average based on ICES (red) and BSIOM (blue) data for SD 28. The green (orange) shaded ranges indicate periods with positive (negative) anomalous runoff.

Table 5 Correlation coefficients between accumulated anomalies of runoff to the Baltic Sea (inverted) and sea surface salinity and volume averaged salinity respectively. All-time series are smoothed with a 5-year moving average. * indicates correlations that are not statistically significant (5% level). Values with footnotes indicate higher correlations when a time lag is considered. The footnote represents the lag in years.

		SD 24		SD 25		SD 28		SD 32	
Surface salintiy	ICES	0.86		0.79		0.84		0.23*	
	BSIOM	0.59	0.67[3]	0.63	0.69[3]	0.80	0.81[2]	0.27*	
Volume averaged salinity	ICES	0.44		0.52	0.60[2]	0.71	0.81[3]	0.44	
	BSIOM	0.59	0.73[4]	0.55	0.78[4]	0.67	0.79[4]	0.48	0.50[1]

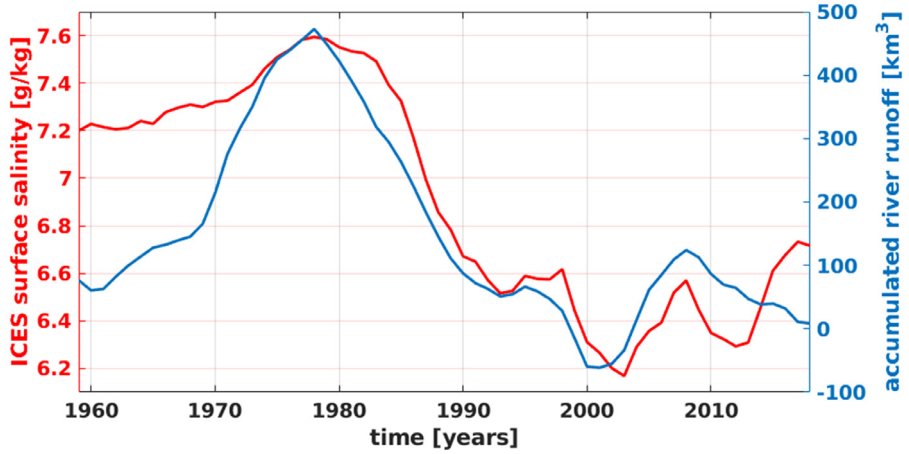

Figure 8 Sea surface salinity (0—10 m) filtered with a 5-year moving average of SD 28 for the period 1959 to 2018 based on ICES data and 5-year filtered accumulated anomalies of runoff of the Baltic Sea (inverted). The correlation coefficient is 0.84.

by correlation calculations. Correlation coefficients were determined between the accumulated runoff anomaly and the volume averaged and surface salinity of each subdivision (Table 5). For the volume averaged salinity, the correlation is highest in the eastern Gotland Basin ($r \approx 0.7$ when no lag is considered). It is remarkable that higher coefficients ($r \approx 0.8$) are obtained when a lag of 2—4 years is taken into account. Here, the runoff anomaly precedes the change in salinity and the correlations become significantly worse with a shift in the other direction. Even higher correlations can be seen between the accumulated river runoff anomaly and salinity at the surface. The relationship with surface salinity in the eastern Gotland Basin is illustrated in Figure 8. However, high correlation coefficients are obtained not only in SD 28 but also in the Arkona and Bornholm Basin at the surface (Table 5). In general, correlations with surface salinities based on the BSIOM model output are smaller than with the ICES data. Better correlation coefficients were obtained for the model data when a lag of 2—3 years was considered. Again, the runoff anomaly precedes the change in salinity. In the Gulf of Finland, there is no significant correlation between surface salinity and accumulated river runoff.

3.2.3. Impact of the NAO

The winter NAO index for the period 1956—2018 is presented in Figure 9. It is noticeable that positive and negative phases of the NAO alternate at irregular intervals of usually several years. First, direct correlations between the winter NAO index and variations in temperature, salinity and oxygen are investigated. Significant correlations are observed between the winter NAO index and sea surface temperature anomalies in SD 24, SD 25 and SD 28 (see Table B1). The coefficients range between 0.5 and 0.6 and decrease from the western to eastern basins. From Figure 9 it is clear that especially the positive NAO phases coincide well with positive temperature anomalies. A slightly weaker and negative correlation ($r \approx -0.4$ to -0.6) can be seen between the NAO index and the surface oxygen anomalies in these basins. An influence of the NAO on surface salinity can only be detected in the Arkona Basin (Table B1). Again, mainly the positive NAO phases are associated with increasing surface salinity in SD 24. The negative anomalies match less (see Figure 9).

In the surface layer of SD 32, no impact of the NAO is evident. The influence of the NAO is also not clear in the deeper layers of the Baltic Sea. Correlation coefficients are mostly low or not statistically significant. However, a striking pattern can be observed in the area of the halocline in SD 28 as well as at the bottom of SD 32 for the period from 1983 to the end of the 1990s: the positive NAO phases are associated with a strongly negative salinity and positive oxygen anomaly (see Figure B1). In the remaining period, this correlation is not clear, so the correlation coefficients are weak ($r = -0.3$ and $r = 0.3$ respectively).

In addition, the influence of the NAO on atmospheric parameters over the Baltic Sea in winter was investigated (not shown). The impact on the temperature in 2 m height and zonal wind speed is very pronounced. Positive (negative) NAO phases are associated with positive (negative) temperature and wind speed anomalies. The correlation coefficients are 0.7 for both temperature and zonal wind speed in

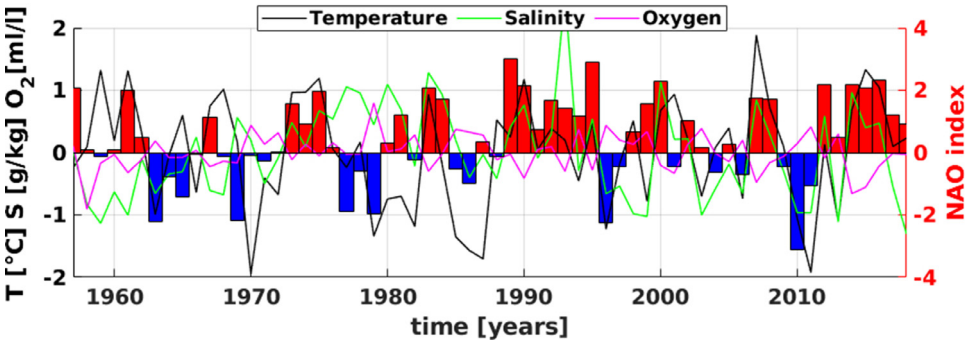

Figure 9 Winter (DJF) NAO index (bars) for the period 1956—2018 and DJF-mean temperature (black), salinity (green), oxygen (magenta) at the surface (0—10 m) based on ICES data for SD 24.

all subdivisions. For precipitation, the correlation is weaker: in the Bornholm Basin there is no statistically significant correlation at all, and the strongest relationship can be found in the Gulf of Finland ($r = 0.53$).

4. Discussion

In the present paper, we provide a detailed overview of the variations of temperature, salinity and oxygen in the Baltic Sea that can be observed in the period 1950 to 2020. The results of both hydrographic data sets investigated, ICES observational data and BSIOM model output, coincide well in the selected subdivisions. There are high interannual variations in sea surface temperature which closely follow variations in air temperature. On interannual time scales, the NAO strongly controls the variability of the sea surface and air temperature in winter. Linear trends over the period from 1950 to 2020 show significantly increasing sea surface and air temperatures of about 0.3 to 0.4°C decade^{-1} in all subdivisions studied. The trends are significantly stronger since the mid-1980s compared to the first half of the observation period. Increasing water temperatures can not only be observed at the sea surface but throughout the entire water column in the Baltic Sea. In salinity, pronounced variability on annual and decadal timescales is indicated during the period 1950 to 2020. Decadal variations of surface salinity are strongly controlled by the accumulated river runoff, which can explain about 70% of the variability. In the deep layer salinity, the decadal variability is associated with variations in saltwater import from the North Sea, which in turn are influenced by river runoff and the prevailing wind conditions. The long-term trends over the period 1950—2020 show a freshening of the upper layer and stagnating or increasing salinities in the deep layer of the Baltic Sea. This trend pattern in salinity is associated with a rising of the halocline and a strengthening of the stratification across the halocline. Surface oxygen depicts strong variations on annual and interannual timescales that are strongly anti-correlated with the SST due to solubility. Linked to the rising temperatures, the oxygen is significantly decreasing during the period 1950—2020 in the Baltic Sea with stronger trends since the mid-1980s. Additionally, eutrophication intensifies both the primary production of organic matter and oxygen consumption needed for its degradation (HELCOM, 2009; Lehmann et al., 2014b).

Trends and variations in temperature, salinity and oxygen for different time periods and regions of the Baltic Sea have already been the subject of several studies. High correlations between SST and air temperature in the Baltic Sea and a strong link with the NAO index in winter were also found by e.g. Bradtke et al. (2010), Janssen (2002) and Tinz (1996). The observed trends in sea surface temperature are consistent with earlier estimates as well: 0.3°C decade^{-1} in the southeastern Baltic Sea for the period 1960—2015 (Rukšėnienė et al., 2017) and 0.5°C decade^{-1} for the period 1982—2016 (Liblik and Lips, 2019). Calculations of SST trends from satellite measurements since the beginning of the 1980s show a greater increase in the northern areas of the Baltic Sea (i.e. Gulf of Bothnia, Gulf of Finland, northern Baltic Proper) than in the rest of the basin (Bradtke et al., 2010; Lehmann et al., 2011; Liblik and Lips, 2019). As noted by previous studies (e.g. Liblik and Lips, 2019; Stramska and Białogrodzka, 2015), the warming trends in SST are stronger in summer than in winter (Table 2). Furthermore, our results show that besides the surface, especially in and within the halocline a strong warming exists. This is probably related to the inflow of water from the North Sea that has also warmed at the surface. However, vertical movement of the halocline could also play a role.

Opposite salinity trends for the upper and deep layers of the Baltic Sea were also observed by Liblik and Lips (2019). For the period 1982—2016, they detected a freshening of the upper layer and increasing salinity in the deep layer of the Baltic Sea with comparable magnitudes. However, this trend pattern is not consistent with the findings of Zorita and Laine (2000), who reported a homogeneous evolution of salinity in the entire water column for the period 1962—1996. The contradictory results can be related to the different periods considered and the pronounced decadal variability in both the upper and lower layer salinity. As shown in this work, the decadal variability of the surface salinity is strongly linked to the accumulated river runoff (Table 5, Figure 8). Periods of increased river runoff are followed by lower surface salinities and vice versa.

The influence of river discharge on salinity in the Baltic Sea is the subject of numerous studies (e.g. Liblik and Lips, 2019; Meier and Kauker, 2003; Radtke et al., 2020; Winsor et al., 2001). Liblik and Lips (2019) cannot explain all the decadal variability of surface salinity by accumulated river runoff, since the two quantities do not correlate well in their observations between 2002 and 2009

(see their Figure 9). Instead, they suggest that decadal changes in vertical salt flux contribute as well. In our observations, however, the courses of accumulated river runoff and surface salinity match closely between 2002 and 2009 (Figure 8). This could indicate that vertical salt flux might play a smaller role in decadal surface salinity changes than assumed by Liblik and Lips (2019). However, further investigations are needed to clarify this question. As noted by Radtke et al. (2020), we can see the impact of river runoff not only on surface salinity but also on the occurrence of MBIs: strong inflow events occurred in periods of reduced river runoff and fewer in periods of enhanced runoff. High correlation coefficients between accumulated river runoff and volume-averaged salinity (Table 5) support this observation. It is noticeable that the correlations with volume-averaged salinity are higher when lags of 2—4 years are considered (runoff precedes salinity changes). The time lag confirms the indirect influence, since changes in deep layer salinity only occur when the inflow water from the Kattegat has spread along the topography.

Our results are furthermore in agreement with Meier and Kauker (2003), who explained about 50% of the decadal changes in mean salinity by accumulated runoff anomalies. However, they found that another significant part of the decadal variability of mean salinity is caused by the low-frequency variability of zonal wind speed. Enhanced zonal wind over the Baltic Sea is linked with intensified precipitation over the catchment and increased river runoff to the Baltic, and reduces the activity of strong saltwater inflows at the same time (Meier and Kauker, 2003). This connection is also indicated in our results (Figure 7), which show that zonal wind speeds over the Arkona Basin are exceptionally high during periods of increased runoff and decreasing mean salinity in the Baltic Sea. However, it is still unclear whether the changes in saltwater inflow activity are related to changes in runoff, or whether an atmospheric pattern can be identified that influences river runoff and inflow activity independently.

We further observed that the zonal wind speed over the Baltic Sea is strongly controlled by the NAO (Table B1). This suggests that the NAO also has an influence on the volume exchange with the North Sea. However, correlations between the winter NAO index and salinity anomalies in the Baltic Sea are mostly not clear in our observations. Lehmann et al. (2002) studied the impact of NAO on water exchange with the North Sea (independent of the salinity of the water) and found a clear relation: a high positive phase of the NAO is related to increased inflows into the Baltic Sea and a negative NAO favours outflow conditions. In this case, it is important to note that inflow into the Baltic Sea does not only mean major Baltic inflows, which increase the bottom salinity in the Baltic Sea but also inflows with lower salinity, which cannot be detected in our salinity time series. This could explain why we have difficulties in identifying the influence of the NAO on salinity changes in the Baltic Sea.

As also noted by Zorita and Laine (2000), we observed decadal variability in oxygen in the area of the halocline of the Bornholm and eastern Gotland Basin and at the bottom of the Gulf of Finland, which is strongly anti-correlated to the decadal variability in salinity in these areas. There is a pronounced minimum in salinity around 1990 in these areas, which can be linked to the absence of MBIs during 1983—1993 and the associated weakening of the halocline. In the Gulf of Finland, the halocline vanished completely during this time. Due to mixing, oxygen-rich water from the upper layer can then reach greater depths. However, since the 1990s, salinity increased again in these areas, which has resulted in a strong oxygen decrease in the last decades. Maximum negative trends up to -1 ml l^{-1} decade^{-1} in the area of the halocline (eastern Gotland Basin) have also been reported by Lehmann et al. (2022).

For the assessment of the results, it is important to briefly point out the main limitations or uncertainties of both data sets. The Baltic Sea model has a limited horizontal (2.5 km) and vertical resolution (3 m), and approximations (e.g. hydrostatics, incompressibility) are applied in the model. Accordingly, the simulation of vertical mixing processes is restricted, which could be a reason for the underestimated depth of the halocline by BSIOM in the eastern Gotland Basin and for differing structures in the trend profiles. Furthermore, we observed fewer salinity peaks at the bottom of SD 28 with BSIOM data (Figure A3), suggesting that the exact spread of water masses in the deep layer is difficult to model. The simplified bottom topography of the model could play a role here. A relatively simple approach is used for modelling oxygen consumption in the water column, which does not resolve the complex biogeochemical cycle. Nevertheless, the variability and distribution of oxygen overall are well represented by the Baltic Sea model. The ICES observational data, on the other hand, do not correspond exactly to reality either. Data density in individual months and subdivisions can vary greatly. The data are more representative if there are many measurements in a month, which were taken over the entire subdivision and not only at a few stations. Especially in the northern subdivisions, it must be assumed that fewer measurements were taken in winter than in summer due to ice coverage. This can explain differences in the seasonal trends between ICES and BSIOM data. For example, ICES observational data show a much stronger decrease in surface salinity than the model data in SD 28. This might be partly related to a lack of measurements in the Gulf of Riga at the beginning of the time period. Fewer measurements in winter may also be the reason for the stronger haline stratification shown in the model compared to the observational data in the Gulf of Finland. When the Gulf of Finland is covered with ice in winter, the water below is protected from interactions with the atmosphere, which could cause stronger stratification of the water column. In addition, the accuracy of the measured values might not be consistent over the time period, as different methods were used (CTD and bottle measurements).

Various processes in the Baltic Sea itself, but also influences from its surrounding and the atmosphere have different effects on changes in the hydrography. We were able to explain some of the variations through atmospheric influences and the impact of river runoff. However, there are still many open questions that are worth further investigation in the future. For example, what hydrographic variations can be observed on larger timescales than presented here? In this context, Börgel et al. (2018) already indicate that the Atlantic Multidecadal Oscillation can play an important role and have an impact on salinity in the Baltic Sea, although this should be investigated in more detail.

Appendix A. Time series of temperature, salinity and oxygen

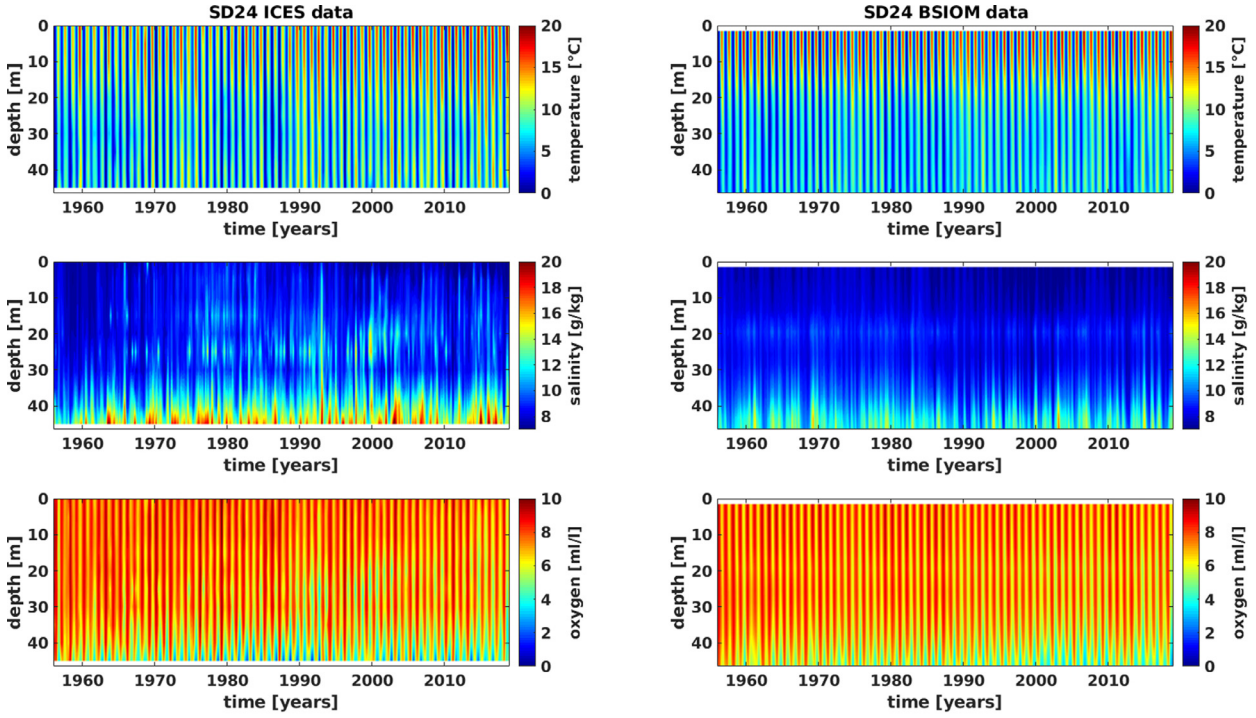

Figure A1 Time series of temperature, salinity and oxygen profiles based on monthly means of ICES observational data (left panels) and BSIOM model output (right panels) of SD 24 (Arkona Basin) for the period 1956—2018. The monthly mean data are filtered with a 3-month moving average.

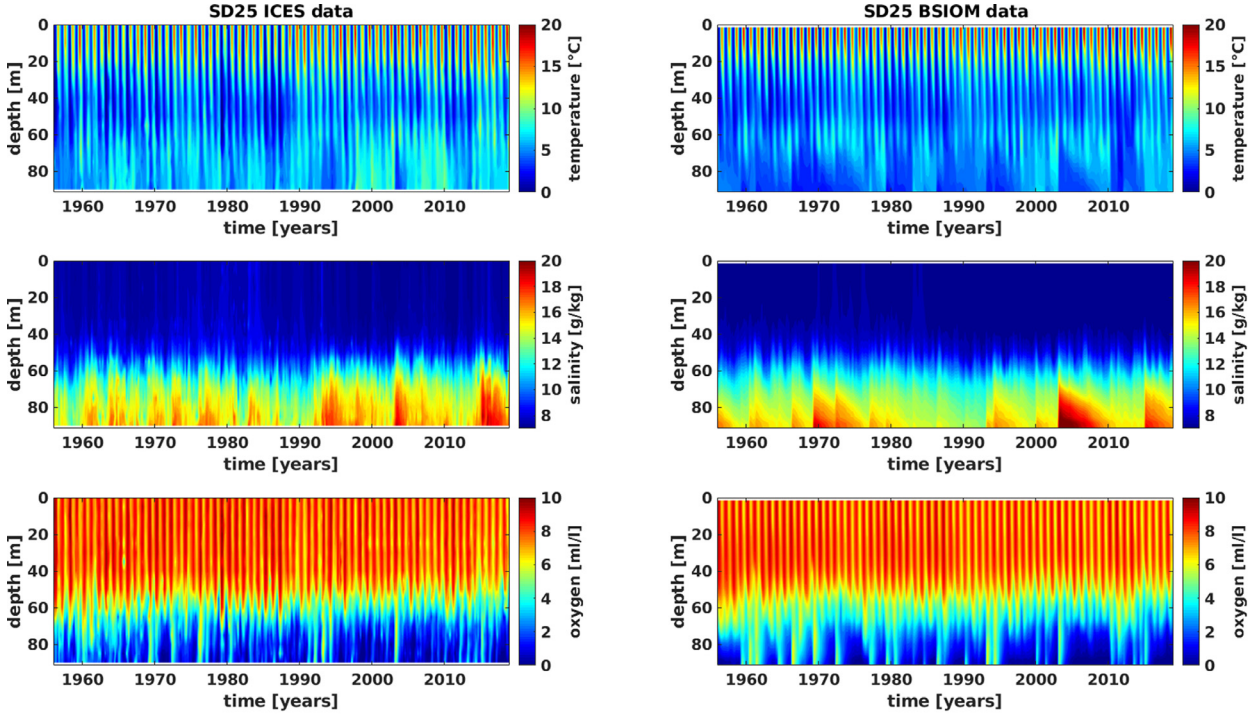

Figure A2 Time series of temperature, salinity and oxygen profiles based on monthly means of ICES observational data (left panels) and BSIOM model output (right panels) of SD 25 (Bornholm Basin) for the period 1956—2018. The monthly mean data are filtered with a 3-month moving average.

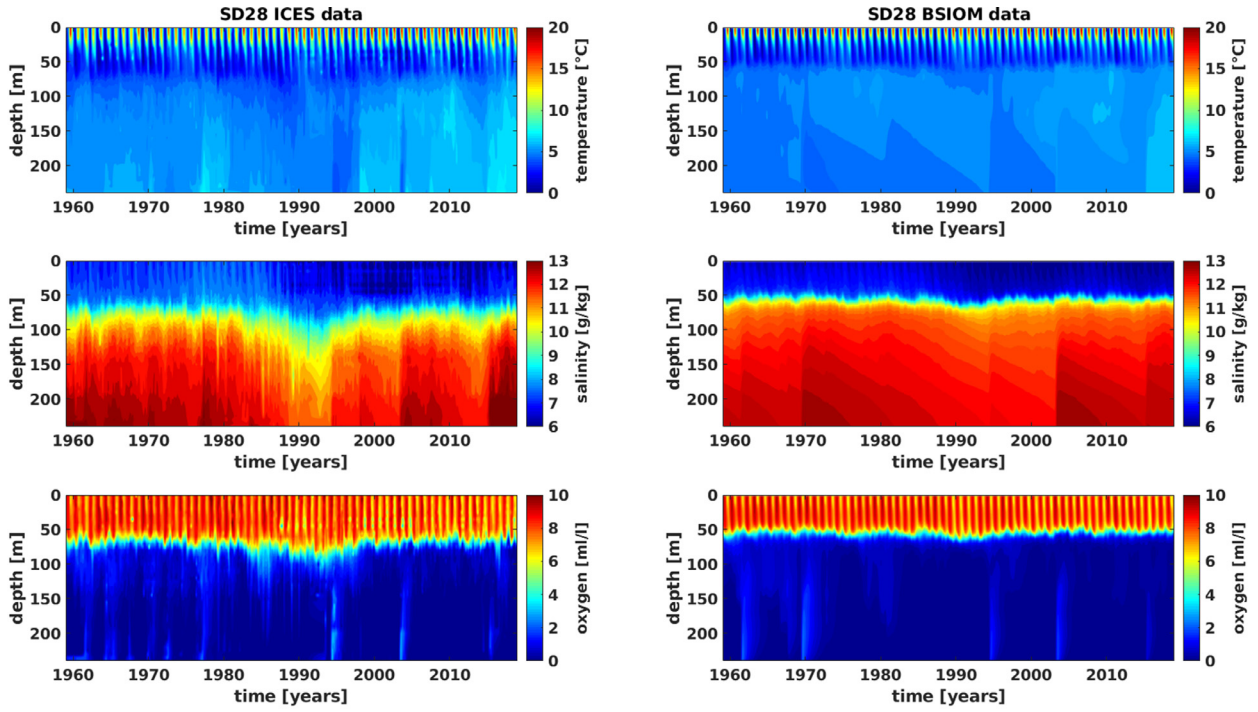

Figure A3 Time series of temperature, salinity and oxygen profiles based on monthly means of ICES observational data (left panels) and BSIOM model output (right panels) of SD 28 (Eastern Gotland Basin) for the period 1959—2018. The monthly mean data are filtered with a 3-month moving average.

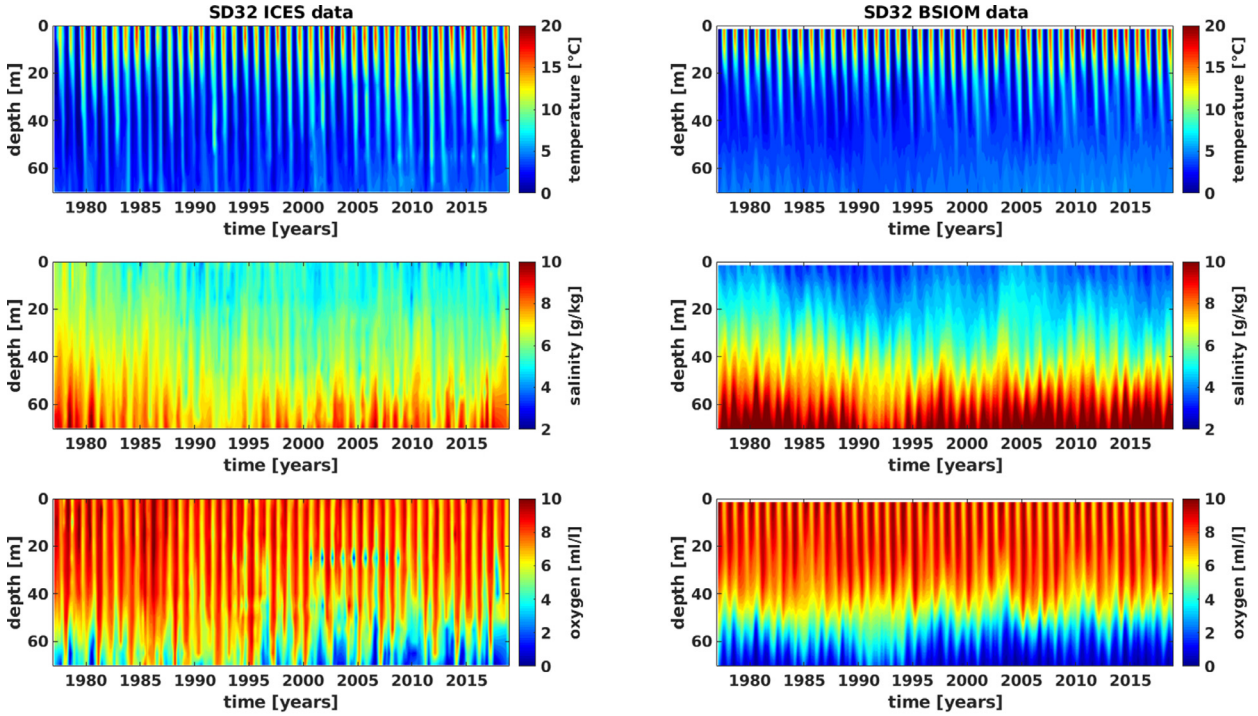

Figure A4 Time series of temperature, salinity and oxygen profiles based on monthly means of ICES observational data (left panels) and BSIOM model output (right panels) of SD 32 (Gulf of Finland) for the period 1977—2018. The monthly mean data are filtered with a 3-month moving average.

Appendix B. Correlations with the NAO index

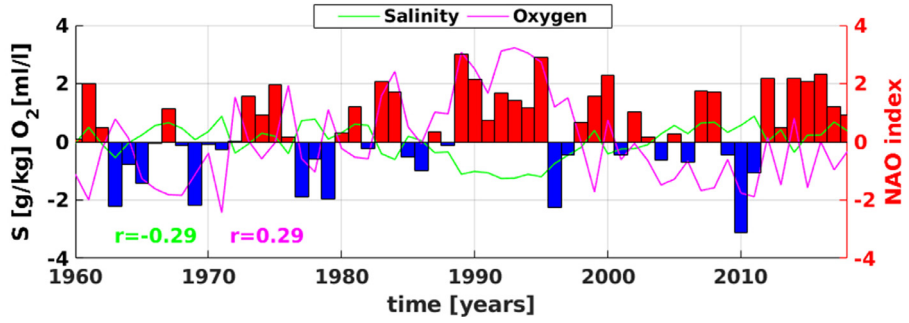

Figure B1 Winter (DJF) NAO index (bars) for the period 1959—2018 and DJF-mean salinity (green) and oxygen (magenta) in the area of the halocline based on ICES data for SD 28 (eastern Gotland Basin). In addition, the correlation coefficients between the NAO index and the salinity and oxygen time series are given. They are significant at the 5% level.

Table B1 Correlation coefficients between winter (DJF) NAO index and hydrographic parameters at the surface based on ICES and BSIOM data and atmospheric parameters based on ERA5 data. All-time series are averaged over DJF. * indicate correlations that are not statistically significant (5% level).

		SD 24	SD 25	SD 28	SD 32
Surface temperature	ICES	0.53	0.55	0.41	0.27*
	BSIOM	0.59	0.53	0.52	0.19*
Surface salinity	ICES	0.36	0.31	−0.23*	−0.13*
	BSIOM	0.41	0.2*	0.03*	−0.21*
Surface oxygen	ICES	−0.44	−0.44	0.29	−0.02*
	BSIOM	−0.61	−0.55	−0.53	−0.03*
2 m air temperature	ICES	0.71	0.70	0.69	0.69
Zonal wind speed	BSIOM	0.73	0.73	0.69	0.72
Precipitation	ERA5	0.28	0.16*	0.28	0.53

References

Andersson, H.C., 2002. Influence of long-term regional and large-scale atmospheric circulation on the Baltic sea level. Tellus A 54, 76—88. https://doi.org/10.3402/tellusa.v54i1.12125

BACC I Author Team, 2008. Assessment of climate change for the Baltic Sea basin. Springer Science & Business Media.

BACC II Author Team, 2015. Second assessment of climate change for the Baltic Sea Basin. Springer Open.

Bell, B., Hersbach, H., Simmons, A., Berrisford, P., Dahlgren, P., Horányi, A., Muñoz-Sabater, J., Nicolas, J., Radu, R., Schepers, D., Soci, C., Villaume, S., Bidlot, J., Haimberger, L., Woollen, J., Buontempo, C., Thépaut, J., 2021. The ERA5 global reanalysis: Preliminary extension to 1950. Q. J. Roy. Meteor. Soc. 147, 4186—4227. https://doi.org/10.1002/qj.4174

Börgel, F., Frauen, C., Neumann, T., Schimanke, S., Meier, H.E.M., 2018. Impact of the Atlantic multidecadal oscillation on Baltic Sea variability. Geophys. Res. Lett. 45, 9880—9888.

Bradtke, K., Herman, A., Urbanski, J.A., 2010. Spatial and interannual variations of seasonal sea surface temperature patterns in the Baltic Sea. Oceanologia 52 (3), 345—362.

Bumke, K., Karger, U., Hasse, L., Niekamp, K., 1998. Evaporation over the Baltic Sea as an example of a semi-enclosed sea. Contrib. Atmos. Phys. 71 (2), 249—261.

Carstensen, J., Andersen, J.H., Gustafsson, B.G., Conley, D.J., 2014. Deoxygenation of the Baltic Sea during the last century. P. Natl. Acad. Sci. USA 111, 5628—5633. https://doi.org/10.1073/pnas.1323156111

Hänninen, J., Vuorinen, I., Hjelt, P., 2000. Climatic factors in the Atlantic control the oceanographic and ecological changes in the Baltic Sea. Limnol. Oceanogr. 45, 703—710.

HELCOM, 2009. Eutrophication in the Baltic Sea. Baltic Sea Environ. Proc. 115B, 1—148.

Hurrell, J.W., 1995. Decadal trends in the North Atlantic Oscillation: Regional temperatures and precipitation. Science 269 (5224), 676—679.

ICES, 2022. https://www.ices.dk/Pages/default.aspx (accessed on: 29 April 2022).

Janssen, F., 2002. Statistische Analyse mehrjähriger Variabilität der Hydrographie in Nord-und Ostsee. Univ. Hamburg, Institute of Oceanography.

Johansson, J., 2016. HELCOM Baltic Sea Environment Fact Sheet 2016 — Total and Regional Runoff to the Baltic Sea.

Jones, P.D., Jónsson, T., Wheeler, D., 1997. Extension to the North Atlantic Oscillation using early instrumental pressure observations from Gibraltar and south-west Iceland. Int. J. Climatol. 17, 1433—1450.

Kniebusch, M., Meier, H.E.M., Neumann, T., Börgel, F., 2019a. Temperature Variability of the Baltic Sea Since 1850 and Attribution

to Atmospheric Forcing Variables. J. Geophys. Res. Ocean. 124, 4168—4187. https://doi.org/10.1029/2018JC013948

Kniebusch, M., Meier, H.E.M., Radtke, H., 2019b. Changing Salinity Gradients in the Baltic Sea As a Consequence of Altered Freshwater Budgets. Geophys. Res. Lett. 46, 9739—9747. https://doi.org/10.1029/2019GL083902

Lehmann, A., Getzlaff, K., Harlaß, J., 2011. Detailed assessment of climate variability in the Baltic Sea area for the period 1958 to 2009. Clim. Res. 46, 185—196. https://doi.org/10.3354/cr00876

Lehmann, A., Hinrichsen, H.-H., 2000. On the thermohaline variability of the Baltic Sea. J. Marine Syst. 25, 333—357. https://doi.org/10.1016/S0924-7963(00)00026-9

Lehmann, A., Hinrichsen, H.-H., Getzlaff, K., Myrberg, K., 2014. Quantifying the heterogeneity of hypoxic and anoxic areas in the Baltic Sea by a simplified coupled hydrodynamic-oxygen consumption model approach. J. Marine Syst. 134, 20—28. https://doi.org/10.1016/j.jmarsys.2014.02.012

Lehmann, A., Höflich, K., Post, P., Myrberg, K., 2017. Pathways of deep cyclones associated with large volume changes (LVCs) and major Baltic inflows (MBIs). J. Marine Syst. 167, 11—18. https://doi.org/10.1016/j.jmarsys.2016.10.014

Lehmann, A., Krauss, W., Hinrichsen, H.-H., 2002. Effects of remote and local atmospheric forcing on circulation and upwelling in the Baltic Sea. Tellus A 54, 299—316. https://doi.org/10.1034/j.1600-0870.2002.00289.x

Lehmann, A., Myrberg, K., Post, P., Chubarenko, I., Dailidiene, I., Hinrichsen, H.-H., Hüssy, K., Liblik, T., Meier, H.E.M., Lips, U., Bukanova, T., 2022. Salinity dynamics of the Baltic Sea. Earth Syst. Dynam. 13, 373—392. https://doi.org/10.5194/esd-13-373-2022

Lehmann, A., Post, P., 2015. Variability of atmospheric circulation patterns associated with large volume changes of the Baltic Sea. Adv. Sci. Res. 12, 219—225. https://doi.org/10.5194/asr-12-219-2015

Leppäranta, M., Myrberg, K., 2009. Physical Oceanography of the Baltic Sea. Springer, Berlin, Heidelberg. https://doi.org/10.1007/978-3-540-79703-6

Liblik, T., Lips, U., 2017. Variability of pycnoclines in a three--layer, large estuary: the Gulf of Finland. Boreal Environ. Res. 22, 27—47.

Liblik, T., Lips, U., 2019. Stratification Has Strengthened in the Baltic Sea — An Analysis of 35 Years of Observational Data. Front. Earth Sci. 7, 174. https://doi.org/10.3389/feart.2019.00174

Liblik, T., Naumann, M., Alenius, P., Hansson, M., Lips, U., Nausch, G., Tuomi, L., Wesslander, K., Laanemets, J., Viktorsson, L., 2018. Propagation of Impact of the Recent Major Baltic Inflows From the Eastern Gotland Basin to the Gulf of Finland. Front. Mar. Sci. 5, 222. https://doi.org/10.3389/fmars.2018.00222

MacKenzie, B.R., Schiedek, D., 2007. Daily ocean monitoring since the 1860s shows record warming of northern European seas. Glob. Change Biol. 13, 1335—1347. https://doi.org/10.1111/j.1365-2486.2007.01360.x

Matthäus, W., Schinke, H., 1999. The influence of river runoff on deep water conditions of the Baltic Sea. In: Biological, Physical and Geochemical Features of Enclosed and Semi-Enclosed Marine Systems. Springer, Dordrecht, 1—10. https://doi.org/10.1007/978-94-017-0912-5_1

Meier, H.E.M., Kniebusch, M., Dieterich, C., Gröger, M., Zorita, E., Elmgren, R., Myrberg, K., Ahola, M.P., Bartosova, A., Bonsdorff, E., Börgel, F., Capell, R., Carlén, I., Carlund, T., Carstensen, J., Christensen, O.B., Dierschke, V., Frauen, C., Frederiksen, M., Gaget, E., Galatius, A., Haapala, J.J., Halkka, A., Hugelius, G., Hünicke, B., Jaagus, J., Jüssi, M., Käyhkö, J., Kirchner, N., Kjellström, E., Kulinski, K., Lehmann, A., Lindström, G., May, W., Miller, P.A., Mohrholz, V., Müller-Karulis, B., Pavón-Jordán, D., Quante, M., Reckermann, M., Rutgersson, A., Savchuk, O.P., Stendel, M., Tuomi, L., Viitasalo, M., Weisse, R., Zhang, W., 2022. Climate change in the Baltic Sea region: a summary. Earth Syst. Dynam. 13, 457—593. https://doi.org/10.5194/esd-13-457-2022

Meier, M., Kauker, F., 2003. Modeling decadal variability of the Baltic Sea: 2. Role of freshwater inflow and large-scale atmospheric circulation for salinity. J. Geophys. Res. 108, 3368. https://doi.org/10.1029/2003JC001799

Mohrholz, V., 2018. Major Baltic Inflow Statistics — Revised. Front. Mar. Sci. 5, 384. https://doi.org/10.3389/fmars.2018.00384

Neumann, T., Radtke, H., Seifert, T., 2017. On the importance of Major Baltic Inflows for oxygenation of the central Baltic Sea. J. Geophys. Res. Ocean. 122, 1090—1101. https://doi.org/10.1002/2016JC012525

Omstedt, A., Rutgersson, A., 2000. Closing the water and heat cycles of the Baltic Sea. Meteorol. Zeitschrift 9, 59—60.

Radtke, H., Brunnabend, S.-E., Gräwe, U., Meier, H.E., 2020. Investigating interdecadal salinity changes in the Baltic Sea in a 1850—2008 hindcast simulation. Clim. Past 16, 1617—1642.

Rudolph, C., Lehmann, A., 2006. A model-measurements comparison of atmospheric forcing and surface fluxes of the Baltic Sea. Oceanologia 48 (3), 333—380.

Rukšėnienė, V., Dailidienė, I., Kelpšaitė-Rimkienė, L., Soomere, T., 2017. Sea surface temperature variations in the south-eastern Baltic Sea in 1960—2015. Baltica 30, 75—85. https://doi.org/10.5200/baltica.2017.30.09

Stramska, M., Białogrodzka, J., 2015. Spatial and temporal variability of sea surface temperature in the Baltic Sea based on 32-years (1982—2013) of satellite data. Oceanologia 57 (3), 223—235. https://doi.org/10.1016/j.oceano.2015.04.004

Stoicescu, S-T., Lips, U., Liblik, T., 2019. Assessment of Eutrophication Status Based on Sub-Surface Oxygen Conditions in the Gulf of Finland (Baltic Sea). Front. Mar. Sci. 6, 54. https://doi.org/10.3389/fmars.2019.00054

Tinz, B., 1996. On the relation between annual maximum extent of ice cover in the Baltic Sea and sea level pressure as well as air temperature field. Geophysica 32, 319—341.

Tronin, A., 2017. The satellite-measured sea surface temperature change in the Gulf of Finland. Int. J. Remote Sens. 38, 1541—1550. https://doi.org/10.1080/01431161.2017.1286057

Winsor, P., Rodhe, J., Omstedt, A., 2001. Baltic Sea ocean climate: an analysis of 100 yr of hydrographic data with focus on the freshwater budget. Clim. Res. 18, 5—15.

Zorita, E., Laine, A., 2000. Dependence of salinity and oxygen concentrations in the Baltic Sea on large-scale atmospheric circulation. Clim. Res. 14, 25—41. https://doi.org/10.3354/cr014025

Oceanologia 65 (2023) 484—493

Available online at www.sciencedirect.com

ScienceDirect

journal homepage: www.journals.elsevier.com/oceanologia

ORIGINAL RESEARCH ARTICLE

Bed forms under the combined action of waves and wind-driven currents in the remote foreshore of the non-tidal sea

Magdalena Stella-Bogusz*

Institute of Hydro-Engineering, Polish Academy of Sciences, Gdańsk, Poland

Received 30 June 2022; accepted 27 March 2023
Available online 18 April 2023

KEYWORDS
Wave-current interaction;
Sand wave height;
Sand wave length;
Bed forms characteristics

Abstract The paper presents a prediction of bed form parameters (length and height) in the remote foreshore of the non-tidal sea. The study site is located in the south Baltic region, near the Coastal Research Station (CRS) in Lubiatowo, Poland (ca. 1—2 Nm off the shoreline at depths of around 16—20 m). The study site is an area with hydrodynamics and lithodynamics typical of the south Baltic coast, built of fine sands. Predictions are based on numerical modelling with an input of measured data. Numerical modelling uses assumptions of specific relations of sand wave height and length with shear stress, grain size, kinematic viscosity, or storm event frequency. To establish these relations for the study area, wave, sea temperature and wind data were collected near CRS Lubiatowo. To verify the predictions made in this research, bathymetric data from a field survey in the study area was used. The results show that the flow is mostly current-dominated. Sand waves formed by hydrodynamic conditions in this area have a steepness of 0.01 to 0.02, a length of 40 to 70 m and a height of 0.6 to 2.3 m.

1. Introduction

Sea bottom features of various characteristics, such as subaqueous sand waves or ripples, influence roughness and flow conditions, and thus also sediment transport. Furthermore, large sand waves appearing or migrating on the sea bottom can create navigation hazards, undermine submarine pipelines or block intake valves. More detailed research on the morphology and dynamics of such bed forms will make it possible to reduce these potential risks and increase our

* Corresponding author at: Institute of Hydro-Engineering, Polish Academy of Sciences, Kościerska 7, 80—328 Gdańsk, Poland.
E-mail address: m.stella@ibwpan.gda.pl
Peer review under the responsibility of the Institute of Oceanology of the Polish Academy of Sciences.

Production and hosting by Elsevier

https://doi.org/10.1016/j.oceano.2023.03.001

understanding of sediment transport (Whitmeyer and Fitzgerald, 2008).

In the remote foreshore of a non-tidal sea, such as the Baltic Sea, where depths are between 15 and 20 m, sediment motion is possible and can be intense, but only under specific hydrodynamic conditions (Rudowski et al. 2008; Stella et al. 2019; Uścinowicz et al. 2014). Ostrowski et al. (2018) and Stella et al. (2019) proved that synergic nonlinear interaction between storm waves and wind-driven currents leads to intensive sediment transport. Stella (2021) showed that seabed level changes in this region usually vary between 0.3 and 0.5 m, but can reach up to 0.7 m. Additionally, Kubacka et al. (2016), Rudowski et al. (2008), Stella (2021) and Uścinowicz et al. (2014) pointed out the existence of larger and smaller seabed forms which migrate in the remote nearshore zone at depths of around 16—20 m.

The study aimed to investigate the characteristics of bed forms under the impact of wave- and wind-driven current interaction and to verify methods of predicting bed form magnitudes. Determining the dimensions of these structures will help in future research by providing information on what needs to be considered when modelling sediment transport in the remote foreshore of the non-tidal sea (especially when measured data is not available). Predicting the size of these "obstacles" to flow will make it possible to describe them more accurately. Verification of various prediction models allows the selection of the best possible method of calculating the height and length of bed forms. These studies are aimed at enriching the knowledge of the largest bed forms that may occur under given hydrodynamic conditions and of their average characteristics.

2. Study site

Measurements used in this article were made within a rectangular polygon in the South Baltic Sea, approximately 2.5 km from the Polish shore (Figure 1). A short distance inland from the shoreline, there is the Coastal Research Station (CRS) in Lubiatowo, which belongs to the Institute of Hydro-Engineering of the Polish Academy of Sciences (IBW PAN). The region is a typical Polish open sea coast with sandy beaches (Cerkowniak et al., 2017; Ostrowski et al., 2015). The height of the tides in the whole Baltic Sea is negligible. Therefore, hydrodynamic and lithodynamic processes are determined by waves and wind currents. Storm events have the greatest impact on the dynamics at depths analysed here (around 16—20 m). The study site can be considered representative of sandy shores not only in Poland but also in the entire south and southeast Baltic Sea.

Along the foreshore in the vicinity of Lubiatowo, the seabed slope is mildly contoured in an NNW direction with an average inclination of about 9° (to the 10 m isobath). The nearshore bathymetric layout is non-uniform, while further, up to 15 m depths, isobaths are parallel to the shore. In the cross-shore profile of the study site, there are 4 stable submerged sandbars at distances of 80—100, 150—180, 300—350, and 500—550 m from the shore (Szmytkiewicz et al., 2021). A grain analysis performed by Szmytkiewicz et al. (2021) showed that sediments on the sea bottom are composed mainly of fine-grained quartz sand with an average diameter d_{50} of around 0.22 mm. The analysis was performed on 46 samples taken from the area at depths of up to 14 m. According to Pruszak et al. (2008), the density of the ground skeleton of the seabed equals $\rho_s = 2650$ kg m^{-3}. The grain diameter of samples taken from the bottom within the polygon analysed in this paper is about 0.13 mm and the sediment is well sorted. The seabed at depths of around 18 m is built mainly of fine sand, with a little admixture of silt in some areas (Ostrowski and Stella, 2020; Stella et al., 2019).

3. Bed form characteristics

There are many ways to predict bed form characteristics under waves, but it is harder to predict their properties when currents are introduced. Depending on its strength, a current can either variously affect the height and length of sand waves (weak current) or completely change their type (strong current). Under interaction between waves and a weak current, sand waves exhibit mainly characteristics typical of wave bed form, sometimes with an asymmetric shape.

The characteristics of bed forms are influenced by the intensity of hydrodynamic processes as well as the angles of wave and current directions. For a wave-dominated flow, bed forms are symmetrical, with a steep crest and a gentle trough, whereas under current-dominated conditions, they are asymmetrical, with a gentle forward slope and a steep lee slope (Lu et al., 2015). When waves and currents are in dynamic equivalence, bed forms exhibit combined characteristics. In order to distinguish between different types of bed forms, Li and Amos (1998) used the factor $\frac{u_w^*}{u_c^*}$ represented by bed shear velocity for waves-only (u_w^*) and current-only (u_c^*) conditions. Current-dominated bed forms occur when $\frac{u_w^*}{u_c^*} < 0.75$, wave-current bed forms occur for $0.75 < \frac{u_w^*}{u_c^*} < 1.25$, wave-dominated bed forms appear when $1.25 < \frac{u_w^*}{u_c^*} < 2$, and pure wave bed forms develop when $2 < \frac{u_w^*}{u_c^*}$.

The angle between the waves and the current affects the shape of seabed forms. For example, Baas et al. (2021) showed that various angles between the waves and current flow lead to the formation of different types of ripples (such as ladder-back, tile-shaped or lunate interference ripples). Lacy et al. (2007) showed in their research that when the angle between the waves and the current decreases, the impact of the current on bed forms increases, and what is more, the three-dimensionality and irregularity of bed forms increase as well. The angle between the waves and the current affects the magnitude of shear stress. The non-linear wave-wind current interaction is strongest when the flow is collinear. When the current flows in the same or opposite direction as the propagation of the waves, maximum bed shear stresses are the same When the wave-current flow is orthogonal, shear stress has a completely different value. In such a case, the wave-current non-linear interaction is weakest (Malarkey and Davies, 1998).

Numerous laboratory studies (Southard, 1971; Southard and Boguchwal, 1990) and field investiga-

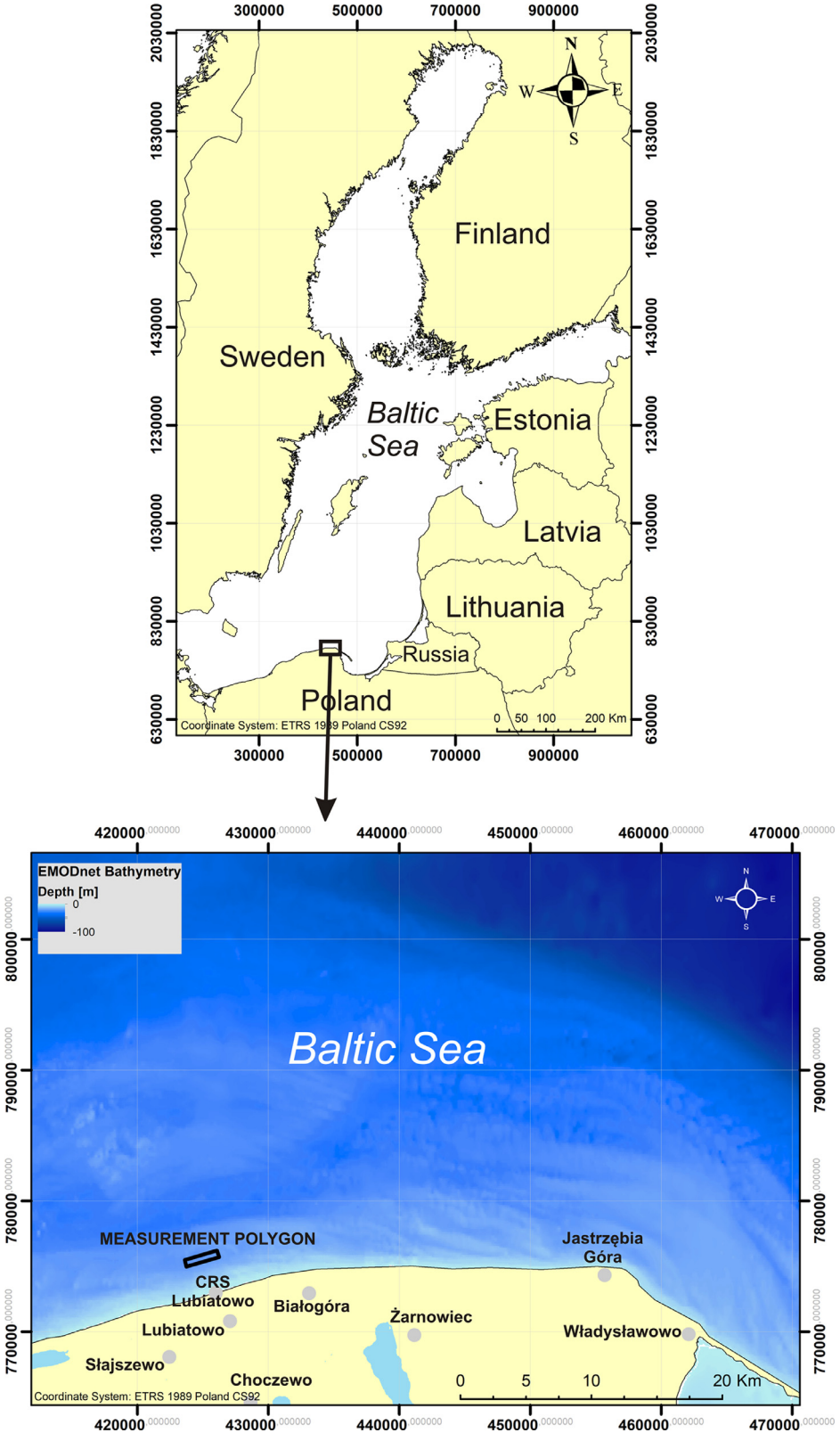

Figure 1 Study site with the measurement polygon (source of the bathymetry: https://portal.emodnet-bathymetry.eu/).

Table 1 Location of the edges of the study site area.

Point number	Location
1	54°50′14″N 17°48′37″E
2	54°49′57″N 17°48′45″E
3	54°50′22″N 17°51′03″E
4	54°50′38″N 17°50′54″E

Table 2 Input parameter values used in numerical modelling.

Parameter	Values
Grain size d_{50}	0.13 mm
Depth h	17 m
Storm event frequency σ_{se}	7 per year

tions (Aliotta and Perillo, 1987; Boothroyd and Hubbard, 1975; Dalrymple and Rhodes, 1995; Dalrymple et al., 1978; Gabel, 1993; Mazumder, 2003; McCave, 1971; van Rijn, 1984; Yalin, 1964; Zarillo, 1982) have been carried out to predict the size of sand waves. As a result of those studies, bed form morphology is defined as a function of flow depth, grain size and flow velocity or shear stress.

According to research by Gail (1990), in order to classify sedimentary structures, it is important to specify their physical characteristics. Another approach is based on size measured in terms of spacing (length). As bed form spacing is a continuum ranging from slightly less than 1 m to more than 1,000 m, arbitrary values of 5, 10 and 100 m are suggested to differentiate between “small”, “medium”, “large”, and “very large” forms. The ranges of bed form spacing and (calculated) mean heights are

λ= 0.6—5.0 m, η =0.075—0.4 m for small forms;
λ = 5.0—10.0 m, η = 0.4—0.75 m for medium forms;
λ = 10.0—100.0 m, η = 0.75—5.0 m for large forms;
λ => 100 m, η = > 5.0 m for very large forms.

4. Methods

4.1. Field measurements

Bathymetric measurements, side-scan sonar images and wave data were collected in an area where depths ranged between 16.4 and 20.6 m. The study polygon extends parallel to the shore, and its dimensions are 2.6 km × 0.53 km. The coordinates of the points defining the edges of the study site are given in Table 1.

4.1.1. Bathymetry and seafloor features

The bathymetry was measured with a multibeam sonar MultibeamResonSeaBat 7125 mounted on the bow of a boat during a research cruise in 2018. The device worked at a frequency of 400 kHz, and the accuracy of depth measurements was less than 1 cm. Prior to the bathymetric measurements, the speed of sound was measured in the water column at 0.5 m intervals, and the sonar was calibrated. During the cruise, 22 profile passes were made every 25 m, each 2500 m long. Leica SmartNet was used as the source for RTK corrections, and IXBlueOctans 1000 was used to support the positioning compensator. Positioning during the cruise was accurate to 2—5 cm. Images taken with a side-scan sonar Klein 3900 in November 2017 were also used in this study. During the survey, 15 profile passes were made at 40 m intervals. The device was towed on a cable line 6—9 m above the seabed, its frequencies were 445 kHz and 900 kHz, and the horizontal and vertical beam widths were 0.21°, 40°, respectively.

4.1.2. Waves

Wave conditions were measured using a Directional Waverider buoy DWR-7 Mk. III. The buoy was moored at a location around 1.5 Nm from the shore with coordinates 54°50′N and 17°50′E, where the depth was approximately 18 m. The measuring period lasted from Oct. 2017 to Oct. 2018. Variations in the water surface elevation were measured continuously for 17 minutes every hour, then processed and stored in a data logger. In addition, raw data and statistics were also transferred by radio to the receiver, then saved on a hard disk of a computer in CRS Lubiatowo. The measurements were taken with an accuracy of 0.01 m.

4.1.3. Wind

The wind parameters were collected near CRS Lubiatowo (54°48.70′N, 17°50.43′E) where a 22 m mast with a cup anemometer SW-48 (produced by MORS, Poland) is located. The distance between the mast and the shoreline is 150 m. Unfortunately, the presence of tree crowns a few meters below the measuring device caused additional roughness, making the wind parameters biased. Furthermore, the presence of trees and the distance of the mast inland from the sea reduce the wind speed compared to the wind blowing on the open sea. In order to minimize the measurement bias, Stella (2021) proposed a correction of the wind velocity. The method is based on the formula transforming the “land” wind speed (W_{land}) to the “sea” wind speed (W_{sea}) using the following equations:

$$W_{sea} = 1.76W_{land} + 1.92[m/s] \quad \text{for} \quad W_{land} > 1m/s \tag{1}$$

$$W_{sea} = 3.68W_{land} \quad \text{for} \quad W_{land} < 1m/s \tag{2}$$

4.2. Numerical modelling

Bed form characteristics were estimated and calculated using the MATLAB numerical computing environment on the basis of existing equations developed by Dalrymple et al. (1978), Flemming (1988), Hulscher (1996), Van Rijn (1984) and Yalin (1964) and adapted to the conditions of the remote foreshore of the Baltic Sea. The input parameters used in modelling are given in Table 2.

Measured current data were not available for that period, so they had to be estimated numerically based on wind velocities. Stella et al. (2019) developed and verified a model for calculating the mean wind-driven current from the wind-induced flow. Given that the wind-induced flow velocity in the surface layer is equal to 3% of the wind

Table 3 Mean monthly water temperature and kinematic viscosity.

Year	Month	T_{mean} — mean water temperature [°C]	ε — kinematic viscosity [m^2/s]
2017	10	12	1.24E-06
2017	11	9	1.35E-06
2017	12	5	1.53E-06
2018	1	3	1.63E-06
2018	2	2	1.68E-06
2018	3	1	1.74E-06
2018	4	5	1.53E-06
2018	5	9	1.35E-06
2018	6	14	1.18E-06
2018	7	19	1.04E-06
2018	8	22	9.65E-07
2018	9	18	1.06E-06
2018	10	15	1.15E-06

speed when that speed is up to 8 m/s and 3.5% for winds exceeding that speed, the distribution of velocity can be calculated. Stella et al. (2019) analysed cases in which the flow was dominated by a wind-induced current separately from those in which a wave-induced flow was dominant. In the former, the velocity distribution can be represented by a logarithmic vertical distribution. In the latter cases, the distribution is represented by a two-layered model of turbulent viscosity that leads to the logarithmic distribution of the flow within the thin nearbed layer but produces a linearly variable velocity in the water column. What is more, the model includes interaction between the waves and the current. As the presence of the wave bed boundary layer affects the wind-driven current through additional roughness, the estimations include a so-called apparent bottom roughness. More detailed descriptions of the steps leading to obtaining the wind-induced current velocity profile are given in a study by Stella et al. (2019).

In an area where depths are between 14—20 m, the wind-current direction is almost always the same as the direction of the wind, especially during storm events, Ostrowski et al. (2018). Hence, in calculations made for purposes of this research, it is assumed that the direction of the wind current is the same as that of the wind.

To estimate bed form types, the Li and Amos (1998) assumption was applied. Bed shear velocities for waves-only (u_w^*) and current-only (u_c^*) conditions were calculated on the basis of measurements performed within the study site between Oct. 2017 and Oct. 2018. The conclusion from research by Hulscher (1996) is that morphological forms at the sea bottom are closely related to the water's kinematic viscosity ε,. Hence, the wave length of a bed form can be estimated from the equation

$$\lambda = 0.16 \cdot 10^2 \sqrt{\frac{2\varepsilon}{\sigma_{se}}} \tag{3}$$

where σ_{se} is the frequency of storm events, and ε represents the kinematic viscosity of water. The magnitudes of ε are given in Table 3. The calculations of this parameter were based on the monthly mean temperature recorded by the wave buoy near CRS Lubiatowo. The storm frequency in the period from Oct. 2017 to Oct. 2018 amounted to 7 per year (when H_s exceeded a magnitude of 3.0 m). The magnitudes of kinematic viscosity and storm event frequency were used to calculate the sand wave length according to formula (3).

Van Rijn (1984) modelled the sand wave height based on the shear stress and grain size as follows:

$$\frac{\eta}{h} = 0.11\left(\frac{d_{50}}{h}\right)^{0.3}(1 - e^{-0.5T_s})(25 - T_s) \tag{4}$$

where h is the flow depth, η is the sand wave height, and $T_s = (\frac{\tau - \tau_{cr}}{\tau_{cr}})$, where τ is the shear stress, and τ_{cr} is the critical shear stress. The sand wave length depends only on the water depth according to the relation $\tau = 7.3h$. The assumption in this model is that no sand waves will develop when the magnitude of shear stresses is below the critical value, as there will be no sediment transport. Van Rijn's (1984) equation for η is true for $\tau < 26\tau_{cr}$ because, according to his study, after τ exceeds this value, all bed forms will be washed away. Yalin (1964), on the other hand, estimated the relationship between the bed form height and shear stress as follows:

$$\frac{\eta}{h} = \frac{1}{6}\left(1 - \frac{\tau_{cr}}{\tau}\right) \tag{5}$$

The critical shear stress corresponds to a Shield stress value of 0.05, denoting the incipient motion of sediment grains. Bed form heights were calculated using Van Rijn's relation of this parameter with shear stress and grain size as well as Yalin's (1964) relation of this parameter with shear stress. Published studies indicate that the height and length of sand waves are directly related. According to the height-spacing relationship determined by Flemming (1988):

$$\eta = 0.0677\lambda^{0.8089} \tag{6}$$

or Dalrymple et al. (1978):

$$\eta = 0.0635\lambda^{0.733} \tag{7}$$

The sand wave height was calculated on the basis of relations proposed by Dalrymple et al. (1978) and Flemming (1988) using Hulscher's wave length. In order to verify the estimations of bed form characteristics, cross-sections of bed forms observed in a bathymetry map (with a grid size of 0.2 m x 0.2 m) from 2018 were used (Figure 2).

5. Results

Several selected side-scan sonar images of the seabed with sand waves are presented in Figure 3.

The occurrence percentages of specified magnitudes of the relation between bed shear velocities for waves-only and current-only conditions are given in Table 4.

It appears that a current- and wave-current dominated flow occurred for most of the time (58%), which should have resulted in asymmetric bed forms with a gentle forward slope and a steep lee slope. However, during the remaining 42% of the time, conditions favoured the formation of wave-dominated and pure wave bed forms.

The predicted values of the sand wave length based on the kinematic viscosity and storm event frequency function and of the sand wave height after Van Rijn and Yalin are given in Table 5.

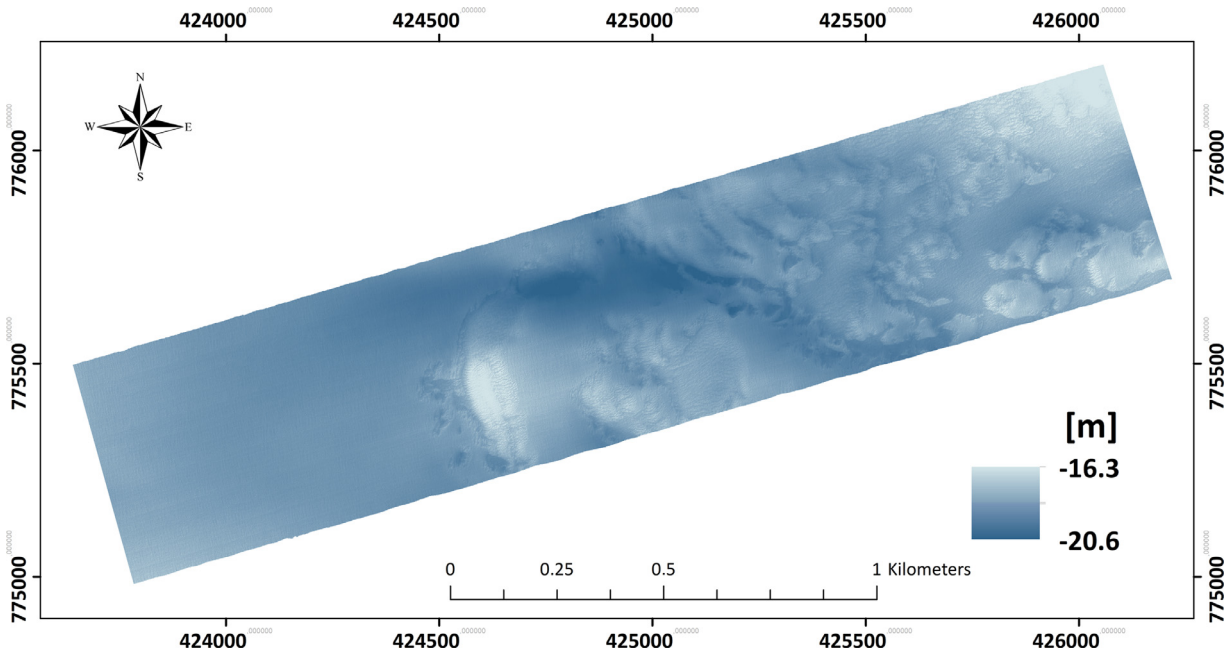

Figure 2 Bathymetry map. Multibeam sonar measurements of November 2017.

Table 4 Occurrence of different bed form types on the sea bottom between October 2017 and October 2018.

Magnitude of $\frac{(u_w^*)}{(u_c^*)}$	Occurrence percentage [%]	Bed forms type
<0.75	37	current-dominated
0.75—1.25	21	wave-current
1.25-2	11	wave-dominated
>2	31	pure wave

The computational results show that hydrodynamic conditions in 2017—2018 favoured the formation of bottom forms with a steepness of 0.01—0.02, with lengths from about 40 to 70 m and heights from 0.6 to 2.3 m. In order to verify the above estimations, cross-sections (Figure 4) of bed forms observed in a bathymetry map from 2018 were used.

Figure 4 shows that the length of sand waves varied from about 30 m to around 80 m, and their height was around 0.4 to 1.4 m. It can also be seen that some of the observed bed forms had one gentle slope and others a slightly steeper one.

The sand wave heights predicted according to Flemming (1988) and Dalrymple et al. (1978) using Hulsher's wave length are given in Table 6.

A comparison of the calculated sand wave heights with those observed in cross-sections suggests that both formulas overestimate this dimension, but the equation proposed by Dalrymple et al. (1978) gives better results than the one by Flemming.

Table 5 Sand wave length and height predictions.

Year	Month	λ Sand wave length [m]	η Van Rijn's sand wave height [m]	η Yalin's sand wave height [m]
2017	10	53.48	0.67	2.32
2017	11	55.80	0.72	2.07
2017	12	59.41	0.69	2.23
2018	1	61.32	0.73	1.97
2018	2	62.25	0.65	2.00
2018	3	63.35	0.68	2.03
2018	4	59.41	0.67	2.03
2018	5	55.80	0.59	1.60
2018	6	52.17	0.64	1.91
2018	7	48.98	0.66	1.77
2018	8	47.18	0.65	1.81
2018	9	49.45	0.65	2.03
2018	10	51.50	0.63	1.81

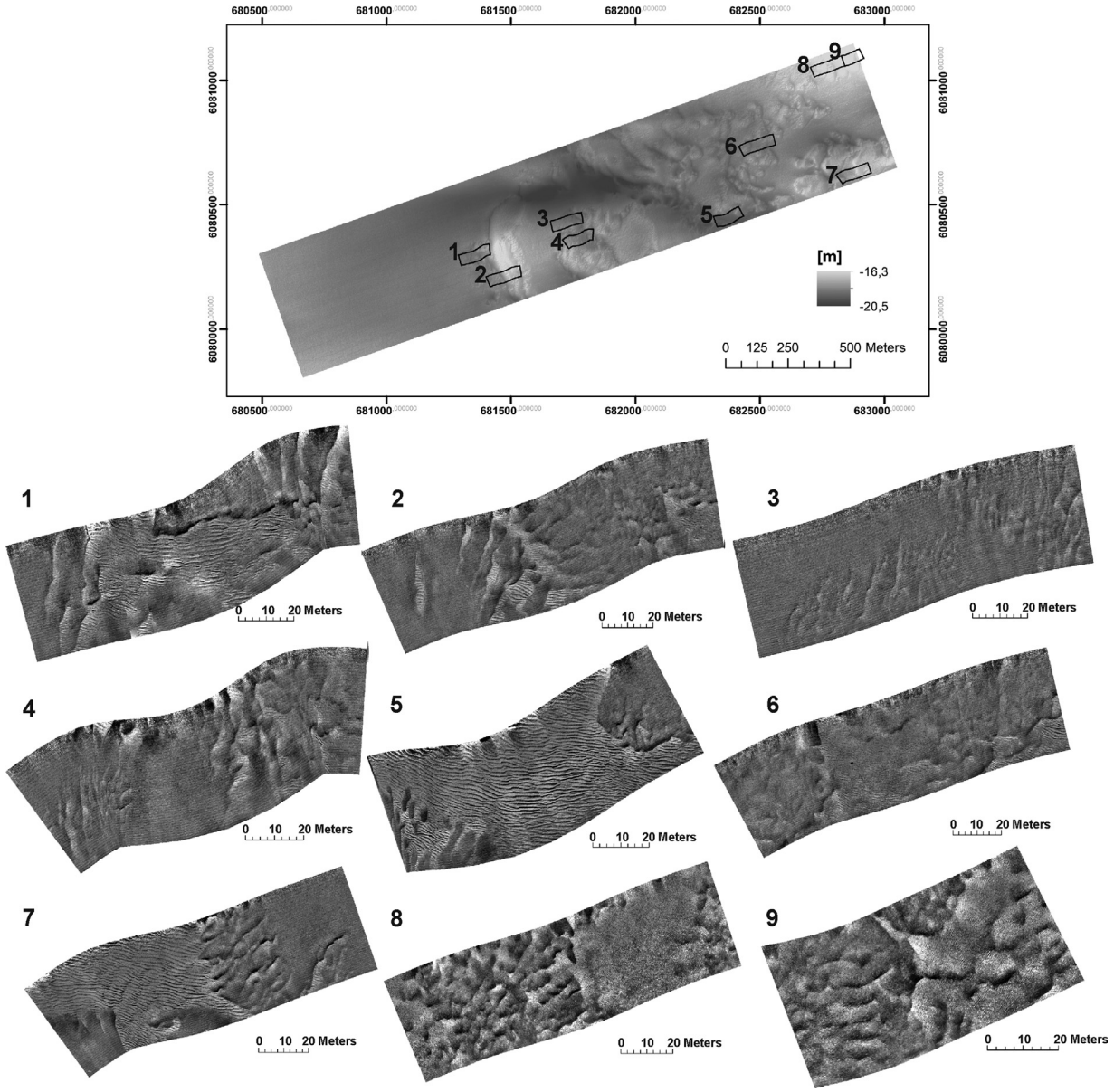

Figure 3 Images from a side-scan sonar survey, November 2017.

6. Discussion

The model of sediment transport and changes in seabed morphology aimed to determine the lengths (λ) and heights (η) of sand waves to be expected in the region analysed. The results show that sand waves formed by hydrodynamic conditions in this area should have a steepness of 0.01 to 0.02, a length of 47 m to 63 m, and a height of 0.6 m to 2.3 m. On the other hand, measured bed-form cross-sections (Figure 4) show bed forms with a length of 30 m to around 80 m and a height of around 0.4 m to 1.4 m. As it turns out, Yalin's model of sand wave height overestimates this parameter by about 100%. Predictions from Van Rijn's model are in the mean range of observed heights. The magnitude of length predicted by Hulscher's relation corresponds to the mean value of measured lengths, but this formula is sensitive to changes in storm event frequency and should be used with some caution. Figure 5 represents the sensitivity of this model. The $\Delta\lambda_{mean}$ represents the difference between sand wave lengths averaged over viscosity. Differences in the estimated sand wave length are largest for a frequency of 2—4 storms per year, where $\Delta\lambda_{mean}$ ranges from 11 to 42 m. For σ_{se} between 5 and 11 storms per year, differences in lengths are between 2 and 7 m. For frequencies of more than 12 storms per year, the $\Delta\lambda_{mean}$ is less than 2 m.

The relation established by Dalrymple et al. (1978) yields bed form height values close to the maximum observed in the cross-sections, which suggests that this equation could be used to estimate the highest possible sand waves.

The classification scheme recommended by the SEPM Bedforms and Bedding Structures Research Symposium (Gail, 1990) uses the height of bed forms calculated from their spacing (length) according to Flemming's formula. According to this approach, bed forms observed within the

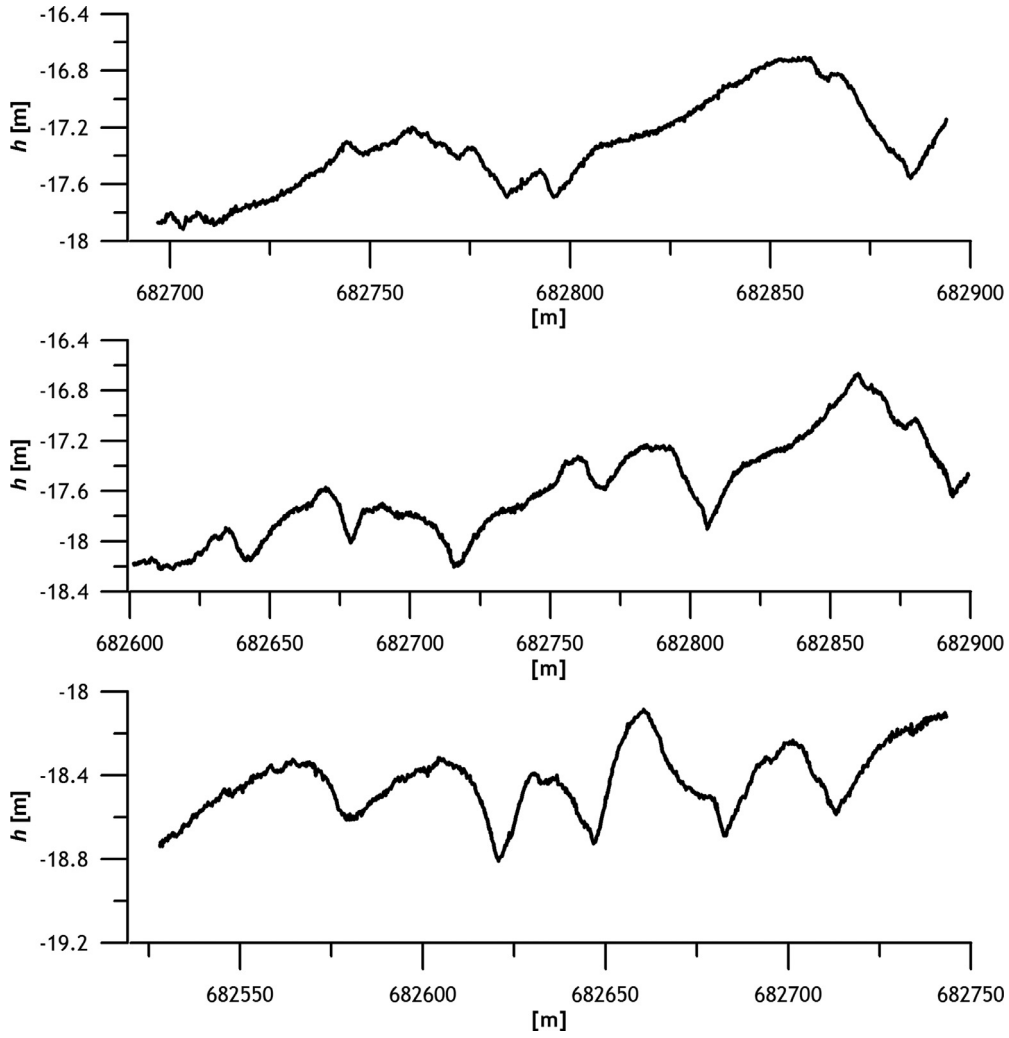

Figure 4 Cross-sections of bed forms observed within the study area.

Table 6 Sand wave height predicted on the basis of its relationship with sand wave length.

Year	Month	λ Sand wave length [m]	η Flemming's sand wave height [m]	η Dalrymple et al.'s sand wave height [m]
2017	10	53.48	1.69	1.17
2017	11	55.80	1.75	1.21
2017	12	59.41	1.84	1.27
2018	1	61.32	1.89	1.30
2018	2	62.25	1.91	1.31
2018	3	63.35	1.94	1.33
2018	4	59.41	1.84	1.27
2018	5	55.80	1.75	1.21
2018	6	52.17	1.66	1.15
2018	7	48.98	1.58	1.10
2018	8	47.18	1.53	1.07
2018	9	49.45	1.59	1.11
2018	10	51.50	1.64	1.14
Wave height calculated on the basis of observed wave length				
minimum		30	1.06	0.77
maximum		80	2.34	1.58

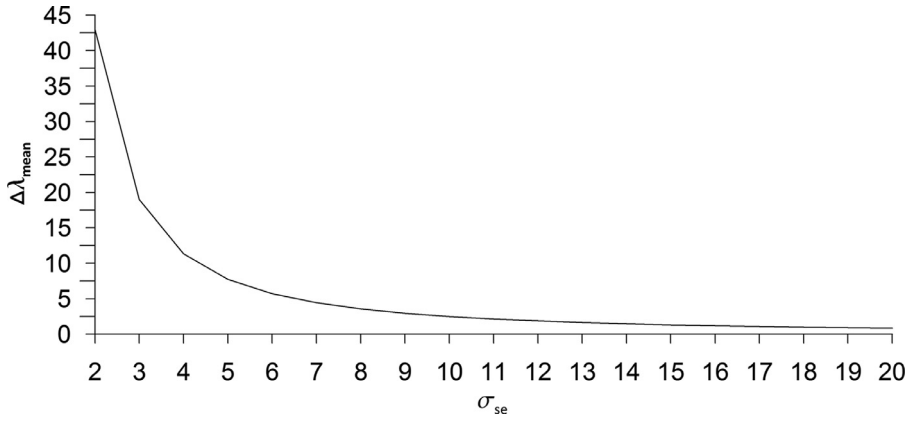

Figure 5 Dependence of average changes in wave length $\Delta\lambda_{mean}$ on the frequency of storms (σ_{se})

study area with a spacing of 30 m to 80 m have a height of 1.06 m to 2.34 m. On the other hand, according to the equation of Dalrymple et al. (1978) the height of these sand waves should range from 0.77 m to 1.58 m. The magnitudes of these dimensions put them in the category of large subaqueous sand waves. In fact, the observed height of some bed forms is rather smaller, which suggests classifying them in the group of medium subaqueous sand waves.

The proper topographical description of bed form patterns is very important, as it defines bottom roughness and thus regulates the shear stress over the flow. It is a very important parameter in many hydrodynamic and morphodynamic models.

Acknowledgements

The study was sponsored by the Ministry of Education and Science, Poland, under IBW PAN statutory programme No. 2 and national research project No. 2021/41/B/ST8/01943 which are hereby gratefully acknowledged.

Declaration of competing interest

The authors declare that they have no known competing financial interests or personal relationships that could have appeared to influence the work reported in this paper.

References

Aliotta, S., Perillo, G.M.E., 1987. A sandwave field in the entrance to Bahia Blanca estuary, Argentina. Mar. Geol. 76, 1—14. https://doi.org/10.1016/0025-3227(87)90013-2

Baas, J., Malarkey, J., Lichtman, I., Amoudry, L., Thorne, P., Hope, J., Peakall, J., Paterson, D., Bass, S., Cooke, R., Manning, A., Parsons, D., Ye, L., 2021. Current- and Wave-Generated Bedforms on Mixed Sand—Clay Intertidal Flats: A New Bedform Phase Diagram and Implications for Bed Roughness and Preservation Potential. Front. Earth Sci. 9. https://doi.org/10.3389/feart.2021.747567

Boothroyd, J.C., Hubbard, D.K., 1975. Genesis of bedforms in mesotidal estuaries. In: Cronin, L.E. (Ed.), Estuarine Research. Academic Press, Inc., New York, 217—234. https://doi.org/10.1016/B978-0-12-197502-9.50018-6

Cerkowniak, G.R., Ostrowski, R., Pruszak, Z., 2017. Application of Dean's curve to investigation of a long-term evolution of the southern Baltic multi-bar shore profile. Oceanologia 59 (1), 18—27. https://doi.org/10.1016/j.oceano.2016.06.001

Dalrymple, R.W., Rhodes, R.N., 1995. Chapter 13 Estuarine Dunes and Bars. In: Perillo, G.M.E. (Ed.), Geomorphology and Sedimentology of Estuaries. Elsevier Science, 359—422. https://doi.org/10.1016/S0070-4571(05)80033-0

Dalrymple, R.W., Knight, J.R., Lambiase, J.J., 1978. Bedforms and their hydraulic stability relationships in a tidal environment, Bay of Fundy, Canada. Nature 275, 100—104. https://doi.org/10.1038/275100a0

Flemming, B.W., 1988. Zur Klassifikation subaquatischer, stromungstrans ver saler Transportkorper. Boch. Geol. U. Geotech. Arb., v. 29, 44—47.

Gabel, S.L., 1993. Geometry and kinematics of dunes during steady and unsteady flows in the Calamus River, Nebraska, U.S.A. Sedimentology 40, 237—269. https://doi.org/10.1111/j.1365-3091.1993.tb01763.x

Gail, M.A., 1990. Classification of large-scale subaqueous bedforms: a new look at an old problem. In: Research symposium. Classification of subaqueous bed forms, 160—172. https://doi.org/10.2110/jsr.60.160

Hulscher, S.J., 1996. Tidal-induced large-scale regular bed form patterns in a three-dimensional shallow water model. J. Geophys. Res. 101 (C9), 20727—20744. https://doi.org/10.1029/96JC01662

Kubacka, M., Rudowski, S., Wróblewski, R., Szefler, K., Gajewski, Ł., 2016. Giant subaqueous dunes on a tideless sea bottom, rozewie bank, southern Baltic. In: Van Landeghem, K.J.J., Garlan, T., Baas, J.H. (Eds.), Fifth International Conference on Marine and River Dune Dynamics. Caernarfon, United Kingdom, 4—6 April 2016. Bangor Univ., SHOM, Madrid.

Lacy, J.R., Rubin, D.M., Ikeda, H., Mokudai, K., Hanes, D.M., 2007. Bed forms created by simulated waves and currents in a large flume. J. Geophys. Res. 112, C10018. https://doi.org/10.1029/2006JC003942

Li, M.Z., Amos, C.L., 1998. Predicting ripple geometry and bed roughness under combined waves and currents in a continental shelf environment. Cont. Shelf Res. 18, 941—970. https://doi.org/10.1016/S0278-4343(98)00034-X

Lu, Y.J., Li, S.Q., Zuo, L.Q., Liu, H.X., Roelvink, J.A., 2015. Advances in sediment transport under combined action of waves

and currents. Int. J. Sediment Res. 30 (4), 351—360. https://doi.org/10.1016/j.ijsrc.2015.01.003

Malarkey, J., Davies, A.G., 1998. Modelling wave—current interactions in rough turbulent bottom boundary layers. Ocean Eng. 25, 119—141. https://doi.org/10.1016/S0029-8018(96)00062-5

Mazumder, R., 2003. Sediment transport, aqueous bedform stability and morphodynamics under unidirectional current: a brief overview. J. Afr. Earth Sci. 36, 1—14. https://doi.org/10.1016/S0899-5362(03)00018-6

McCave, I.N., 1971. Sand waves in the North Sea off the coast of Holland. Mar. Geol. 10, 199—225. https://doi.org/10.1016/0025-3227(71)90063-6

Ostrowski, R., Stella, M., 2020. Potential dynamics of non-tidal sea bed in remote foreshore under waves and currents. Ocean Eng. 207. https://doi.org/10.1016/j.oceaneng.2020.107398

Ostrowski, R., Schonhofer, J., Szmytkiewicz, P., 2015. South Baltic representative coastal field surveys, including monitoring at the Coastal Research Station in Lubiatowo, Poland. J. Marine Syst. 162, 89—97. https://doi.org/10.1016/j.jmarsys.2015.10.006

Ostrowski, R., Stella, M., Szmytkiewicz, P., Kapiński, J., Marcinkowski, T., 2018. Coastal hydrodynamics beyond the surf zone of the South Baltic Sea. Oceanologia 60 (3), 264—276. https://doi.org/10.1016/j.oceano.2017.11.007

Pruszak, Z., Szmytkiewicz, P., Ostrowski, R., Skaja, M., Szmytkiewicz, M., 2008. Shallow-water wave energy dissipation in a multi-bar coastal zone. Oceanologia 50 (1), 43—58.

Rudowski, S., Łęczyński, L., Gajewski, Ł., 2008. Sand waves on the bottom of the deep nearshore and their role in shore formation. Landform Analysis 9, 214—216 (in Polish).

Southard, J.B., 1971. Representation of bed configurations in depth—velocity—size diagrams. J. Sediment. Petrol. 41 (4), 903—915. https://doi.org/10.1306/74D723B0-2B21-11D7-8648000102C1865D

Southard, J.B., Boguchwal, L.A., 1990. Bedform configurations in steady unidirectional water flows. Part 2: synthesis of flume data. J. Sediment. Petrol. 60 (5), 658—679. https://doi.org/10.1306/212F9241-2B24-11D7-8648000102C1865D

Stella, M., 2021. Morphodynamics of the south Baltic seabed in the remote nearshore zone in the light of field measurements. Mar. Geol. 439. https://doi.org/10.1016/j.margeo.2021.106546

Stella, M., Ostrowski, R., Szmytkiewicz, P., Kapiński, J., Marcinkowski, T., 2019. Driving forces of sandy sediment transport beyond the surf zone. Oceanologia 61 (1), 50—59. https://doi.org/10.1016/j.oceano.2018.06.003

Szmytkiewicz, P., Szmytkiewicz, M., Uścinowicz, G., 2021. Lithodynamic Processes along the Seashore in the Area of Planned Nuclear Power Plant Construction: A Case Study. on Lubiatowo at Poland. Energies 14 (6), 1636. https://doi.org/10.3390/en14061636

Uścinowicz, S., Jegliński, W., Miotk-Szpiganowicz, G., Nowak, J., Pączek, U., Przezdziecki, P., Szefler, K., Poręba, G., 2014. Impact of sand extraction from the bottom of the southern Baltic Sea on the relief and sediments of the seabed. Oceanologia 56 (4), 857—880. https://doi.org/10.5697/oc.56-4.857

Whitmeyer, S.J., Fitzgerald, D.M., 2008. Episodic dynamics of a sand wave field. Mar. Geol. 252, 24—37. https://doi.org/10.1016/j.margeo.2008.03.009

Van Rijn, L.C., 1984. Sediment transport, part III: bed forms and alluvial roughness. J. Hydraul. Eng. 110 (12), 1733—1754. https://doi.org/10.1061/(ASCE)0733-9429(1984)110:12(1733)

Yalin, S.M., 1964. Geometric properties of sandwaves. J. Hydraul. Div. 90 (HY5), 105—120. https://doi.org/10.1061/JYCEAJ.0001097

Zarillo, G.A., 1982. Stability of bedforms in a tidal environment. Mar. Geol. 48, 337—351. https://doi.org/10.1016/0025-3227(82)90103-7

Oceanologia 65 (2023) 494—502

Available online at www.sciencedirect.com

ScienceDirect

journal homepage: www.journals.elsevier.com/oceanologia

ORIGINAL RESEARCH ARTICLE

General characteristics of tidal currents in the entrance of Khor Abdullah, northwest of Arabian Gulf

Ali Abdulridha Lafta*

Marine Science Center, University of Basrah, Iraq

Received 19 November 2022; accepted 27 March 2023

KEYWORDS
Tidal currents;
Arabian Gulf;
Harmonic analysis;
Residual currents;
Khor Abdullah

Abstract The general characteristics of tidal currents in the entrance of the Khor Abdullah at Iraq marine water, located at the northwest tip of the Arabian Gulf, were studied based on realistic current measurements. The velocity measurements used in this study extended to about one year, which was never previously available in this vital region of the Arabian Gulf. The results illustrated that this area is characterized by strong currents exceeding 1 m/s during both ebb and flood tides, driven by local water level variations. The maximum currents recorded during the study period were 1.65 and 1.36 m/s at the ebb and flood tides, respectively. Additionally, the monthly averages of ebb currents are higher than those of flood currents. The harmonic analysis results revealed that the tidal effect explained approximately 98% of the variation in water currents, with the remaining percentage due to residual currents. Among the 35 tidal components used in harmonic analysis, the M_2 component was the main contributor to tidal currents variation in the area, followed by S_2, K_1, N_2, and O_1. The residual current seems to have a low effect on the currents variations in the area, with maximum values not exceeding 0.0677 and 0.058 m/s during the ebb and flood tides, respectively. The results obtained give a general view of the tidal current behavior and could be beneficial for several aspects of marine and coastal engineering as well as shipping and navigation activities in this region.

1. Introduction

The study of tidal hydrodynamics in coastal water is highly prioritized due to their direct impacts on overall maritime activities and ecosystems stability in these water systems. However, studying tidal hydrodynamics can be useful in understanding the transport and distribution of materials, construction of coastal infrastructure, and shipping processes in harbors and ports. Moreover, it can help determine the appropriate locations for wastewater effluent from industrial

* Corresponding author at: Marine Science Center, University of Basrah, Iraq.
E-mail address: ali.lafta@uobasrah.edu.iq
Peer review under the responsibility of the Institute of Oceanology of the Polish Academy of Sciences.

Production and hosting by Elsevier

https://doi.org/10.1016/j.oceano.2023.03.002

and domestic activities. Among the main oceanic currents, tidal currents play a fundamental role in physical processes in coastal regions. Tidal currents are generated and coincide with the rising and falling of the tide; the vertical motion of water causes the water to move horizontally, creating currents (Boon, 2013). Generally, tidal currents are responsible for water exchange processes between the coastal and open sea, consequently, they are the most essential mechanism responsible for the transport of material from or to the coastal systems (Kowalik et al., 2015; Sterl et al., 2020). However, tidal currents can break up pollutants or carry them farther toward the open sea. Moreover, tidal currents have the most significant effect on sediment transport in the coastal regions and, thus, on morphological changes by inducing erosion or sedimentation processes in these areas (Truong et al., 2021). Furthermore, understanding the tidal currents patterns could enhance navigation safety, particularly in the shallow coastal regions at the entrance of bays or estuarine systems.

Traditionally, there are two direct ways to measure tidal currents, the Lagrangian and the Eulerian methods (Poulain and Centurioni, 2015). Tidal currents measurements by the Lagrangian method are conducted simply by adding something to the water and following it as it moves. Meanwhile, the Eulerian approach involves placing an instrument in a fixed position and measuring how fast the water flow at that location. The most valuable data on tidal currents, particularly for long periods of observations, could be obtained by installing special instruments anchored to the seafloor (moorings) or mounted on buoys and platforms. Nowadays, the ADCP (acoustic Doppler current profiler) technique is widely used around the world to measure the flow velocity in both coastal and open seas due to their flexibility and accuracy in conducting such measurements (Bi et al., 2019; Hoitink et al., 2009; Shin et al., 2022).

Iraq marine water, located at the northwest tip of the Arabian Gulf, is the most estuarine part of the gulf, consisting of the Shatt al-Arab estuary and several open lagoons, such as Khor Al-Kafka, Khor Al-Amaya, and Khor Abdullah (Al-Mahdi et al., 2009). Iraq's marine water is critical to the country because it is the only way to reach the open sea (Lafta et al., 2020). The Arabian Gulf is the world's most important oil transport waterway, and it receives a great deal of attention from researchers in various scientific fields, particularly oceanographic studies (Alosairi et al., 2011; Alothman and Ayhan, 2010; Kämpf and Sadrinasab, 2006; Lafta, 2021; Madah and Sameer, 2022; Ranjbar et al., 2020; Reynolds, 1993; Sadrinasab and Kämpf, 2004; Siddig et al., 2019). However, physical oceanographic studies at the gulf's northwestern tip, particularly those based on field measurements, remain incomplete and require further investigation. However, Arabian Gulf is familiar with strong tidal currents, which coincide with a high tidal range that exceeds 1 m in all gulf regions (Alosairi et al., 2011; Reynolds, 1993). Najafi (1997) predicted that the tidal currents can reach 0.9 m/s in the gulf head and range between 0.3 and 0.6 m/s elsewhere. However, the measurements of tidal currents in Iraq marine water are very scarce, and if available, they are limited to short periods. Al-Mahdi et al. (2009) conducted one of the first studies that highlighted the physical characteristics of Iraq's marine water. They indicated that the tidal currents in the entrance of Khor Abdullah are strong and reach speeds of the order of 1—2 m/s. Al-Mahdi and Mahmood (2010) studied the features of tidal currents at the entrance of Khor Abdullah and indicated that the mean flood currents are higher than the mean ebb currents. Moreover, they showed a reduction in the speed of currents with the depth. Moreover, Al-Hasem (2018) was the first to study the tidal currents characteristics based on a continuous measurement of flow velocities near our study area. However, he studied the behavior of tidal currents using hourly records of flow velocities for about 54 days near the entrance of Khor Abdullah on the Kuwait coast. He showed that the maximum flood and ebb velocities reach 1.07 and 1.08 m/s, respectively. This study aims to examine the general characteristics of the tidal currents at the entrance of Khor Abdullah in Iraq marine water located at the northwestern tip of the Arabian Gulf based on a relatively long record of the velocity of the currents.

2. Material and methods

2.1. Study area

Iraq marine water is located at the northwest tip of the Arabian Gulf. The area is known as a waterway of oil transportation and oil industries for mega oil fields in southern Iraq, as well as its economic importance for the country due to the shipping processes by several commercial ports. Figure 1 shows the location of the study area and the ADCP and tide gauge sites. However, the study area is located in the most shallow water region of the gulf, with depths ranging from 10 to 20 m.

The tidal regime in the region is mixed, primarily semidiurnal, with the essential tidal constituents being the semidiurnal M_2 and S_2 and diurnal K_1 and O_1 (Lafta et al., 2020; Lafta, 2022).

The climate of this region is characterized by an arid desert climate with two distinct seasons: a hot and long summer of about 230 days and cold and rainy winter (Zakaria et al., 2013). Rainfall occurs during the winter months, and its average is generally low, with a negligible contribution to the water budget in Arabian Gulf (Reynolds, 1993). The prevailing wind regime in the northwest of the Arabian Gulf is the northwest wind, locally known as the Shamal wind. This wind blows on the area during most months of the year with notable seasonal variations. The second important wind regime in the region is the southeast wind; its period ranges from hours to several days (Reynolds, 1993). The averages of wind speed are higher in summer than those in winter. The peak wind speeds are generally due to the northwest wind and the maximum wind speed can exceed 20 m/s. On the other hand, although the southeast wind speed is generally lower than that of the northwest wind, the highest wave heights in the studied area were recorded during the southeast wind, which is mainly attributed to a large fetch available for the southeast wind relative to a limited fetch available to the northwest wind (Lafta and Al-Fartusi, 2022). The wind waves are dominant in the area with negligible contribution due to swell waves. The highest observed significant and maximum wave heights reach 0.78 and 1.95 m, respectively (Lafta and Al-Fartusi, 2022).

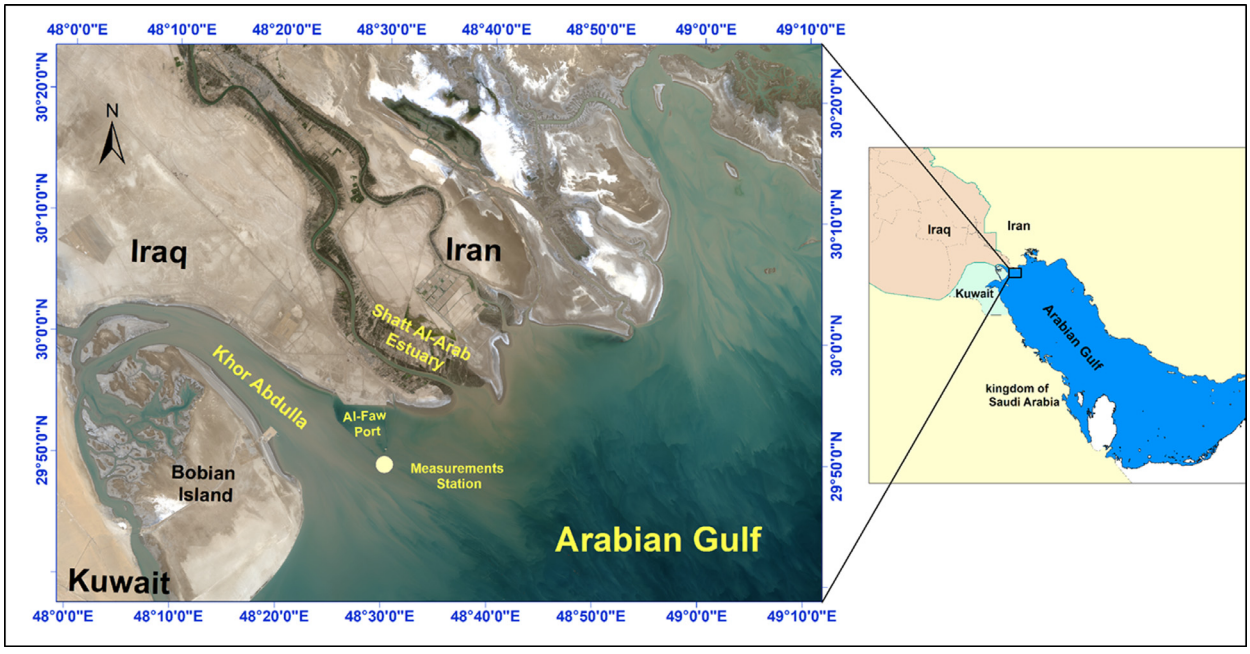

Figure 1 Location map of the study area showing the measurements station (Lafta, 2021).

2.2. Harmonic analysis of currents

The harmonic tidal current analysis is widely used to obtain the amplitudes and phase lags for each tidal frequency (Chen et al., 2021; Jin et al., 2018; Khedr et al., 2018). The traditional harmonic tidal model involving tidal and nontidal energies can be expressed as follows:

$$h(x,t) = h_0 + \sum_{j=1}^{m} f_j H_j \cos\left(\omega_j t + u_j - k_j^*\right) + R, \quad (1)$$

where t is time in hours, h(x,t) is the water level or water current at time t, f_j is the lunar node factor for constituent, H_j is the amplitude for constituent, h_0 is the mean water level or water current in that location, u_j is the nodal phase for constituent, k_j^* is the phase of constituent, ω_j is the frequency of constituent, m is the number of constituents, and R is the nontidal residual. For purely solar constituents, $f_j = 1$ and $u_j = 0$. The residual currents, which are generated by forces other than astronomical tidal forces, play an important role in coastal hydrodynamics (Antoranz et al., 2001). Residual currents control the transport of sediment and consequently largely contribute to long-term morphological changes in coastal regions. Additionally, residual currents control the transport and fate of pollution, which has a considerable effect on the environmental stability of coastal water.

The MATLAB World tide and World Currents, a package for tide and tidal current analysis was used in this study (Boon, 2013). The World Currents package analyzes water currents based on the assumption that horizontal currents can be converted into two components, U and V. However, in the entrances of estuaries and lagoons, the currents display reverse directions associated with flood and ebb phases of the tidal cycle. Hence, by separating currents into two components, obviously, there will be the principal axis U and secondary axes V. The idea proposed by World Currents package is that if there is a distinguished direction of flood and ebb currents, then the orthogonal axes (U, V) can rotate to correspond to the water current directions while keeping the dots (data of water velocities) fixed. The principal and secondary axes resulting from the rotation of U and V are denoted as U_p and V_p. The total variance, the combined variance for U_p and V_p, will be the same as that for U and V. However, the principle axis U_p will have the greatest fraction possible of the total variance and V_p will have the least. If the U_p fraction is high enough, we may choose it and ignore V_p altogether, reducing the current's dimensionality from two to one (Boon, 2013). The U_p current component is one needed for the tidal current analysis, and we can now analyze a current curve plotted as a continuous function of time.

2.3. Data source

Generally, water currents measurements in Iraq marine water are very scarce, and when available, they are generally limited for a short period that does not exceed one tidal cycle. In the past decade, Daewoo Engineering and Construction Co., Ltd., which constructed the western breakwater of the Grand Faw Port, installed a hydrographic station at the entrance of Khor Abdullah, about 700 m far from the breakwater at 29°50′1.8″N, 48°28′43.8″E (Figure 1). The water depth at this location reaches 10 m. Several oceanographic and meteorological elements are recorded continuously by this platform. These data are managed under the responsibility of the General Acoustics company, Germany (https://www.generalacoustics.com/).

The continuous records of the water currents for January 2018 to November 2018 and the water level of 2018 were acquired by the General Company for Ports of Iraq. The water level measurements are carried out by installing an acoustic tide gauge above the platform at a height of 4.98 m relative

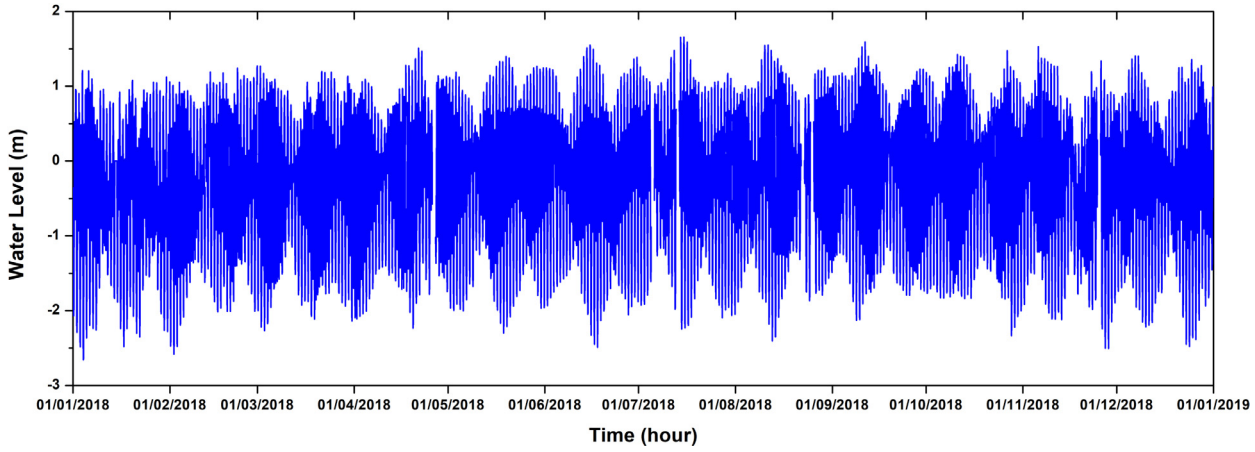

Figure 2 Time series of the hourly water level during 2018 at the entrance of Khor Abdullah.

to the mean sea level. All water level measurements are rectified to the local vertical datum known as Faw 1979 datum, the local datum in this region. The interval in water level records was one hour for the entire year of 2018.

The currents (speed and direction) measurements are carried out using a moored ADCP. The ADCP measured the water currents profile with 0.5 m space step along the water column, with a time interval of 10 minutes. However, due to the shallow nature of the study area (depth of 10 m), no remarkable changes in the water currents patterns along the water column were observed; hence, only the near-surface velocity measurements will be analyzed and discussed.

3. Results and discussion

3.1. Water level variability

Water level records in the studied area showed remarkable variations ranging from hourly to annual fluctuations. The sea-level records showed a maximum annual tidal range of about 4.32 m, from 1.66 to −2.66 m (Figure 2). This tidal range is the highest range recorded in the entire Arabian Gulf water. A similar range is observed in Kuwait bay, a semi-enclosed bay near the studied area, as indicated by Alosairi et al., 2018. Generally, the maximum tidal ranges are recorded during the spring tide, while during the neap tide, the tidal range rarely exceeds 2.5 m (Figure 2).

Table 1 displays the maximum and minimum water height during the months of 2018. The table shows that the water level reaches its highest values during the summer months, i.e., June to September. However, this behavior has been observed previously in several areas in the Arabian Gulf. It is generally attributed to the impact of the meteorological forces, particularly the atmospheric pressure, which reaches its lowest levels during the summer months (Afshar-Kaveh et al., 2020; Sultan et al., 2000). In contrast, during the winter, when the atmospheric pressure is at its highest levels, and due to the inverse relationship between this meteorological element and the sea surface, the water height is generally at the lowest level, as shown in Figure 2.

The water level variations in the study area are mainly associated with the astronomical tidal phenomenon. The harmonic analysis results of the water level in the northwest tip of the Arabian Gulf demonstrated that the astronomical tide is responsible for about 90% to 96% of water level variation (Alosairi et al., 2018; Lafta, 2021). Meanwhile, the rest of the water level variations are known as the residual water level, mainly attributed to other factors, particularly atmospherical forces. Consequently, water circulation in these regions is generally governed by tidal effects.

Table 1 Statistics of water level in the Enterence of Khor Abdullah in 2018.

Month	Minimum	Maximum
January	−2.66	1.20
February	−2.58	1.27
March	−2.27	1.26
April	−2.23	1.51
May	−2.30	1.48
June	−2.49	1.55
July	−2.24	1.66
August	−2.40	1.55
September	−2.12	1.59
October	−2.33	1.47
November	−2.50	1.53
December	−2.47	1.40

3.2. Current variability from moored measurements

The time series of near-surface currents' velocities are presented in Figure 3. However, the most common maxima exceeded 1 m/s during both the ebb and flood phases of the tidal cycle. The results illustrated that the maximum tidal current velocity generally occurs during the ebb tide. The highest flow of currents recorded during the study period reaches 1.65 m/s during the ebb tide. The monthly averages of tidal current velocities showed that the average monthly ebb velocities were also greater than the average monthly flood velocities. However, the monthly averaged flood velocities ranged between 0.56 and 0.62 m/s, while

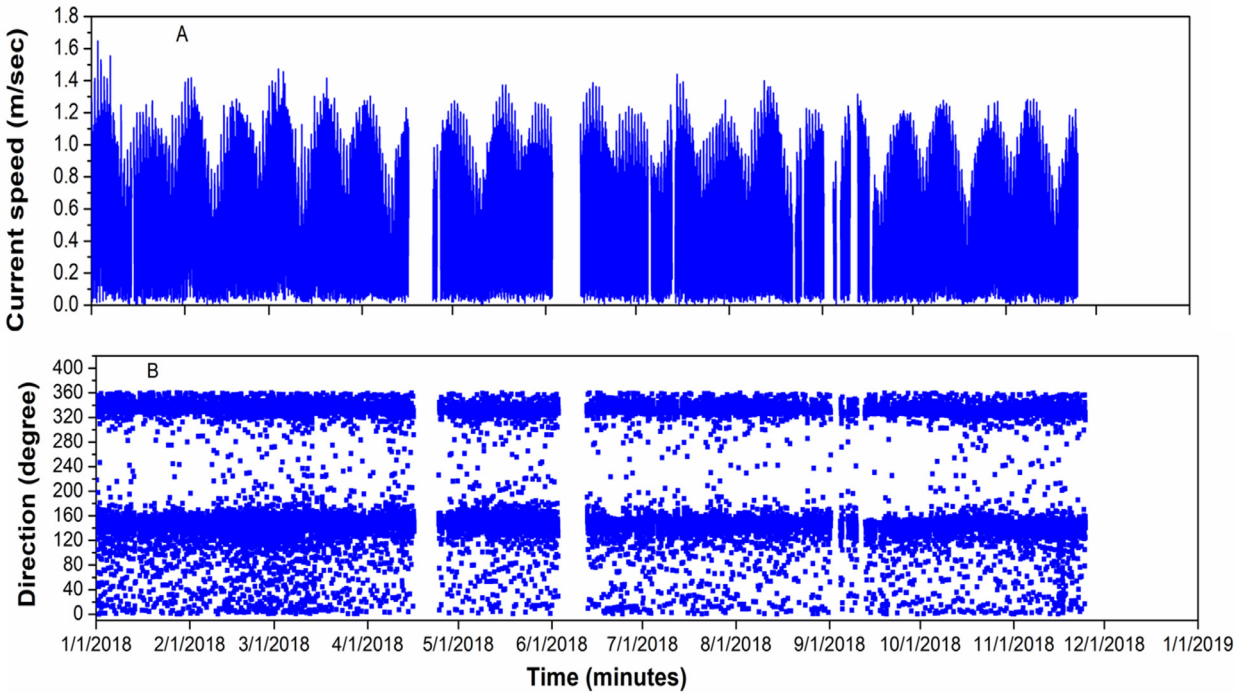

Figure 3 Time series of the currents speed (A) and direction (B) during 2018 at the entrance of Khor Abdullah.

Table 2 The ebb and flood currents statistical characteristics.

Month	Flood		Ebb	
	Mean	Maximum	Mean	Maximum
Jan.	0.62	1.27	0.69	1.65
Feb.	0.59	1.28	0.70	1.42
Mar.	0.59	1.24	0.72	1.47
Apr.	0.57	1.23	0.67	1.30
May	0.58	1.22	0.68	1.37
Jun.	0.61	1.21	0.71	1.39
Jul.	0.56	1.23	0.65	1.44
Aug.	0.58	1.36	0.68	1.40
Sep.	0.58	1.24	0.66	1.31
Oct.	0.59	1.24	0.65	1.28
Nov.	0.56	1.20	0.62	1.28

the monthly averaged ebb velocities ranged between 0.62 and 0.72 m/s (Table 2).

Based on the orientation of the study area, tidal currents have two distinguished directions, southeast during ebb tide and northwest to west-northwest through the flood tide. Other directions for the tidal current were found, but they were all very weak velocities and generally occurred during the transition period from flood tide to ebb tide and vice versa (Figure 4), and similar results were observed by Al-Hasem (2018).

Figure 5 illustrates the percentage of occurrence of various current velocity classes. The figure also shows that the flood is slightly higher for lower velocity classes, i.e., less than 0.6 m/s; meanwhile, the ebb exceeds the flood for higher velocity classes. The distribution of ebb currents demonstrated that the most frequent class of velocities is the 0.8—1 m/s group with a frequency exceeding 20%. The second significant class of ebb velocities was the 0.6—0.8 m/s group, with a frequency reaching 19.5%, followed by the class 0.4—0.6 m/s group, with a frequency of 16%. The velocity classes of 0.2—0.4 and 1—1.2 m/s seem to have an equal frequency of occurrence at about 15%. Additionally, the highest velocities of tidal currents are more frequent during the ebb phase of the tidal cycle, particularly velocities that are higher than 1.2 m/s, compared to flood currents that seem to rarely exceed 1.3 m/sec. Correspondingly, the most frequent velocity class for the flood current is the 0.8—1 m/s group, followed by 0.6—0.8 m/s and 0.4—0.6 m/s, respectively.

3.3. Harmonic analysis of currents

The characteristics of the tidal currents are investigated using the harmonic model for currents velocity recorded in the study station (Figure 1), which was performed by the World Currents package, a MATLAB application for the harmonic analysis and prediction of tides and currents (Boon, 2013). The U and V current plot in Figure 6 shows how the Khor Abdullah entrance data are distributed. Each red dot in the diagram represents the tip of a current vector with speed and direction from the origin plotted on a grid with orthogonal U and V axes. By the rotation of the U and V to the orthogonal axes U_p and V_p, the origin is first shifted to the bivariate mean position, and both axes are then rotated 59° clockwise about this point. Thus, a point lying on the U axis would have a current heading of 90°, while a point on the Up axis would have a heading of 149°.

However, Figure 6 shows that the data are arrayed from one end of the U_p axis to the other, and hence, the current

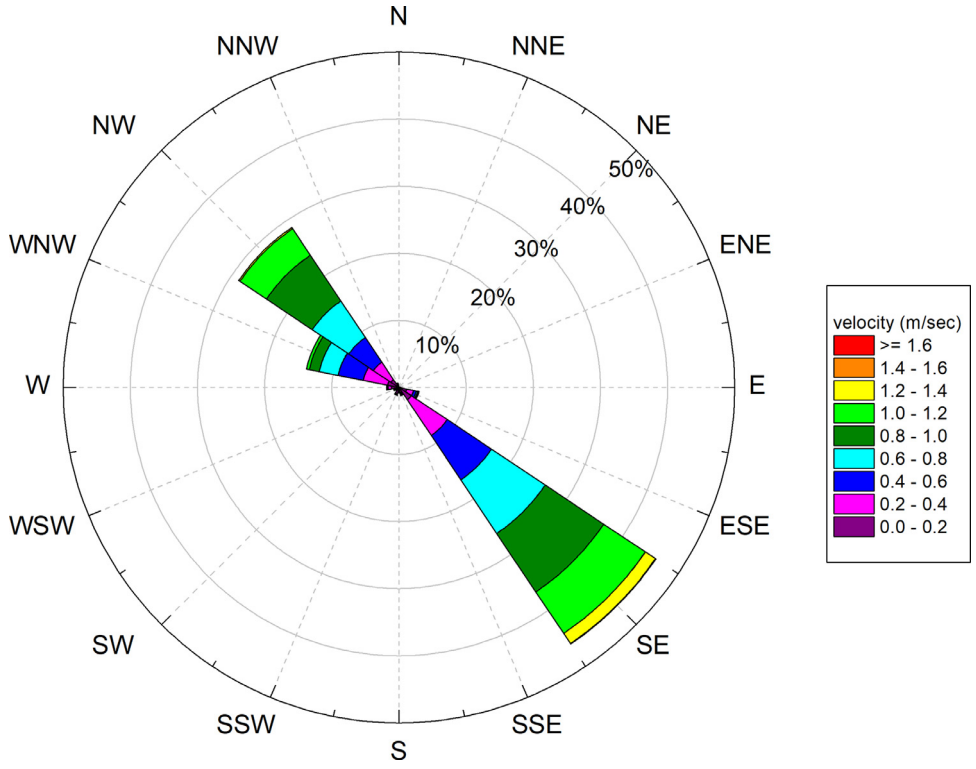

Figure 4 The rose diagram of currents at the entrance of Khor Abdullah during 2018. Up axis would have a heading of 149°.

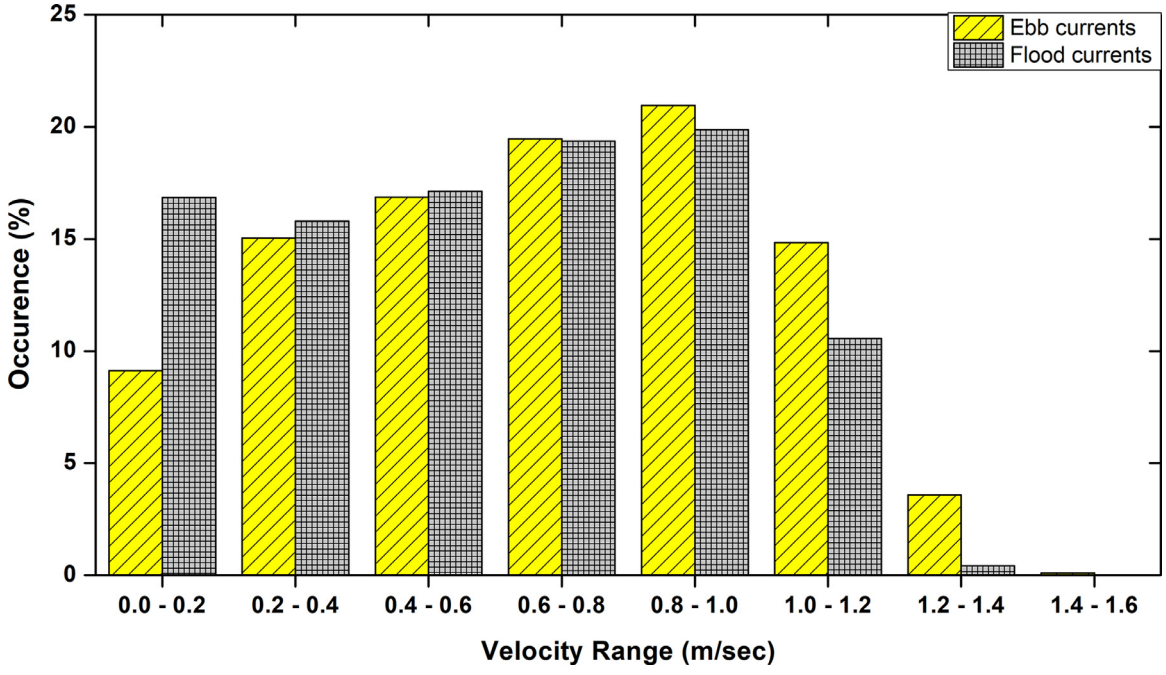

Figure 5 Percentage of various velocity classes for flood and ebb currents in Khor Abdullah Entrance.

readings projected onto this axis show an obvious spread. The U_p axis (329°—149° with respect to true north) shows the greatest spread, the maximum variance possible for any axis orientation; therefore, U_p becomes the principal axis. Meanwhile, V_p clearly has the least spread in projected values and becomes the minor axis. Moreover, the Principal Axis Variance (PAV) in Figure 6 is 0.994. The small remaining fraction of variance associated with the minor axis (0.006) suggests that not much will be missed if V_p is ignored and only U_p is considered. Thus, the currents analysis is conducted for the principle axis U_p. The harmonic analysis results of a tidal stream (Table 3) showed that the 35 astronomical constituents used by the World Currents package can explain about 98% of the total variance of the current

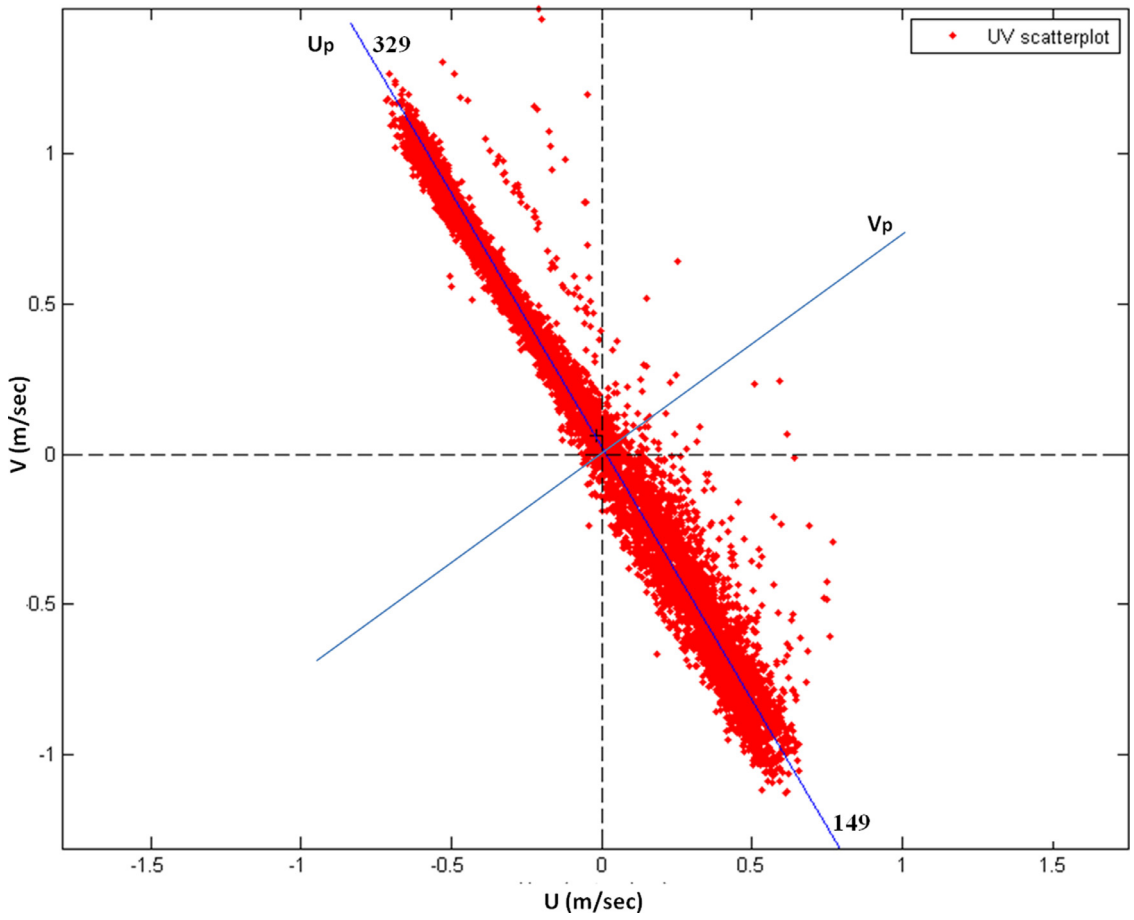

Figure 6 U,V plot of surface current readings at Khor Abdullah entrance, 2018. Principal Axis Variance (PAV) is 0.994. The flood direction is 329°; the ebb direction is 149°.

Table 3 Amplitudes (m/s) and phases (degree) for the constituents that are used in the harmonic analysis of currents in the Khor Abdullah Entrance.

Constituent	Amplitude	Phase	Constituent	Amplitude	Phase	Constituent	Amplitude	Phase
Q1	0.016	201.13	N2	0.143	263.05	MK3	0.036	275.77
RHO1	0.001	295.87	NU2	0.041	7.99	MN4	0.017	44.62
O1	0.104	305.87	M2	0.742	16.29	M4	0.047	156.99
M1	0.004	28.83	LAM2	0.027	173.17	MS4	0.036	284.15
P1	0.052	41.61	L2	0.043	25.43	S4	0.004	93.09
S1	0.009	334.91	T2	0.016	133.18	2MN6	0.012	184.26
K1	0.178	30.3	S2	0.251	138.92	M6	0.019	300.28
J1	0.01	176.14	R2	0.002	176.39	2MS6	0.022	56.44
OO1	0.006	0.23	K2	0.08	287.1	S6	0.001	67.46
MNS2	0.011	278.77	2SM2	0.018	44.33	M8	0.005	63.67
2N2	0.022	137.28	2MK3	0.048	169.95	3MS8	0.007	176.8
MU2	0.048	45.73	M3	0.004	29.16			

in the studied area during the study period. The main constituents (K_1, O_1, M_2, S_2, N_2) contributed to about 70% of this variation. The principle semidiurnal lunar constituent M_2 was the main contributor to the total variation of tidal current by about 36%, followed by S_2, K_1, N_2, and O_1. Additionally, the diurnal constituent P_1 seems to have an essential contribution to tidal currents variability in the studied area, which is in line with the findings of Pous et al. (2012), who pointed out that this constituent has an important contribution to tidal hydrodynamics of the Arabian Gulf. Correspondingly, most of the shallow water constituents seem to significantly contribute to tidal currents variation, par-

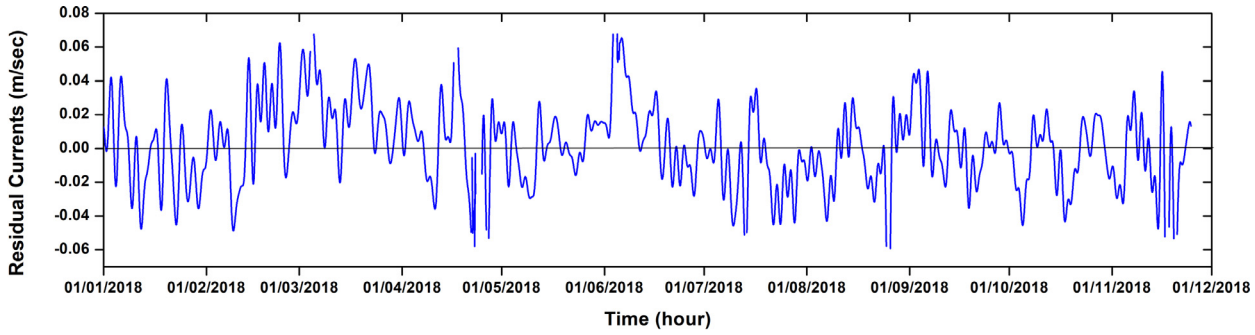

Figure 7 Residual currents in the Khor Abdullah entrance (positive values refer to the currents towards the southeast while negative values refer to the northwest direction).

ticularly $2MK_3$, M_3, MK_3, MN_4, M_4, and MS_4. However, this is not a surprising result since the studied area is a shallow coastal region with a maximum depth not exceeding 20 m (Lafta, 2021).

The form number $((O_1 + K_1)/(M_2 + S_2))$ was 0.28. Based on the classification of (Defant, 1961), the study area displays a mixed, predominantly semidiurnal tide, which is in line with the previous finding of Alosairi et al. (2018) and Lafta et al. (2020).

3.4. Residual currents

The residual currents in the studied area were obtained by applying a low-pass filter to the resulting hourly residual curve from harmonic analysis to remove all signals in semidiurnal and diurnal tidal frequencies. The cutoff frequency was 57×10^{-7} Hz (equivalent to 0.5 cycles per day). The residual currents show a seasonal fluctuation with a maximum ebb value reaching 0.0677 m/s during June and a minimum value of 0.023 m/s during October. Meanwhile, the maximum flood value of 0.058 m/s during April and a minimum of 0.02943 m/s during May (Figure 7). The direction of the residual currents shows a monthly variation. It fluctuates between northwest during five months of the study interval, i.e., January, July, August, October, and November, and southeast direction during the rest months. These fluctuations in residual direction could be attributed to the dominant wind regime in the study area, which has been well documented as ranging from northwest to southeast winds (Al Senafi and Anis, 2015; Lafta and Al-Fartusi, 2022). However, when the monthly average residual current is compared to the monthly average of the along-wind component, there appears to be no obvious relationship between them, with a correlation coefficient of less than 0.2. Hence, the origin of residual currents could belong to other forces rather than the wind force. The most probable driver could be the rivers flow since the area is known as the most estuarine part in the northwest of the Arabian Gulf. The southeast direction of residual current seems to correlate well with the river discharge during the wet months, which occur through the spring and winter months. Unfortunately, no data on river discharge is available during the study period. So, when such data is available, one can examine this hypothesis and obtain a deep understanding of the behavior of residual currents in this region.

4. Conclusion

In this study, the general behavior of tidal currents was highlighted at the entrance of Khor Abdullah in Iraq marine water at the northern tip of the Arabian Gulf. The study is based on the realistic measurements of water currents and for a relatively long period, which was never conducted previously in this region. The results illustrated that the studied area is characterized by strong tidal currents that exceed 1 m/s during both the ebb and flood phases of the tidal cycle. Additionally, the results show that the ebb velocities were generally higher than the flood velocities. The distribution of ebb and flood currents demonstrated that the most frequent class of velocities is the 0.8—1 m/s group. The results showed that the strong currents, i.e., with velocities greater than 1.5 m/s, seldom occur during flood tide and mostly occur during the ebb tide.

The harmonic analysis result demonstrated that about 98% of water currents variation was explained using 35 tidal constituents, with the remaining percentage explained using residual currents. The astronomical constituent M_2 was the main contributor to the total variation of tidal current, followed by S_2, K_1, N_2, and O_1. These five constituents account for approximately 70% of the total variance of currents in the studied area, with the remaining 30% due to the other 30 constituents. It should be noted that these findings were the primary findings and focused on the general behavior of tidal currents in this important region of the northwestern Arabian Gulf.

Acknowledgements

The author is grateful to General Company of Iraq Ports and General Acoustics company, Germany, especially Eng. Jörg Stuczynski for providing the data.

References

Afshar-Kaveh, N., Nazarali, M., Pattiaratchi, C., 2020. Relationship between the Persian Gulf sea-level fluctuations and meteorological forcing. J. Mar. Sci. Eng. 8, 285. https://doi.org/10.3390/jmse8040285

Al Senafi, F., Anis, A., 2015. Shamals and climate variability in the northern Arabian/Persian Gulf from 1973 to 2012. Int. J. Climatol. 35, 4509—4528. https://doi.org/10.1002/joc.4302

Al-hasem, A.M., 2018. Tidal Current Behaviors and Remarkable Bathymetric Change in the South-Western Part of Khor Abdullah. Kuwait. Int. J. Mar. Env. Sci. 12 (2), 118—125.

Al-Mahdi, A.A., Abdullahh, S.S., Husain, N.A., 2009. Some Features of the Physical Oceanography in Iraqi Marine Water. Mesopot. J. Mar. Sci. 24, 13—24.

Al-Mahdi, A.A., Mahmood, A.B., 2010. Some Features of Tidal Currents in Khor Abdullah. North West Arabian Gulf. J. KAU: Mar. Sci. 21 (1), 162—182.

Alosairi, Y., Imberger, J., Falconer, R.A., 2011. Mixing and flushing in the Persian Gulf (Arabian Gulf). J. Geophys. Res. 116, C03029. https://doi.org/10.1029/2010JC006769

Alosairi, Y., Pokavanich, T., Alsulaiman, N., 2018. Three-dimensional hydrodynamic modeling study of reverse estuarine circulation: Kuwait Bay. Mar. Pollut. Bull. 127, 82—96. https://doi.org/10.1016/j.marpolbul.2017.11.049

Alothman, A., Ayhan, M., 2010. Detection of Sea Level Rise within the Arabian Gulf Using Space Based GNSS Measurements and In situ Tide Gauge data. 38th COSPAR Scientific Assembly 38, 3—7.

Antoranz, A.M., Pelegri, J.L., Masciángoli, P., 2001. Tidal currents and mixing in the Lake Maracaibo estuarine system. Sci. Mar. 65 (Suppl. 1), 155—166. https://doi.org/10.3989/scimar.2001.65s1155

Bi, C., Bao, X., Ding, Y., 2019. Observed characteristics of tidal currents and mean flow in the northern Yellow Sea. J. Ocean. Limnol. 37, 461—473. https://doi.org/10.1007/s00343-019-8026-z

Boon, J.D., 2013. Secrets of the Tide: Tide and Tidal Current Analysis and Predictions, Storm Surges and Sea Level Trends. Elsevier, 224 pp.

Chen, Y.R., Paduan, J.D., Cook, M.S., Chuang, L.Z., Chung, Y.J., 2021. Observations of Surface Currents and Tidal Variability Off of Northeastern Taiwan from Shore-Based High Frequency Radar. Remote Sens. 13, 3438. https://doi.org/10.3390/rs13173438

Defant, A., 1961. Physical Oceanography, vol. 1. Pergamon Press, London, 729 pp.

Hoitink, A.J.F., Buschman, F.A., Vermeulen, B., 2009. Continuous measurements of discharge from a horizontal acoustic Doppler current profiler in a tidal river. Water Resour. Res. 45 (11), 1—3. https://doi.org/10.1029/2009WR007791

Jin, G., Pan, H., Zhang, Q., Lv, X., Zhao, W., Gao, Y., 2018. Determination of harmonic parameters with temporal variations: An enhanced harmonic analysis algorithm and application to internal tidal currents in the south China Sea. J. Atmos. Ocean. Tech. 35 (7), 1375—1398. https://doi.org/10.1175/jtech-d-16-0239.1

Kämpf, J., Sadrinasab, M., 2006. The circulation of the Persian Gulf: A numerical study. Ocean Sci. 2, 27—41. https://doi.org/10.5194/os-2-27-2006

Khedr, A.M., Abdelrahman, S.M., Alam El-Din, K.A., 2018. Currents and sea level variability of Alexandria Coast in Association with Wind Forcing. J. KAU: Mar. Sci. 28, 27—42. https://doi.org/10.4197/Mar.28-2.3

Kowalik, Z., Marchenko, A., Brazhnikov, D., Marchenko, N., 2015. Tidal currents in the western Svalbard Fjords. Oceanologia 57 (4), 318—332. https://doi.org/10.1016/j.oceano.2015.06.003

Lafta, A.A., 2021. Influence of atmospheric forces on sea surface fluctuations in Iraq marine water, northwest of Arabian Gulf. Arab. J. Geosci. 14, 1639. https://doi.org/10.1007/s12517-021-07874-x

Lafta, A.A., 2022. Investigation of tidal asymmetry in the Shatt Al-Arab river estuary, Northwest of Arabian Gulf. Oceanologia 64 (2), 376—386. https://doi.org/10.1016/j.oceano.2022.01.005

Lafta, A.A., Al-Fartusi, A.J., 2022. General characteristics of surface waves in Iraq marine water, Northwest of Arabian Gulf. Arab. J. Geosci. 15, 1598. https://doi.org/10.1007/s12517-022-10884-y

Lafta, A.A., Altaei, S.A., Al-Hashimi, N.H., 2020. Impacts of potential sea-level rise on tidal dynamics in Khor Abdullah and Khor Al-Zubair, northwest of Arabian Gulf. Earth Syst. Environ. 4, 93—105. https://doi.org/10.1007/s41748-020-00147-9

Madah, F., Sameer, G., 2022. Numerical Simulation of Tidal Hydrodynamics in the Arabian Gulf. Oceanologia 64 (2), 327—345. https://doi.org/10.1016/j.oceano.2022.01.002

Najafi, H.S., 1997. Modeling tides in the Persian Gulf using dynamic nesting. Ph.D. thesis, Univ. Adelaide, South Australia.

Poulain, P.M., Centurioni, L., 2015. Direct measurements of World Ocean tidal currents with surface drifters. J. Geophys. Res.-Oceans 120 (10), 6986—7003. https://doi.org/10.1002/2015JC010818

Pous, S., Carton, X., Lazure, P., 2012. A Process Study of the Tidal Circulation in the Persian Gulf. Open J. Mar. Sci. 02 (04), 131—140. https://doi.org/10.4236/ojms.2012.24016

Ranjbar, M.H., Etemad-Shahidi, A., Kamranzad, B., 2020. Modeling the combined impact of climate change and sea-level rise on general circulation and residence time in a semi-enclosed sea. Sci. Total Environ. 740, 140073. https://doi.org/10.1016/j.scitotenv.2020.140073

Reynolds, R.M., 1993. Physical oceanography of the Gulf, Strait of Hormuz, and the Gulf of Oman: results from the Mt Mitchell expedition. Mar. Pollut. Bull. 27, 35—59. https://doi.org/10.1016/0025-326X(93)90007-7

Sadrinasab, M., Kämpf, J., 2004. Three-dimensional flushing times of the Persian Gulf. Geophys. Res. Lett. 31, 1—4. https://doi.org/10.1029/2004GL020425

Shin, H.R., Lee, J.H., Kim, C.H., Yoon, J.H., Hirose, N., Takikawa, T., Cho, K., 2022. Long-term variation in volume transport of the Tsushima warm current estimated from ADCP current measurement and sea level differences in the Korea/Tsushima Strait. J. Marine Syst. 232. https://doi.org/10.1016/j.jmarsys.2022.103750

Siddig, N.A., Al-Subhi, A.M., Alsaafani, M.A., 2019. Tide and mean sea level trend in the west coast of the Arabian Gulf from tide gauges and multi-missions satellite altimeter. Oceanologia 61 (4), 401—411. https://doi.org/10.1016/j.oceano.2019.05.003

Sterl, M.F., Delandmeter, P., van Sebille, E., 2020. Influence of barotropic tidal currents on transport and accumulation of floating microplastics in the global open ocean. J. Geophys. Res.-Oceans 125, e2019JC015583. https://doi.org/10.1029/2019JC015583

Sultan, S.A., Moamar, M.O., Elghribi, N.M., Williams, R., 2000. Sea level changes along the Suadi coast of the Arabian Gulf. Indian J. Geo-Mar. Sci. 29, 191—200. http://nopr.niscair.res.in/handle/123456789/25532

Truong, D.D., Tri, D.Q., Don, N.C., 2021. The impact of waves and tidal currents on the sediment transport at the sea port. Civil Eng. J. 7 (10), 1634—1649.

Zakaria, S., Al-Ansari, N., Knutsson, S., 2013. Historical and future climatic change scenarios for temperature and rainfall for Iraq. J. Civ. Eng. Archit. 7, 1574—1594. https://doi.org/10.17265/1934-7359/2013.12.012

Oceanologia 65 (2023) 503—516

Available online at www.sciencedirect.com

ScienceDirect

journal homepage: www.journals.elsevier.com/oceanologia

ORIGINAL RESEARCH ARTICLE

Remotely induced storm effects on the coastal flooding along the southwest coast of India

P.S. Swathy Krishna[a,b], **Valliyil Mohammed Aboobacker**[c], **Madipally Ramesh**[a,b,*], **L. Sheela Nair**[a]

[a] *National Centre for Earth Science Studies, Thiruvananthapuram, Kerala, India*
[b] *Cochin University of Science and Technology, Cochin, Kerala, India*
[c] *UNESCO Chair in Marine Sciences, Environmental Science Center, Qatar University, Doha, Qatar*

Received 9 January 2023; accepted 29 March 2023
Available online 18 April 2023

KEYWORDS
IASO swells;
ERA5 winds;
Indian Ocean;
Kerala coast;
Coastal inundation;
Wave runup

Abstract The southwest coast of India is exposed to long-period swells propagated from the South Indian Ocean during pre- and post-monsoon seasons. Although swells from the Southern Ocean and Atlantic Ocean were identified in the North Indian Ocean, their existence and impact along the southwest coast of India were not well investigated. On 19 March 2019, the Valiyathura-Shangumukham coastal stretch along the southwest coast of India experienced an unexpected coastal inundation without having a prompt forecast/warning, and not induced by a storm/cyclone in its vicinity. The present study investigates the causative forces of this inundation and estimates the wave runup and inundation. The study reveals that an unusual swell system was developed in the Indian-Atlantic-Southern Oceans (IASO) interface during 10—12 March and propagated towards the southwest coast of India. The measured wave spectra off Varkala clearly depicts the presence of long-period swells ($T_p > 18$ s), which dominantly occurred as single-peaked. Wave modelling has been carried out to characterize the wave transformation associated with the "IASO interface swells" along the southern Kerala coast. A wave runup of up to 0.93 m height and a coastal inundation of up to 83 m onshore have been estimated during this event.

* Corresponding author at: National Centre for Earth Science Studies, Thiruvananthapuram, Kerala, India; Cochin University of Science and Technology, Cochin, Kerala, India.
E-mail address: ramesh.madipally@ncess.gov.in (M. Ramesh).

Peer review under the responsibility of the Institute of Oceanology of the Polish Academy of Sciences.

ELSEVIER Production and hosting by Elsevier

https://doi.org/10.1016/j.oceano.2023.03.003

1. Introduction

Swells play a major role in the distribution of energy from the deep ocean to nearshore regions and contribute to wave-induced coastal dynamics as they interact with wind seas, tides and currents (Hanley et al., 2010). Waves in the North Indian Ocean (NIO) are generally dominated by the swells propagated from the South Indian Ocean (SIO) during pre- and post-monsoon seasons (Anoop et al., 2015; Sashikant et al., 2013). However, local wind seas induced by sea breeze often superimpose with these swells and result in complex sea states during pre-monsoon seasons (Glejin et al., 2013; Piyali et al., 2019; Vethamony et al., 2011). In the Arabian Sea (AS), southwest monsoon (SWM) winds and tropical cyclones generate high swells (Aboobacker et al., 2011a). Long-period swells from far SIO and the Atlantic Ocean were also identified in the AS (Samiksha et al., 2011). The AS also experiences the northerly shamal and makran swells during pre- and post-monsoon seasons (Aboobacker et al., 2011b; Aboobacker and Shanas, 2018; Anoop et al., 2020).

Long-period swells generated by tropical or extra-tropical storms cause flooding along the coasts in different parts of the world (Andrew et al., 2015; Kurian et al., 2009a). Along the SW coast of India, the relative narrowness of the continental shelf and a near perpendicular orthogonal of swells enhance the wave setup and increase the swell heights compared to the other coasts of India (Remya et al., 2016). In low-lying areas, the combination of long-period swells and spring tides can contribute to nuisance flooding (Hamed et al., 2015). There were such incidents occurred along the Kerala coast on a few occasions (Kurian et al., 2009b). For example, high swells that occurred in May 2005 have marooned almost all the low-lying areas of the Kerala coast and the southern coast of Tamil Nadu. The coastal floods that occurred at Chavakkad in September 2021, at Alappuzha in September 2015, and at different parts of the Kerala coasts in April 2018, were a few other incidents as reported by the news media. Recently (May 2021), cyclone Tauktae caused severe flooding at Thiruvananthapuram, the southern tip of the Kerala coast. Most of these events are associated with an initial receding of coastal waters, followed by strong swells, called Kallakadal (Kurian et al., 2009b). During the Kallakadal of May 2005, the Adimalathura coast, near Thiruvananthapuram was inundated about 500 m inland (Kurian et al., 2009b).

When waves approach the coast, most of the energy dissipates across the surf zone by breaking. A part of this energy is converted into potential energy and makes a runup on the beach (Stockdon et al., 2006). The swash is dominated by incident energy on reflective beaches, and more extreme wave runup occurs for swells with wavelengths between 500 m and 800 m (Abdalazeez Ahmed, 2012). Highly reflective beaches have a slope between 4° and 10° with medium sand grains (Scott et al., 2011). The Kerala coast has been distinctively classified into high-energy, medium energy and low-energy regions, depending upon the beach face and grain size distributions (Kurian, 1987). The southern Kerala coast falls under high-energy coast, and the impact of flash flood events along this coast is relatively higher (Ramesh et al., 2022).

The number of flooding events along the Kerala coast is increasing year by year, and most of the events were not given proper scientific attention (Sachin et al., 2014). Future projections indicate that extreme wind speeds and wave heights in the SIO are increasing towards the end of the century (Krishnan et al., 2022). The connectivity of flash floods with SIO swells is somewhat known (Remya et al., 2016). However, this needs to be further elaborated on the context of swells generated at an interface between the Indian, Atlantic and Southern Oceans (IASO). The present study aims to fill this gap by exploring swell generation regions in the IASO interface, which propagate towards the NIO and impact the southern Kerala coast. Flooding of March 2019 has been investigated by identifying causative remote storms, swell generation, and propagation, and analyzing the nearshore wave regime including wave runup. The study also emphasises the importance of continuous monitoring and prediction of distant storms and corresponding swell propagation, which contribute significantly to the pre-monsoon coastal flooding.

2. Study area

Kerala is an Indian coastal state located at the southwest of the subcontinent with a coastline of 590 km distributed across 222 coastal villages with an average population density of 2,262 people per square kilometre (Sachin et al., 2014). Nearly 40% of the population lives within 25 km of the coast and as the sea level rises, low-lying land areas and small islands could shrink due to flooding and coastal erosion, forcing large-scale migration inland. Thiruvananthapuram coast is located at the extreme south of Kerala coast. Figure 1 shows the study region that extends from Kanyakumari in the South to Varkala in the North covering approximately 120 km alongshore. The Valiyathura is in the middle, and Shangumukham is 2.4 km north of it. The Thiruvananthapuram coast is a high-energy coast, where the shelf gradient is 33.33×10^{-3}, the highest along the SW coast of India (Kurian, 1987; Ramesh et al., 2022). The mean grain size here is around 0.30 mm. The annual mean wind speed is around 4.3 m/s along the Thiruvananthapuram coast and 5.0 m/s in the offshore region (Abdulla et al., 2022). This region experiences a maximum H_s of around 6.0 m and 2.0 m during SW monsoon and during fair-weather seasons, respectively. Whereas the mean H_s are around 3.0 m and 1.5 m during SWM and fair-weather seasons, respectively (Baba and Joseph, 1988).

3. Data and methodology

3.1. Wind data

This study utilises the ECMWF Reanalysis v5 (ERA5) winds over a semi-global domain (0°—120° E, 90°S—30°N) covering the Indian Ocean and part of the Southern, Atlantic and Pacific Oceans to evaluate the storm events which cause the flash floods off Valiyathura. These winds are also used as the surface forcing in the wave simulations. The ERA5 winds are extracted for every 1 hour on a 30 km × 30 km spa-

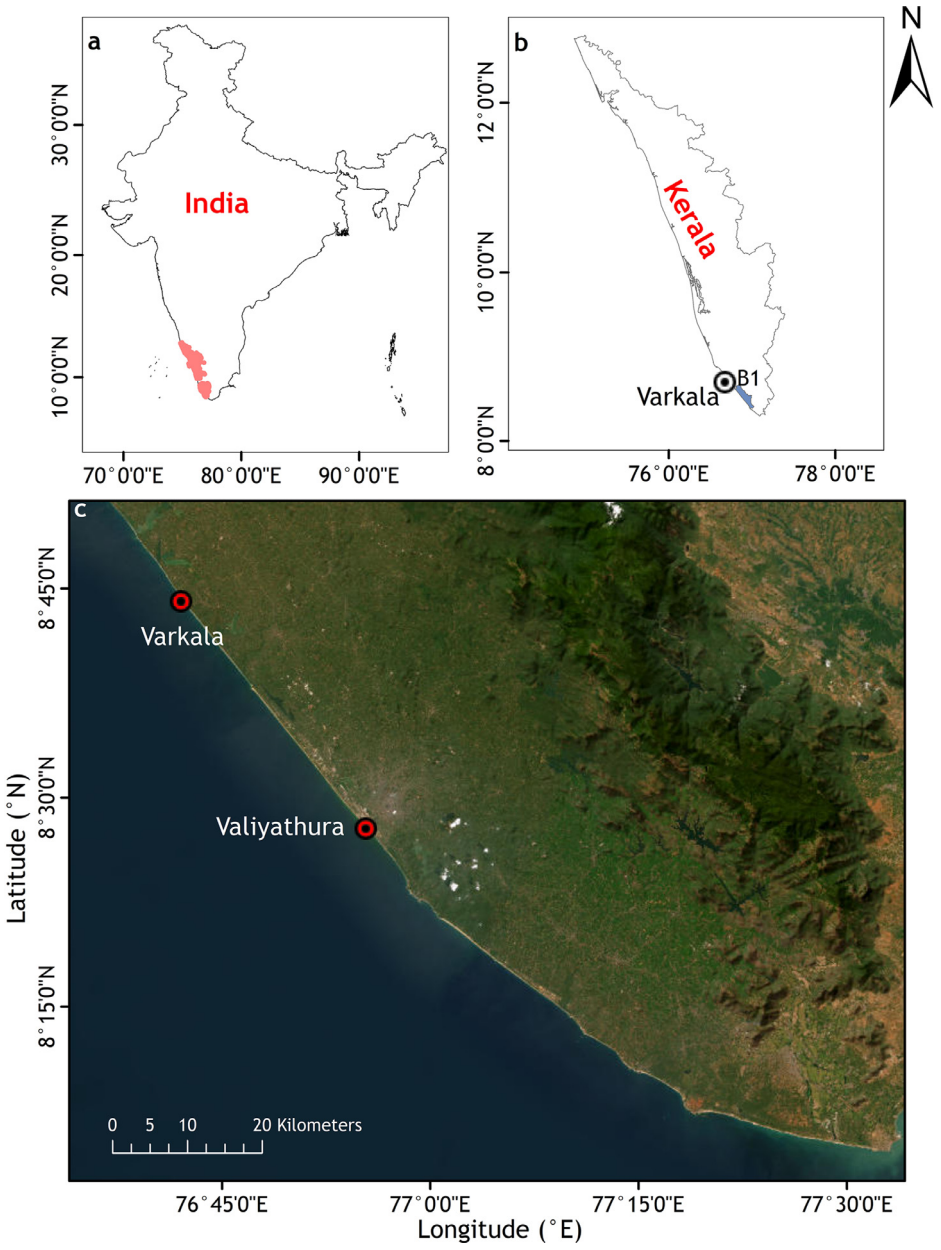

Figure 1 Location map of the study area: a) India sub-continent, b) SW coast of India with buoy location (B1), and c) Thiruvananthapuram coast. Shangumukham is 2.4 km north of Valiyathura.

tial resolution during March 2019 (https://www.ecmwf.int/en/forecasts/datasets/reanalysis-datasets/era5). The ERA5 winds are found satisfactory for the global ocean modelling (Parsons et al., 2018). Recent studies on the wind-wave characteristics over the Indian ocean has made use of ERA5 datasets and are validated with measurements (Aboobacker et al., 2021; Mahmoodi et al., 2019; Parsons et al., 2018; Sreelakshmi and Prasad, 2020a, b). The ERA5 waves are also extracted for every 1 hour on a 55 km × 55 km spatial resolution during March 2019 for the spatial wave data analysis.

3.2. Wave measurements

The present study analyses the measured wave spectra and integral parameters along the Thiruvananthapuram coast. A directional wave rider buoy (DWR-MKIII) developed by Datawell BV, Netherlands, was deployed at 15 m depth off Varkala during 01—22 March 2019 (Figure 1b). The DWR is provided with the HF link facility for online transmission with wave data output rate of 1.28 Hz for distances up to 50 km over the sea. The heave range of the buoy is −20 m to +20 m with a resolution of 1.0 cm. The range of frequency in the spectra is 0.01—0.58 Hz (wave period between 1.6 s and 100 s), and the directions are from 0° to 360°. Continuous wave data for every 30 minutes with a sampling period of 20 minutes were collected.

3.3. Wave modelling

The wave runup calculations require fine-resolution wave data close to the shore. Therefore, numerical wave

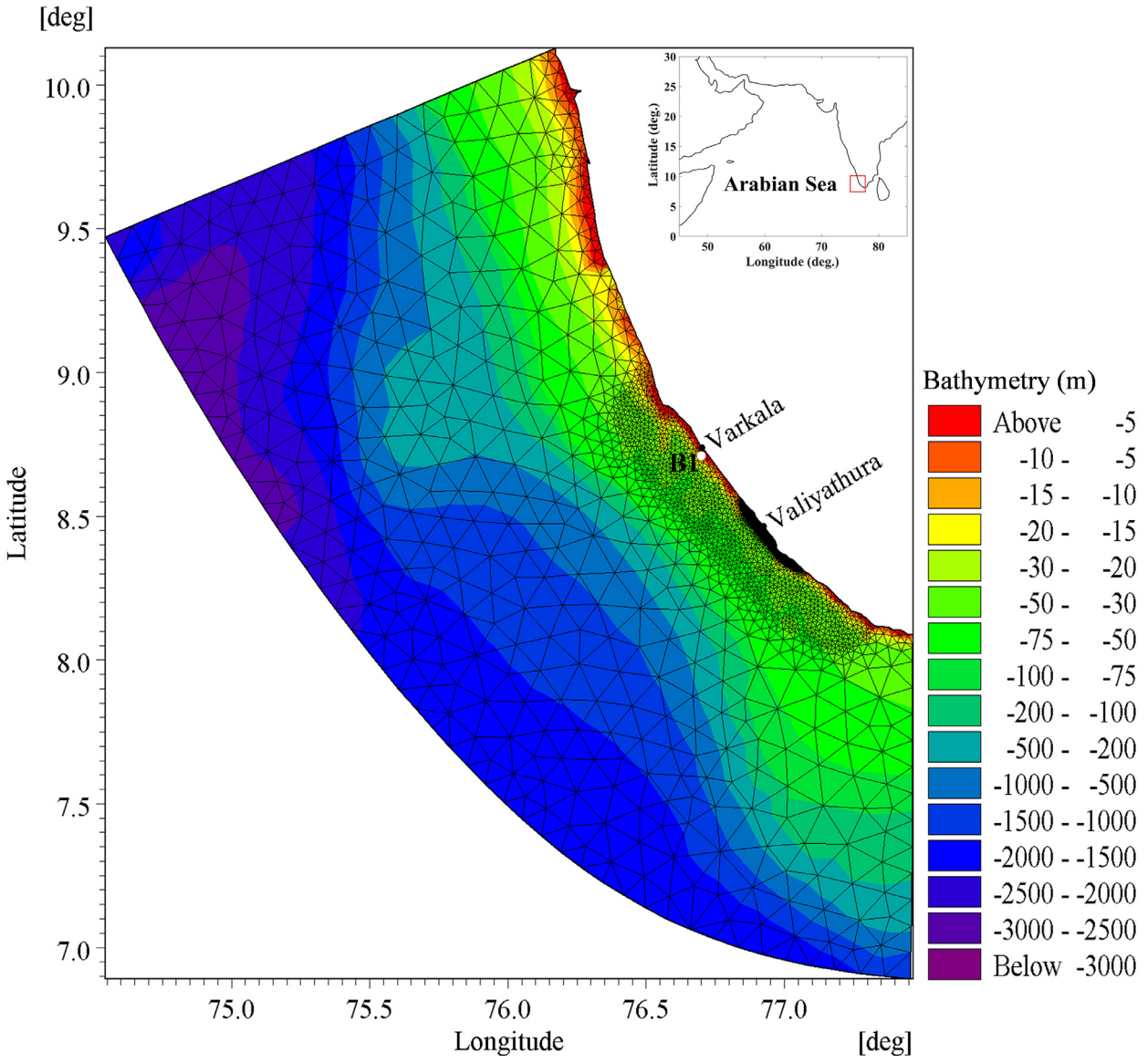

Figure 2 Model domain, bathymetry and flexible mesh used for wave simulations off the Thiruvananthapuram coast. B1 is the wave measurement location. Valiyathura is the region where the flash floods occurred on 19 March 2019.

simulations have been carried out along the Thiruvananthapuram coast to resolve the shallow water effects and to extract the nearshore wave parameters (at 5 m depth) for the wave runup calculations. For this purpose, a local model has been set up using MIKE 21 — Spectral Waves (DHI, 2019). The model domain extends 220 km in the north-south axis covering the entire Thiruvananthapuram coast and has a width of 199 km in the north and 133 km in the south (Figure 2). 1 arc-minute resolution ETOPO1 data (Amante and Eakins, 2009) along with digitized hydrographic charts available at National Centre for Earth Science Studies (NCESS) has been used to generate the model bathymetry. A variable resolution mesh has been adopted for the proper representation of deep, intermediate, and shallow waters. The mesh size in the outer region is around 6—7 km (side of the triangle), while that in the intermediate zone is around 1.4 km and that at the Valiyathura coast is around 300 m. The ERA5 winds have been used to force the surface boundary, while the wave parameters extracted from ERA5 waves have been applied as the boundary conditions all along the 3 open boundaries. The simulations have been carried out in March 2019.

The wave model has been tuned with different values of coefficients such as dissipation due to bottom friction (S_{bot}), white capping dissipation coefficient (C_{dis}) and wave breaking parameter (γ). Earlier studies used C_{dis}, and γ as calibration parameters in the nearshore wave simulations along the SW coast of India (Nair et al., 2011, 2013; Parvathy et al., 2014). Kurian et al. (2009a) applied varying bottom friction estimated using mean grain diameter (D_{50}) ranging from 0.00025 m to 0.0003 m for the wave simulations along the southern Kerala coast. In the present study, a better calibration has been obtained when $C_{dis} = 2.6$ and $\gamma = 0.5$. We used $D_{50} = 0.0003$ obtained from field investigations to calculate the bottom dissipation.

3.4. Beach slope

The beach slopes at Valiyathura and Shangumukham coast are measured by field surveys using clinometer compass (McFall, 2019). The compass has been placed at the mid-water line during low tide, to measure the foreshore slope of the beach. Three field surveys are conducted in March 2019, to characterise the beach slopes.

3.5. Wave runup computations

The wave induced maximum water elevation on the foreshore is estimated as the extreme wave runup using both wave (H_s and T_p) and beach slope (β) (Torres-Freyermuth et al., 2019). The amount of runup is the extreme vertical height above still water level that the rush of water reaches. It is affected by wave set up and swash (Stockdon et al., 2006). The wave set up is the elevation of the mean water level (MWL) above the still water line due to onshore mass transport by the action of waves. We find that the selected coastal stretch, namely Shangumukham to Valiyathura along the Thiruvananthapuram coast is a dissipative beach based on the Irribarren number (ξ) and foreshore slope β, which are collectively defined as:

$$\xi = \tan\beta/\sqrt{H_b/L} \quad (1)$$

where L is the wavelength and H_b is the breaker wave height.

The estimated β and ξ for the Thiruvananthapuram coast are 0.034—0.047 radians and 0.20— 0.27, respectively. When $\beta <$ 0.1 radians and ξ <0.3, the runup is independent of β (Stockdon et al., 2006). Thus, runup can be approximated to Equation (2) as follows:

$$R_{2\%} = 0.043(H_sL)^{1/2} \quad (2)$$

Based on this approximation the wave runup along the Thiruvananthapuram coast has been estimated.

4. Results and discussion

4.1. Spectral variability in response to remote storms

The waves measured from 1 to 22 March 2019 indicate that the H_s are moderate except on a few occasions (Figure 3). Interestingly, the highest H_s occurred in two instances — one with a lower T_p (about 9 s on 6 March) and the other with a relatively higher T_p (around 20 s on 18 March). The corresponding mean wave directions are 200° and 210°, respectively. The former is associated with a wind sea-dominated sea state, while the latter is associated with a long-period swell-dominated sea state. Typically, there are three sea states along the west coast of India: wind sea-dominated, swell-dominated and co-existence of wind seas and swells in nearly equal proportion (Aboobacker et al., 2011a; Rashmi et al., 2013). The presence of two wind sea components from two different directions along with a distant swell (Aboobacker et al., 2014) and two swell components from different directions along with wind seas (Anoop et al., 2020) were also identified along the west coast of India.

The measured 1D spectra measured highlights typical and peculiar spectral characteristics (Figure 3). Generally, they are a combination of single-peaked and multi-peaked spectra during the measurement period. The spectra on 06 March reveal the co-existence of a swell and a wind sea, during which the H_s is above 1.0 m. The frequencies corresponding to the primary and secondary peaks are 0.11 Hz (swell) and 0.24 Hz (wind sea), respectively. The generation area of the swell present here could be the tropical/subtropical SIO as the peak swell period is only around 9s, during which the peak swell direction was 180°. This is a potential swell generation area during the pre- and post-monsoon season as evidenced by Aboobacker et al. (2011a). The peak wind sea direction was around 305°, which is due to a sea breeze. Sea breeze activity is prominent along the SW coast of India during the pre-monsoon season (Aparna et al., 2005). Although wind sea energy varies, the influence of sea breeze is evident in the wave spectra in variable frequencies throughout the measurement period.

On 09 March, the spectrum is single-peaked consisting of a dominant SIO swell from 195° having a peak frequency of about 0.095 Hz, during which the energy in the wind sea region is very low. The absence of wind sea peak here is associated with low/no wind conditions (at 12 AM), which is apparent from the diurnal patterns of the coastal winds along the southwest coast of India during the pre-monsoon season (Aboobacker et al., 2021, 2014).

On 16 March, the region experienced two major swell components; primary swell was from 195° with a frequency of about 0.08 Hz and the secondary swell was from 185° with a frequency of about 0.11 Hz. This is a mixed sea state with swells from far and near regions of the SIO. In the following days (17 and 18 March), the primary peak has been shifted to a relatively lower frequency region with a narrow spectral band having a peak frequency of about 0.05—0.055 Hz, and the energy in the secondary swell peak has been gradually weakened. During these days, the primary swell directions were shifted to 210°, while the secondary swells remained at 180—185°. This brings the possibility of longer swells propagating from a region farther than the swells generated in the preceding days. On 19 March, the secondary swell peak has been disappeared, while the primary peak (from 210°) remained in the lower frequency region with a peak frequency of about 0.065 Hz. These swells have had a higher celerity in absence of muti-frequent and multi-directional waves. In the nearshore waters, especially in the breaker zone, the transformation of kinetic energy to potential energy yields to higher wave heights along with strong elliptical/linear motion for the particles under the waves. On a flatty beach, this may lead to considerable wave runup and coastal inundation. The influence of these longer swells has been gradually weakened and the spectra started to retain the pre-existing conditions in the following days, as seen from 20 to 22 March.

4.2. IASO interface swells

The swells present along the west coast of India are predominantly propagated from the SIO (Aboobacker et al., 2011a; Remya et al., 2016). Although swells from the Southern Ocean (SO) and Atlantic Ocean (AO) are present in the NIO (Alves, 2006; Samiksha et al., 2011), their impact along the

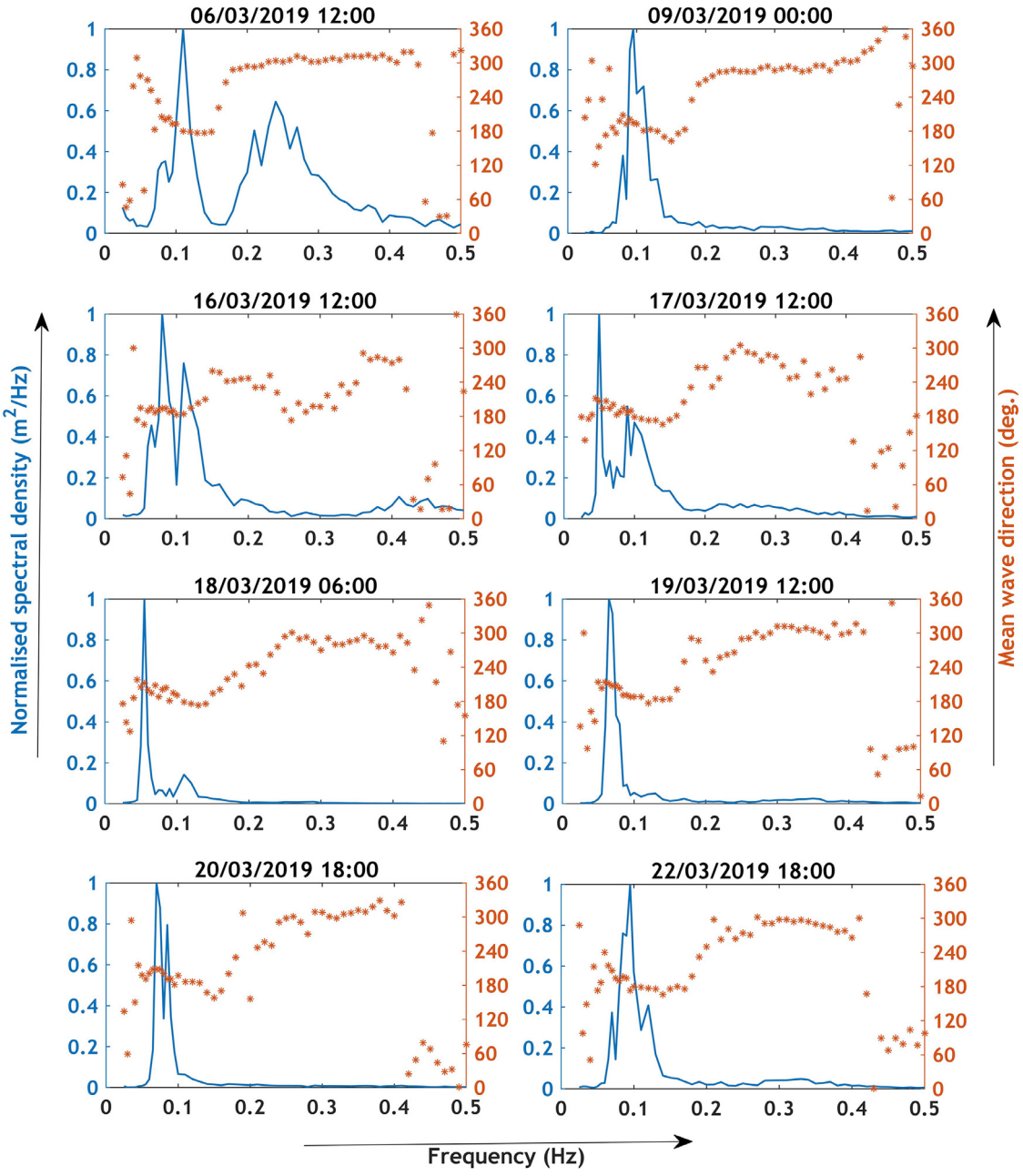

Figure 3 1D wave spectra and corresponding MWD during different wave conditions.

west coast of India has not been well-investigated. Here, the genesis of distant swells has been analysed with reference to the spectral variability of Varkala. The ERA5 winds show that the IASO interface experiences large storms, out of which a few storms generate S/SSW/SW winds (Figure 4), which can generate swells from the respective directions and propagate towards the west coast of India. The IASO interface winds from S/SSW/SW directions are evident during 10—12 March 2019, which was initially formed in the AO-SO interface, and ultimately the system has made an eastward propagation to the IO-SO interface with considerable spatial enhancement. The wind speeds during this event are of the order of 15—25 m/s. The storm has been weakened in the successive days, and the southerly wind components were disappeared. There have been two tropical cyclones formed in the SIO during the study period: (i) Idai developed east of Madagascar (10—14 March 2019) and (ii) Savannah developed southeast of Indonesia (14—21 March 2019) with maximum wind speeds of about 195 km/hr and 165 km/hr, respectively (https://tropic.ssec.wisc.edu/storm_archive/2019/storms/tracks/). Compared to the IASO interface winds, the impact of these cyclones is limited to relatively small regions.

It is evident from ERA5 waves (Figure 5) that strong southerly swells developed in the AO-IO interface (around 10°E) started to make a clear presence in the SIO on 11 March as it propagates towards the north. The swell generation area has been further shifted towards the east according to the propagation of the storm system, while the southerly swells continued to develop and propagate

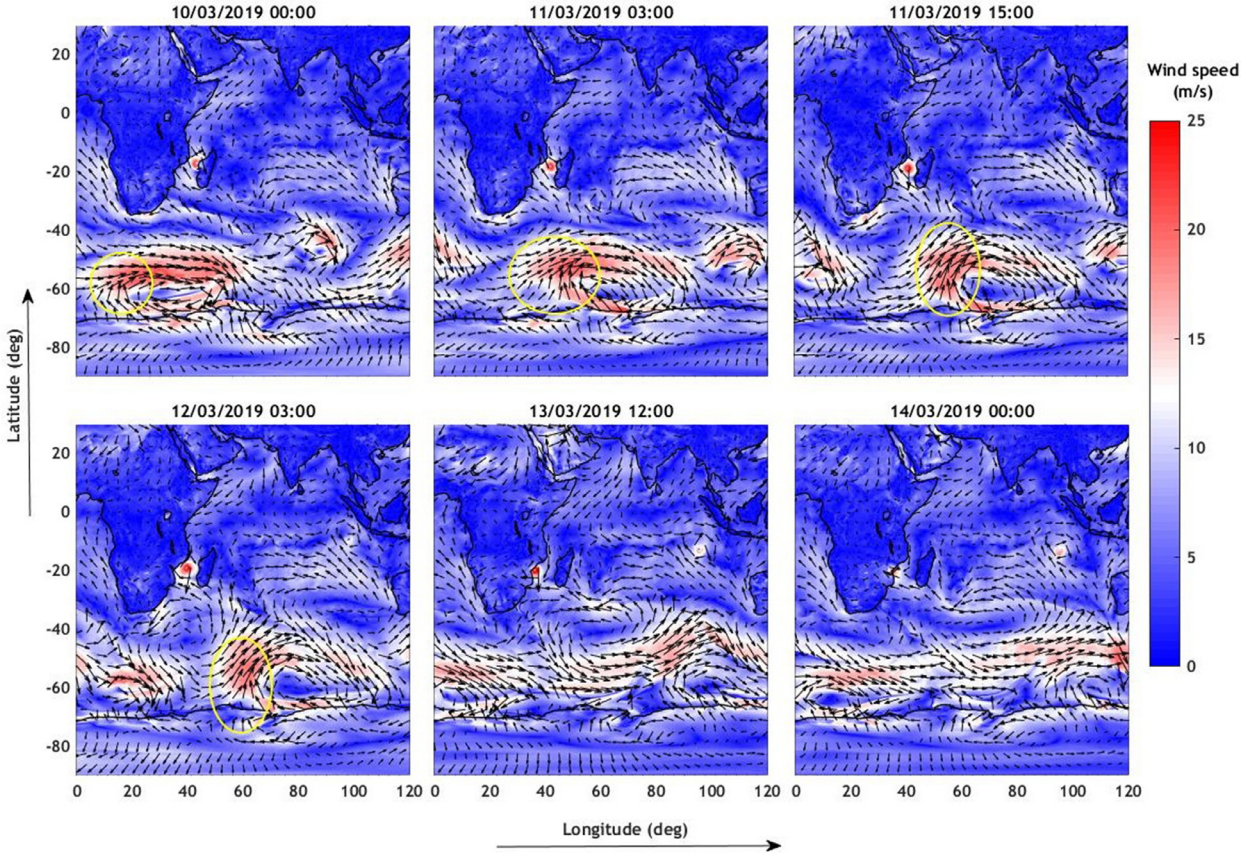

Figure 4 Snapshots of ERA5 winds during 10—14 March 2019.

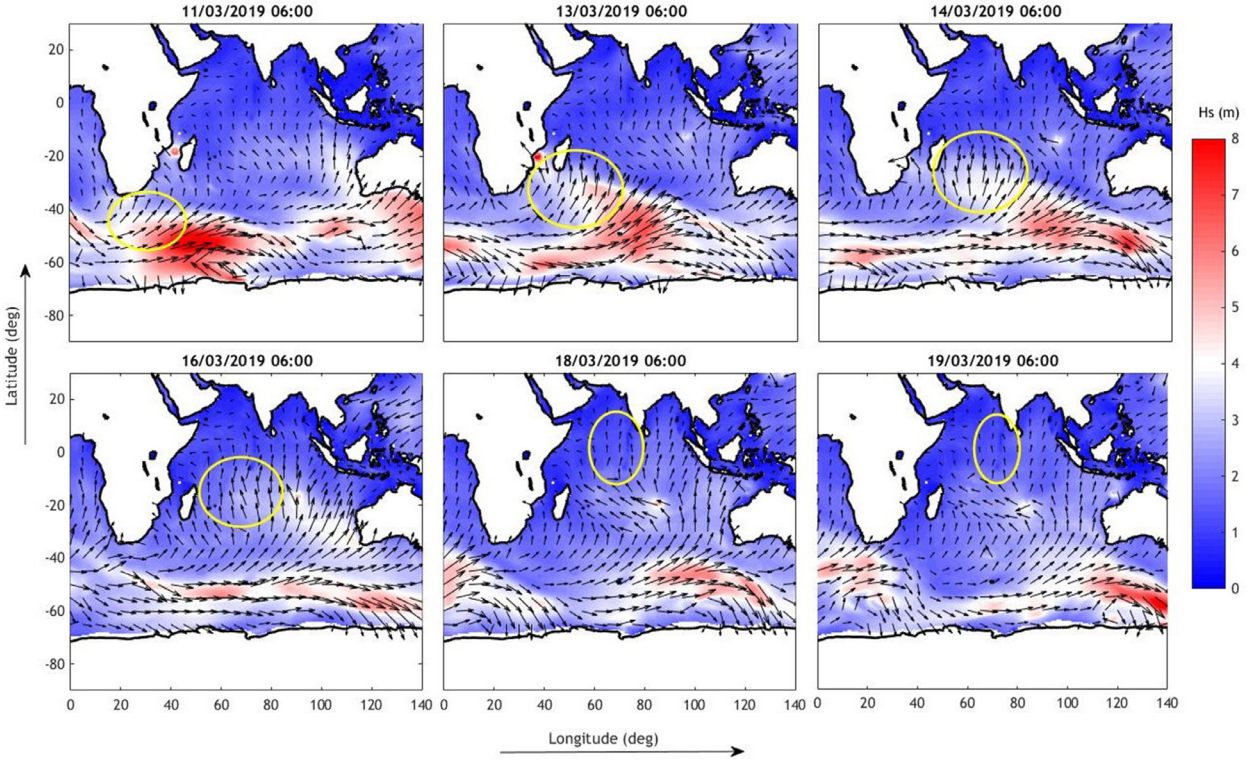

Figure 5 Snapshots of ERA5 wave heights and directions during 10—14 March 2019.

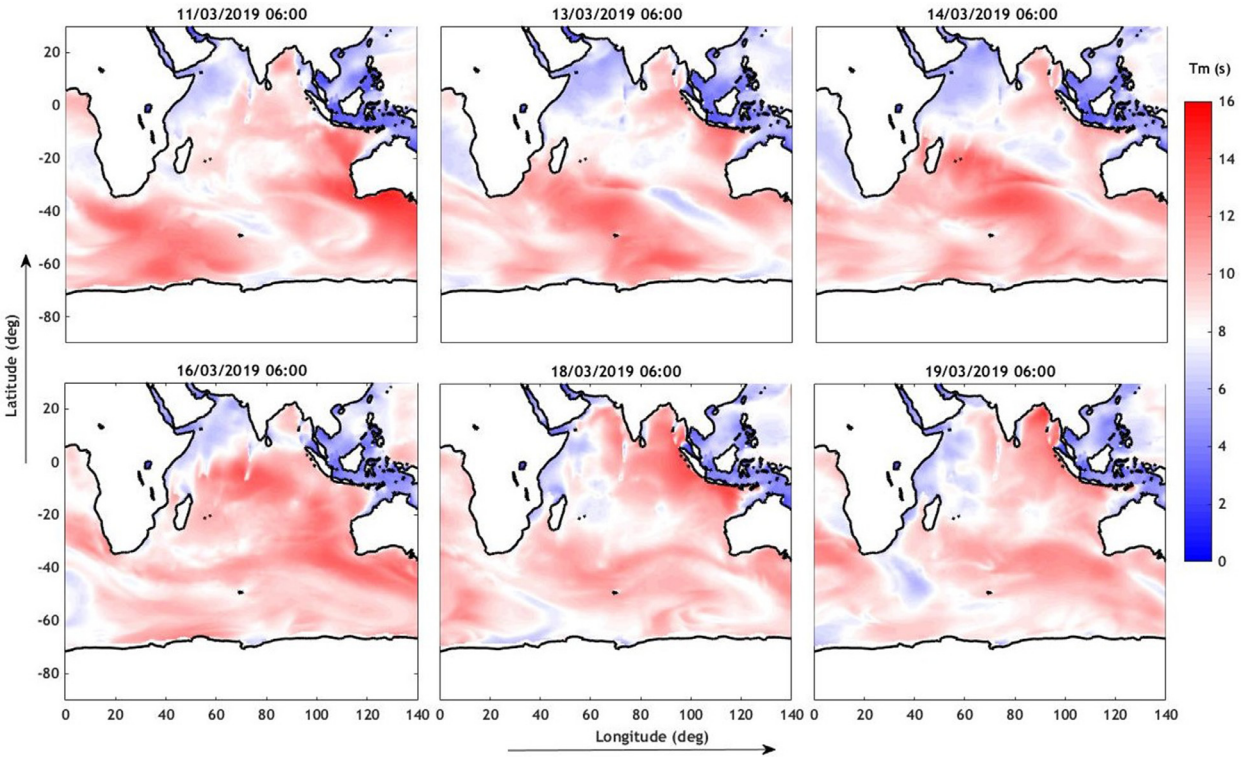

Figure 6 Snapshots of ERA5 mean wave periods during 10—14 March 2019.

through the SIO. On 13 March, these swells reached around 30° S, east of Madagascar, with H_s up to 5.0 m. Although the energy has been gradually attenuated, the swells continued to propagate and reached the AS on 17 March. This has prevailed until 19 March. The wave spectra measured off Thiruvananthapuram indicates the presence of these swells during 17—19 March having peak energy in the very low-frequency region (Figure 4). Since these swells are generated in the IASO interface and propagated towards the NIO, we hereby named them as "IASO interface swells".

The ERA5 mean wave periods (T_m) clearly substantiates the propagation of IASO interface swells through the SIO and NIO. It was not only propagated up to the west coast of India but also identified along the head of BoB (Figure 6). The T_m of the IASO interface swells reach above 12 s in the AS and BoB. A rough estimation of the propagation duration of the swells considering the distance between the storm area and the coast, and the wavelength indicate that the swells generated at around 10°E, 65°S can take at least 7 days to reach the Thiruvananthapuram coast. Thus, the swells generated on 10 March have reached on 17 March. This indicates, the swells reached along the Thiruvananthapuram coast during 17—19 March are dominantly from far distance including AO and SO, which has a higher celerity. When these high wavelength approaches a flat and reflective beach, the possibility of wave runup is high. The wave measurements indicate that the T_p along the Varkala coast increases from about 12 s to 20 s from 17 to 19 March, during which the MWD has been changed from about 200° to 210°, a clear shifting of swells from SIO origin to IASO interface origin (Figure 7). This is a peculiar feature considering the pre-existing wave conditions in this region. Although H_s is not very high (about 1.0 m) during this event, the longer period and corresponding celerity of the IASO interface swells along with the flat beach topography of Valiyathura-Shangumukham stretch together caused the flash floods.

4.3. Model validation

The model results have been validated against the measurements at B1. Figure 7 shows the time series comparison of H_s, peak wave period (T_p) and mean wave direction (WMD) between the model and measurements during 01—22 March 2019. The model parameters have reasonable match with measured values with estimated correlation coefficients of 0.85 and 0.92 for H_s and T_p, respectively. The scatter indices of H_s and T_p are 0.15 and 0.19, respectively, while the bias is 0.01 m and 0.17 s, respectively. The root means square errors for H_s and T_p are $\pm$ 0.15 m and 2.23 s, respectively. The model wave direction has a perfect match with the measurements, except on a few occasions. It has a bias of less than 4°. These comparisons are consistent with the earlier modelling attempts along the southwest coast of India utilizing MIKE 21 SW (Parvathy et al., 2014; Remya et al., 2012), Wavewatch III (Samiksha et al., 2011) and SWAN (Amrutha et al., 2016) Figure 8.

4.4. Nearshore wave transformation and wave runup

4.4.1. Wave transformation

The results of the validated wave model are utilized in this subsection to investigate the nearshore wave transformation and to estimate the wave runup. During the event on 18-19 March, waves approached the coast with a max-

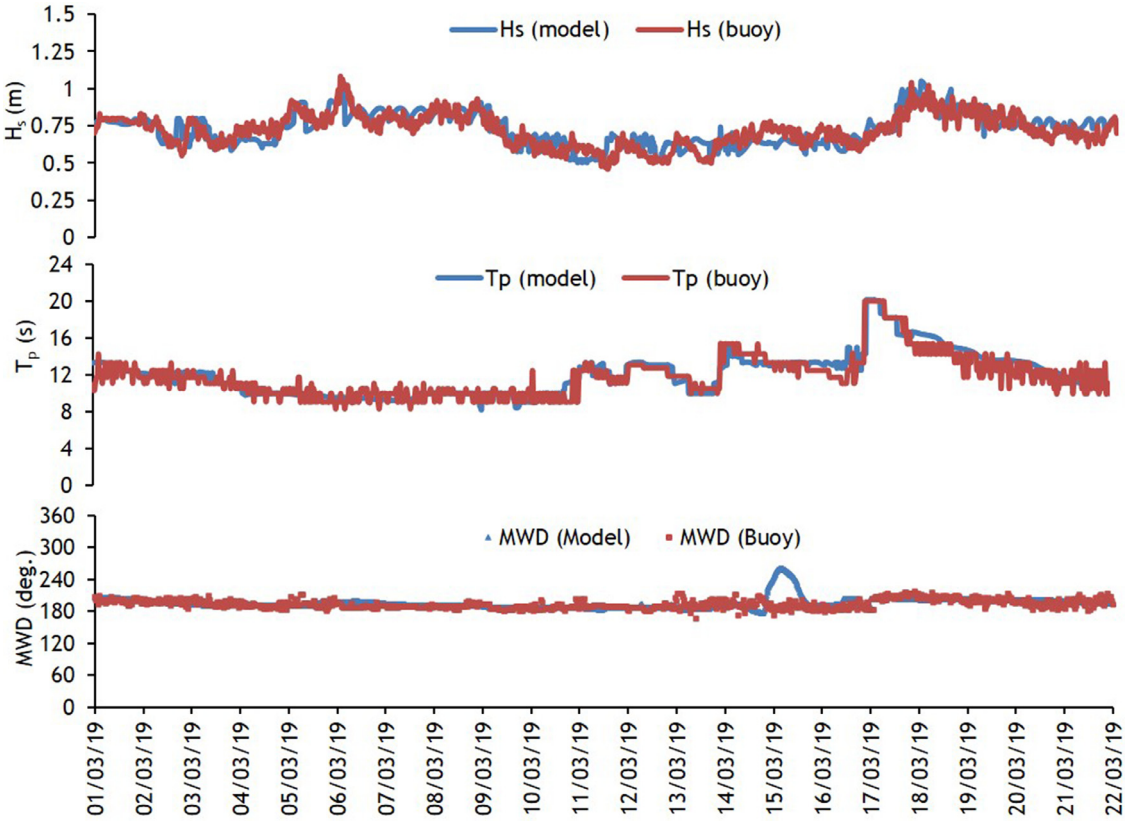

Figure 7 Comparison of measured and modelled significant wave height, peak wave period and mean wave direction off Varkala during 01—22 March 2019.

imum wavelength of 600 m. Thus, the deep, intermediate, and shallow waters can be defined with respect to the depth as d>300 m, 30<d<300 m and d<30 m, respectively. During fair weather season, the wave breaker depth along this coast was around 5—7 m with a breaker height of 1—1.5 m (Swamy et al., 1979). The bottom attenuation resulted a decrease in wave height when the waves were propagated from 1600 m to 50 m and 15 m depth contours, which is consistent with earlier observations along the Thiruvananthapuram coast (Parvathy et al., 2014). As obvious, there are no significant changes in T_m between the depths. The wave refraction enables a shore normal propagation in the nearshore waters, with a shift of around 20—25° from the deep-water waves. The dominant wave direction along the Kerala coast during fair-weather season varies between northwest and southeast (Hameed et al., 2007). During 14—16 March, the waves were approaching from the W. The boundary data applied (ERA5 waves parameters) in the local model also reveals a W/WNW component on the northern boundaries, however, they were not present in the southern regions. The wave model results indicate that this has been propagated towards the coast. The W/WNW component could be due to the effect of sea breeze, which are predominant along the Kerala coast during March (Abdulla et al., 2022).

A slight increase in H_s has been identified when the wave approaches the shore (from 15 m to 5 m). This increment was more pronounced during 18—19 March when IASO swells were present. In addition, the T_m on these days were the highest (10—12 s) of the month. This high T_m indicates that the long-period swells from the IASO interface have approached the shore without considerable interference of locally generated wind seas. The presence of local wind seas generally reduce T_m of the total waves compared to the independent swell T_m (Vethamony et al., 2011). Thus, the persistent higher T_m with an increased wave setup in the shallow waters of Valiyathura-Shangumukham stretch over the fully developed beach have made the runup easier than the other adjacent regions.

4.4.2. Coastal inundation and morphological changes

The study area is part of a straight coastal belt in which the 2.4 km stretch between Shangumukham and Valiyathura has got particular attention in this study. The beach is relatively wider at Shangumukham while the beach slope is relatively small at Valiyathura. Sea-level rise, anthropogenic activities and geomorphological changes by the wave action together contribute to the long-term erosion along the coast. It makes the coast more vulnerable to sudden floodings and inundation.

During 17—19 March 2019, the Valiyathura and Shangumukham coasts were heavily affected by wave runup, wave breaking and inundation. The coastal inundation was evident from the field visits immediately after the event (Figure 9). The beach survey along the Shangumukham coast reveals that the beach is dissipative with slopes ranging between 2° and 6° before the event. On 05 March, it was a fully developed beach with a beach width of 52 m (with a berm at the landward side) and an extended mild slopy beach up to 75 m. This has been altered by the wave

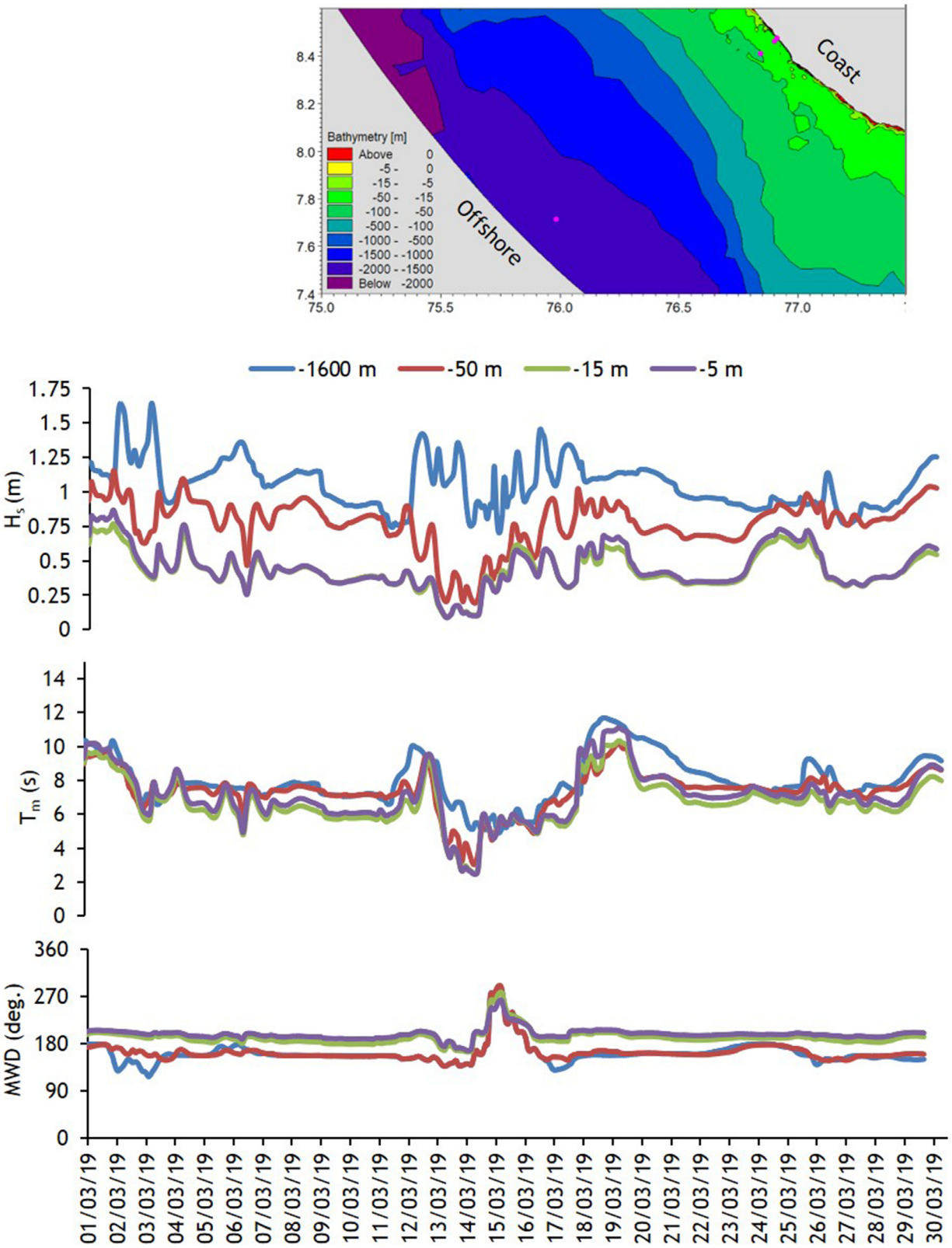

Figure 8 Wave transformation: Spatial variations of bathymetry (contour plot) in the top panel including the extraction locations; changes in wave parameters from the deep ocean (1600 m) to nearshore (5 m) across Valiyathura coast in the bottom panel.

Figure 9 Field photographs of Valiyathura — Shangumukham stretch during the event on 18 March 2019.

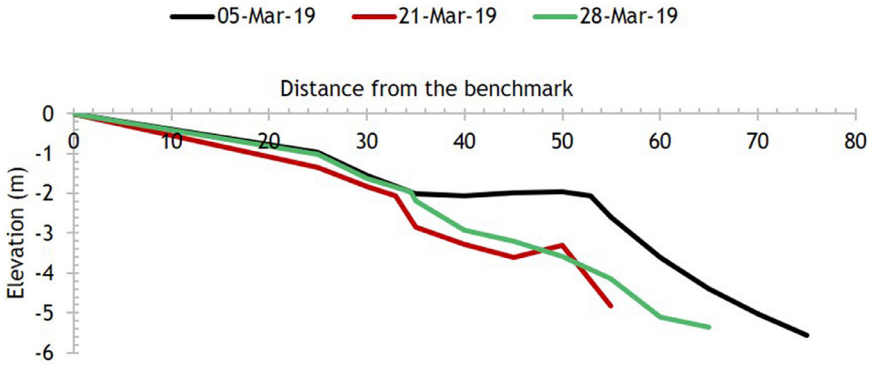

Figure 10 Beach profiles at Shangumukham coast during March 2019.

activity that occurred on 18—19 March. The beach face has turned flat, the fully developed flat beach was extended up to 80 m, and the beach slope was modified with a steep foreshore slope of about 10°. A mean grain diameter (d_{50}) of 0.41 mm observed during this period indicates the presence of relatively fine sand. The water was inundated by almost 80 m up to the permanent benchmark of the survey (steps) (Figure 10).

The post-event scenario indicates that the foreshore slope has been decreased from 10° to 6° with the berm shifted towards the seaside within a week time. Compared to 05 March, a significant erosion was occurred due to the flood event with a beach loss of 20 m. The flooding normally reduces the capacity of the beach acting as a natural barrier against erosion (Miguel et al., 2021). Kurian et al. (2009a) identified similar erosion by the effects of southerly swells, which generated a southward alongshore current, gets amplified and enabled a wave setup during event. The post-flood profile (28 March) at the Shangumukham coast indicate that the beach has started to retain the pre-existing condition (Figure 10). The characteristics of the inundation occurred due to these long-period swells are quite different from those that occurred due to the cyclonic activity (Gayathri et al., 2017; Rao et al., 2020), on which the coast re-building may take a longer duration.

4.4.3. Wave runup

The wave runup is higher in a mild slopy beach that results in greater landward inundation during high waves (Gayathri et al., 2017). Here, the runup exceeded by 2% of the waves ($R_{2\%}$) is estimated corresponding to the daily H_{max} for March 2019 on the Shangumukham beach (Figure 11). This shows that the highest values are obtained during 18 March compared to the pre- and post-event scenarios. On 18 March, the $R_{2\%}$ has reached 0.93 m with H_{max}= 1.37 m and T_p= 18.5 s. On the following day (19 March) it was 0.8 m with H_{max}= 1.7 m and T_p= 17 s. However, the $R_{2\%}$ corresponds to the highest H_{max} (2.11 m) was only 0.59 m, which was occurred during 13 March with T_p below 15 s. This shows that the T_p has more dependency on the runup rather than the H_{max} and the persistence of long-period swells of above 18 s for more than a day has resulted in the coastal flooding along the Valiyathura-Shangumukham coastal stretch.

The highest wave runup along the Indian coasts occurred during 2004 tsunami. It went up to 4.17 m height along the coast of Tamil Nadu and inundated 238 m inshore (Seelam et al., 2005). The runup varied along Kerala coast due to the influence of bottom topography in channelising the tsunami waves. The runup height was 3.5 m along the north Kerala coast and 5.0 m along the south Kerala coast (Narayana et al., 2007). Generally, the increased runup variability is attributed to low frequency wave which dominates the swash (Torres-Freyermuth et al., 2019). Therefore, under long-period swell dominant conditions, the swash has contributed to the high wave runup on 18—19 March. The IASO swells reached the Thiruvananthapuram coast on 17 March (Figure 4). As the swell activity continued, the wave setup increased and accordingly the runup has reached to

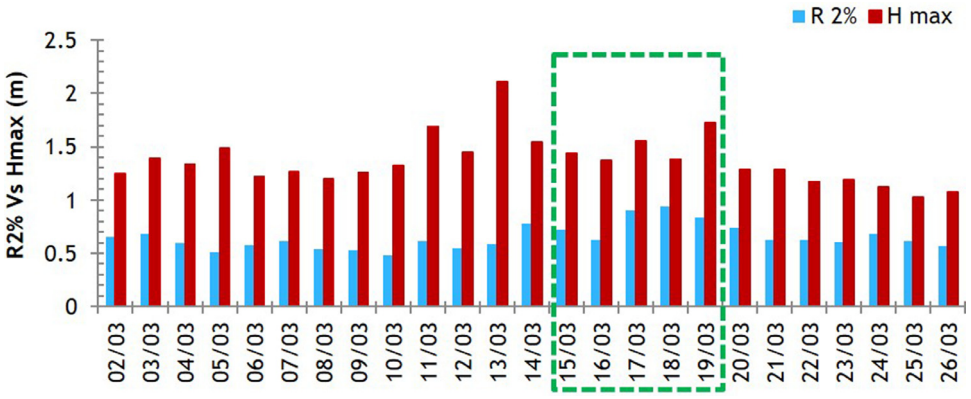

Figure 11 Wave runup along Shangumukham beach.

a height of 0.6 to 0.89 m along the Shangumukham coast on 18 March. It is further developed to 0.93 m on 19 March which contributed to the flooding and inundation over the Valiyathura-Shangumukham stretch.

5. Conclusions

The coastal inundation that occurred along the Valiyathura-Shangumukham stretch during March 2019 was investigated through the analysis of ERA5 winds and waves over a global domain, fine-scale modelling for the Thiruvananthapuram coast and estimation of wave runup and inundation for the affected region. The study identified that a storm system was developed in the Indian-Atlantic-Southern Oceans (IASO) interface during 10—12 March 2019, from where the southerly components generated high swells having significant wave heights of the order of 6.0—8.0 m and propagated towards the North Indian Ocean. These swells have a clear incidence along the southwest coast of India as evident from the measured spectra. The arrival time of the swells estimated (~7 days) was matched well with the low-frequency spectra measured off Varkala. The high celerity of these waves along with the presence of a fully developed/reflective beach made a quick runup of waters towards the shore, which caused an inundation of up to 83 m with a runup height of up to 0.93 m.

There were several wave runup events occurred at different parts of the southwest coast of India in the past; most of them were associated with long-period swells during fair-weather seasons (pre- and post-monsoon seasons). A few of them were investigated in relation to the Kallakadal phenomena, which are somewhat predictable considering the recent advances in wave forecasts in the country. However, the wave runup event of March 2019 was not expected as there were no high swell forecasts or warnings related to it. Our analysis indicates that this event is a localised effect of a remote forcing, originating from the IASO interface. Similar events were often ignored as the swell heights were not very high along the southwest coast of India, but their celerity does an impact. A more detailed understanding of the IASO interface swells including their climatological features is our future scope. This will help to better assess the forecasts and provide early warnings to the public.

Acknowledgements

The authors would like to thank Mr Sarankumar S.G., Mr Akhildev S., Dr Prasad R., Dr Anoop T.R., Dr Glejin J. and Ms Amrutharaj V., for their valuable support during fieldwork and laboratory analysis. The authors would like to extend their gratitude towards the Director, NCESS and the Ministry of Earth Sciences for extending their support and funding for the research. The second author acknowledges the support of the UNESCO Chair in Marine Sciences at Qatar University, funded through the project, QUEX-ESC-QP-TM-18/19-01.

Declaration of competing interest

The authors declare that they have no known competing financial interests or personal relationships that could have appeared to influence the work reported in this paper.

CRediT authorship contribution statement

P.S. Swathy Krishna: Conceptualization, Investigation, Methodology, Software, Formal analysis, Validation, Writing — original draft, Writing — review & editing. **Valliyil Mohammed Aboobacker:** Conceptualization, Investigation, Formal analysis, Writing — original draft, Writing — review & editing. **Madipally Ramesh:** Software, Data curation, Formal analysis, Visualization, Resources, Writing — original draft, Writing — review & editing. **L. Sheela Nair:** Project administration, Resources, Supervision, Writing — review & editing.

References

Abdalazeez, A., 2012. Wave runup estimates at gentle beaches in the Northern Indian Ocean. Faculty of Mathematics and Natural Sciences, Geophys. Inst., Univ., Bergen, 31. https://doi.org/10.13140/RG.2.2.29367.55207

Abdulla, C.P., Aboobacker, V.M., Shanas, P.R., Vijith, V., Sajeev, R., Vethamony, P., 2022. Climatology and variability of wind speeds along the southwest coast of India derived from CFSR winds. Int. J. Climatol. 42. https://doi.org/10.1002/joc.7767

Aboobacker, V.M., Shanas, P.R., 2018. The climatology of shamals in the Arabian Sea part 2: surface waves. Int. J. Climatol. 38, 4417—4430. https://doi.org/10.1002/joc.5677

Aboobacker, V.M., Rashmi, R., Vethamony, P., Menon, H.B., 2011a. On the dominance of pre-existing swells over wind seas along the west coast of India. Cont. Shelf Res. 31 (16), 1701—1712. https://doi.org/10.1016/j.csr.2011.07.010

Aboobacker, V.M., Vethamony, P., Rashmi, R., 2011b. "Shamal" swells in the Arabian Sea and their influence along the west coast of India. Geophys. Res. Lett. 38 (3), 1—7. https://doi.org/10.1029/2010GL045736

Aboobacker, V.M., Seemanth, M., Samiksha, S.V., Sudheesh, K., Jyoti, K., Vethamony, P., 2014. Sea breeze-induced wind sea growth in the central west coast of India. Ocean Eng. 84, 20—28. https://doi.org/10.1016/j.oceaneng.2014.03.030

Aboobacker, V.M., Shanas, P.R., Al-Ansari, E.M., Kumar, V.S., Vethamony, P., 2021. The maxima in northerly wind speeds and wave heights over the Arabian Sea, the Arabian/Persian Gulf and the Red Sea derived from 40 years of ERA5 data. Clim. Dynam. 56 (3), 1037—1052. https://doi.org/10.1007/s00382-020-05518-6

Alves, J.-H.G.M., 2006. Numerical modelling of ocean swells contributions to the global wind-wave climate. Ocean Model. 11, 98—122. https://doi.org/10.1016/j.ocemod.2004.11.007

Amante, C., Eakins, B., 2009. ETOPO1 1 Arc-Minute Global ReliefModel: Procedures, Data Sources and Analysis. NOAA Technical Memorandum NESDIS NGDC-24. https://doi.org/10.7289/V5C8276M,2009

Amrutha, M.M., Sanil Kumar, V., Sandhya, K.G., Balakrishnan Nair, T.M., Rathod, J.L., 2016. Wave hindcast studies using SWAN nested in WAVEWATCH III — comparison with measured nearshore buoy data off Karwar, eastern Arabian Sea. Ocean Eng. 119, 114—124. https://doi.org/10.1016/j.oceaneng.2016.04.032

Andrew, S., Dave, C., Helen, T., 2015. Coastal flooding in England and Wales from Atlantic and North Sea storms during the 2013/2014 winter, Weather — February. RMetS 70 (2), 62—70. https://doi.org/10.1002/wea.2471

Anoop, T.R., Sanil Kumar, V., Shanas, P.R., Johnson, G., 2015. Surface wave climatology and its variability in the North Indian Ocean based on ERA-Interim reanalysis. J. Atmos. Ocean Technol. 32, 1372—1385. https://doi.org/10.1175/JTECH-D-14-00212.1

Anoop, T.R., Shanas, P.R., Aboobacker, V.M., Sanil Kumar, V., Nair, L.S., Prasad, R., Reji, S., 2020. On the generation and propagation of Makran swells in the Arabian Sea. Int. J. Climatol. 40 (1), 585—593. https://doi.org/10.1002/joc.6192

Aparna, M., Shetye, S.R., Shankar, D., Shenoi, S.S.C., Mehra, P., Desai, R.G.P., 2005. Estimating the seaward extent of sea breeze from QuikSCAT scatterometry. Geophys. Res. Lett. 32, L13601. https://doi.org/10.1029/2005GL023107

Baba, M., Joseph, P.S., 1988. Wave climate off Cochin and Trivandrum. In: Baba, M., Kurian, N.P. (Eds.), Ocean Waves and beach processes. CESS, Trivandrum, 129—213.

Danish Hydraulic Institute (DHI), 2019. MIKE 21 Spectral wave Model FM User Guide. DHI, Holsholm, Denmark.

Gayathri, R., Bhaskaran, P.K., Jose, F., 2017. Coastal inundation research: an overview of the process. Curr. Sci. 112 (2), 267—278. http://www.jstor.org/stable/24912354

Glejin, J., Sanil Kumar, V., Balakrishnan Nair, T.M., Singh, J., 2013. Influence of winds on temporally varying short and long period gravity waves in the near shore regions of Eastern Arabian Sea. Ocean Sci. 9, 343—353. https://doi.org/10.5194/os-9-343-2013

Hamed, R.M., Amir, A., Brett, F.S., David, L.F., William, S., Richard, A.M., Adam, L., 2015. Increased nuisance flooding along the coasts. Geophys. Res. Lett. 42, 9846—9852. https://doi.org/10.1002/2015GL066072

Hameed, S., Kurian, N., Thomas, K., Rajith, K., Prakash, T., 2007. Wave and Current Regime off the Southwest Coast of India. J. Coast. Res. 23, 1167—1174. http://doi.org/10.2112/04-0388.1.

Hanley, E.K., Stephen, E.B., Peter, P.S., 2010. A global Climatology of wind wave interaction. J. Phys. Oceanogr. 40, 1263—1282. https://doi.org/10.1175/2010JPO4377.1

Krishnan, A., Bhaskaran, P.K., Kumar, P., 2022. Extreme wind-wave climate projections for the Indian Ocean under changing climate scenarios. Clim. Dynam. 59, 649—669. https://doi.org/10.1007/s00382-022-06147-x

Kurian, N.P., 1987. Wave height and spectral transformation in the shallow waters of Kerala coast and their prediction. Cochin Univ. Sci. Technol., Cochin, Kerala, India, 150.

Kurian, N.P., Rajith, K., Shahul Hameed, T.S., Sheela Nair, L., Ramana Murthy, M.V., 2009a. Wind waves and sediment transport regime off the south- central Kerala coast, India. Nat. Hazards 49, 325—345. https://doi.org/10.1007/s11069-008-9318-3

Kurian, N.P., Nirupama, N., Baba, M., Thomas, K.V., 2009b. Coastal flooding due to synoptic scale meso-scale and remote forcing. Nat. Hazards 48, 259—273. https://doi.org/10.1007/s11069-008-9260-4

Mahmoodi, K., Ghassemi, H., Razminia, A., 2019. Temporal and spatial characteristics of wave energy in the Persian Gulf based on the ERA5 reanalysis dataset. Energy 187, 115991. https://doi.org/10.1016/j.energy.2019.115991

McFall, B., 2019. The Relationship between Beach Grain Size and Intertidal Beach Face Slope. J. Coast. Res. 35. https://doi.org/10.2112/JCOASTRES-D-19-00004.1

Miguel, A., Jordà, G., Lionello, P., 2021. Flooding of Sandy Beaches in a Changing Climate. The Case of the Balearic Islands (NW Mediterranean). Front. Mar. Sci. 8, 2296—7745. https://doi.org/10.3389/fmars.2021.760725

Nair, L.S., Sundar, V., Kurian, N., 2011. Numerical Model Studies on the Effect of Breakwaters on Coastal Processes — A Case Study along a Stretch of the Kerala Coast, India. Int. J. Ocean Clim. Syst. 2, 291—302. https://doi.org/10.1260/1759-3131.2.4.291

Nair, L.S., Sundar, V., Kurian, N., 2013. Shore Protection for a Placer Deposit Rich Beach of the Southwest Coast of India. Int. J. Ocean Clim. Syst. 4, 41—62. https://doi.org/10.1260/1759-3131.4.1.41

Narayana, A.C., Tatavarti, R., Shinu, N., Subeer, A., 2007. Tsunami of December 26, 2004 on the southwest coast of India: Post-tsunami geomorphic and sediment characteristics. Mar. Geol. 242 (1—3), 155—168. https://doi.org/10.1016/j.margeo.2007.03.012

Parsons, M.J., Crosby, A.R., Orelup, L., Ferguson, M., Cox, A.T., 2018. Evaluation of ERA5 reanalysis wind forcing for use in ocean response modelling. In: Waves in Shallow Environments (WISE) conference, 22—26 April 2018.

Parvathy, K.G., Deepthi, G., Noujas, V., Thomas, K.V., 2014. Wave Transformation along Southwest Coast of India Using MIKE 21. Int. J. Ocean Clim. Syst. 5, 23—34. https://doi.org/10.1260/1759-3131.5.1.23

Piyali, C., Manasa, R.B., Dominic, E.R., 2019. Wave climate projections along the Indian Coast. Int. J. Climatol. 39, 4531—4542. https://doi.org/10.1002/joc.6096

Rao, A.D., Upadhaya, P., Ali, H., Pandey, H., Warrier, V., 2020. Coastal inundation due to tropical cyclones along the east coast of India: an influence of climate change impact. Nat Hazards. 101, 39—57. https://doi.org/10.1007/s11069-020-03861-9

Ramesh, M., Sheela Nair, L., Anoop, T.R., Prakash, T.N., 2022. Nearshore wave analysis from coastal video monitoring techniques at high energy micro tidal beach under sunlight dominance conditions: A case study from Valiathura beach in southwest coast of India. Reg. Stud. Mar. Sci. 51, 102205. https://doi.org/10.1016/j.rsma.2022.102205

Rashmi, R., Aboobacker, V.M., Vethamony, P., John, M.P., 2013. Co-existence of wind seas and swells along the west coast of India during non-monsoon season. Ocean Sci. 9, 281—292.

Remya, P.G., Kumar, R., Sujit, B., Abhijit, S., 2012. Wave hindcast experiments in the Indian Ocean using MIKE 21 SW model. J. Earth Syst. Sci. 121, 385—392. https://doi.org/10.1007/s12040-012-0169-7

Remya, P.G., Vishnu, S., Praveen Kumar, B., Balakrishnan Nair, T.M., Rohith, B., 2016. Teleconnection between the North Indian Ocean high swell events and meteorological conditions over the Southern Indian Ocean. J. Geophys. Res.-Oceans. 121, 7476—7494. https://doi.org/10.1002/2016JC011723

Sachin, P., Menon, A.P., Sankaranarayanan, N.R., 2014. An analysis of various coastal issues in Kerala. Int. J. Sci. Res. Educ. 2 (10), 1993—2001.

Samiksha, S.V., Rashmi, R., Vethamony, P., 2011. Wave modelling for the Indian Ocean using WAVEWATCH III. In: Proc. AOGS 2011.

Sashikant, N., Bhaskaran, P.K., Venkatesan, R., Sikha, D., 2013. Modulation of local wind-waves at Kalpakkam from remote forcing effects of Southern Ocean swells. Ocean Eng. 64, 23—35.

Scott, T., Gerhard, M., Paul, R., 2011. Morphodynamic characteristics and classification of beaches in England and Wales. Mar. Geol. 286 (1—4), 1—20. https://doi.org/10.1016/j.margeo.2011.04.004

Seelam, J., Ilangovan, D., Samiksha, S.V., Gowthaman, R., Tirodkar, G., Naik, G.N., ManiMurali, R., Michael, G.S., Raman, M.V., Bhattacharya, G., 2005. Runup and inundation limits along southeast coast of India during the 26 December 2004 Indian Ocean tsunami. Curr. Sci. 88, 1741—1743.

Sreelakshmi, S., Bhaskaran, P.K., 2020a. Spatio-temporal distribution and variability of high threshold wind speed and significant wave height for the Indian Ocean. Pure Appl. Geophys. 177, 4559—4575. https://doi.org/10.1007/s00024-020-02462-8

Sreelakshmi, S., Bhaskaran, P.K., 2020b. Wind generated wave climate variability in Indian Ocean using ERA-5 dataset. Ocean Eng. 209, 107486.

Stockdon, H.F., Holman, R.A., Howd, P.A., Sallenger Jr, A.H., 2006. Empirical parameterization of setup, swash, and runup. Coast. Eng. 53 (7), 573—588.

Swamy, G.N., Udaya, V, P., Pylee, A., RamaRaju, V.S., Chandramohan, P., 1979. Wave climate off Trivandrum (Kerala). Mahasagar- Bulletin of the national centre for Oceanography 12 (3), 127—133.

Torres-Freyermuth, A., Pintado-Patiño, J.C., Pedrozo-Acuña, A., Puleo, J.A., Baldock, T.E., 2019. Runup uncertainty on planar beaches. Ocean Dynam. 69 (11), 1359—1371.

Vethamony, P., Aboobacker, V.M., Menon, H.B., Ashok Kumar, K., Cavaleri, L., 2011. Superimposition of windseas on pre-existing swells off Goa coast. J. Marine Syst. 87 (1), 47—54.